

**THE INFLUENCE OF PORE SYSTEM CHARACTERISTICS ON
ABSORPTION AND FREEZE-THAW RESISTANCE OF CARBONATED,
LOW-LIME CALCIUM SILICATE CEMENT (CSC) BASED MATERIALS**

by

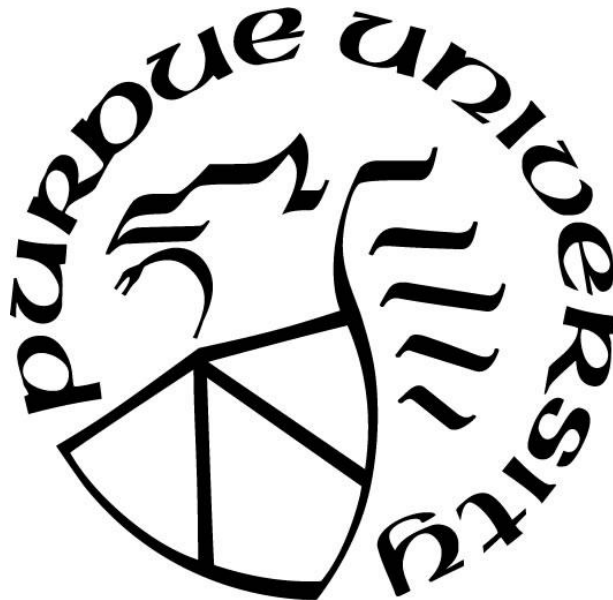
HyunGu Jeong

A Dissertation

Submitted to the Faculty of Purdue University

In Partial Fulfillment of the Requirements for the degree of

Doctor of Philosophy



Lyles School of Civil Engineering

West Lafayette, Indiana

May 2020

**THE PURDUE UNIVERSITY GRADUATE SCHOOL
STATEMENT OF COMMITTEE APPROVAL**

Dr. Jan Olek, Chair

Lyles School of Civil Engineering, Purdue University

Dr. Pablo Zavattieri

Lyles School of Civil Engineering, Purdue University

Dr. Eric Kvam

School of Materials Engineering, Purdue University

Dr. Jitendra Jain

Senior Research Scientist, Solidia Technologies

Approved by:

Dr. Dulcy Abraham

Head of the Graduate Program

To my wife, Yun-kyoung Gail Kim, and my family

ACKNOWLEDGMENTS

First of all, I would like to express my sincere gratitude to my advisor Prof. Jan Olek for his limitless support, kindness, effort, patience, vision, and immense knowledge. Foremost, his guidance helped me all the time during my research and writing of this thesis. I could not have imagined having any better advisor for my Ph.D. study.

Besides my advisor, I would like to thank the rest of my thesis committee members: Prof. Pablo Zavattieri, Prof. Eric Kvam, and Dr. Jitendra Jain, for their insightful comments and encouragement.

My special thanks goes to Solidia Technologies for providing materials and two years of research funding. Also, without teaching assistantships from undergraduate courses (CE231, CE331, and CEM321) I could not have finished my Ph.D. study.

My sincere thanks also goes to the construction materials research group at Purdue: Drs. Taehwan Kim, Ali Behnood, Belyayneh Desta, Charles Chiu, Warda Ashraf, Ayesha Shah, and Kursat Esat Alyamac. Raikhan Tokpatayeva, Robert Hershberger, Dan Huang, Reza Moini, Juan Tabares Tamayo, Santiago Ruiz, Bogdan Dykyy, Chan Jung, Adwait Trikanad, Yen-Fang Su, Guangshuai Han, Cihang Huang, Vito Francioso, Carlos Martinez, Raymond Faber, Kyle Johnson. Especially, I thank Dr. Kho Verian for his guidance in research and kindness. I adapted easily to the new environment because of him during the first year of my Ph.D. Also, I thank Dr. Parth Panchmatia for his tremendous support inside and outside school as a friend.

It will be difficult to mention all of my friends here but I am thankful for my friendships with: Chungwook Sim, Soojin Yoon, Gyuhoo Lee, Chulmin Yeom, Kyubyung Kang, Jeehee Lim, Sungsoo Park, Minsoo Baek, Seungjae Lee, Younjeong Choi, Yeonjin Bae, Goeun Han, Jooho Kim, Kyungho Kim, Jungil Seo, Yoonbo Sim, Hogun Park, Yongho Lee, Jongsoo Kim, Yonggu Lee, Jimin Kim, Jaewan Jo, Tim Lawlor, Jean Duvoisin, Peter Kovacs, Steve Meinhardt, Ryan Fleck, Daniel Castaneda, Austin Woodruff, Ignacio Diaz, Rich Santos, and Barry Hill.

Last but not least, I would like to thank my family: my parents, sisters, in-laws and wife for supporting me throughout writing this thesis and my life in general.

TABLE OF CONTENTS

LIST OF TABLES	9
LIST OF FIGURES	10
GLOSSARY	12
ABSTRACT.....	14
1. INTRODUCTION	17
1.1 Background of sustainable binders	17
1.2 Research motivation.....	19
1.3 Research objectives.....	21
1.4 Structure of the thesis.....	22
2. LITERATURE REVIEW	23
2.1 Overview.....	23
2.2 Hydraulic cement	23
2.2.1 History	23
2.2.2 Production of hydraulic cement (ordinary portland cement, OPC).....	24
2.2.3 Hydration of hydraulic cement (ordinary portland cement, OPC)	26
2.3 Non-hydraulic cement.....	26
2.3.1 History	26
2.3.2 Production of non-hydraulic cement (CSC, Solidia Cement™)	27
2.3.3 Carbonation of CSC.....	28
2.3.4 Reduction in CO ₂ emission rate of CSC.....	29
2.4 Pore system of cementitious materials.....	30
2.4.1 Introduction.....	30
2.4.2 Gel and capillary pores in cement paste	31
2.4.2.1 Hydraulic cementitious materials	31
2.4.3 Non-hydraulic cementitious materials	34
2.4.4 Pores in the interfacial transition zone (ITZ).....	34
2.4.5 Air voids	35
2.5 Water content (saturation level).....	35
2.5.1 Kelvin equation and relative humidity (capillary condensation).....	35

2.5.2	Air voids	37
2.6	Freeze-thaw behavior of hardened cementitious material	37
2.6.1	Introduction.....	37
2.6.2	Mechanisms of freeze-thaw degradation	38
2.6.2.1	Hydraulic and osmotic pressure mechanisms (Powers and Helmuth).....	39
2.6.2.2	Critical degrees of saturation level and void spacing (Fagerlund)	40
2.6.2.3	Migration of water from smaller pores to larger pores (Litvan).....	41
2.6.2.4	Pore pressure (Penttala)	42
2.6.2.5	Micro-ice-lens-theory (Setzer)	42
2.6.2.6	Disjoining pressure and ice penetration (Scherer).....	44
2.6.3	Discussion on frost damage and the role of capillary pores	44
3.	CHARACTERIZATION OF PORES IN CARBONATED CSC SYSTEMS	46
3.1	Motivations and objectives	46
3.2	Materials and methods	47
3.2.1	Mercury intrusion porosimetry (MIP)	49
3.2.2	Scanning electron microscope (SEM)	51
3.2.3	Image J analysis.....	52
3.2.4	TGA (thermal gravimetric analysis).....	52
3.2.5	DVS (dynamic vapor sorption).....	52
3.3	Results and discussion	53
3.3.1	Changes in the porosity of CSC paste with various w/c.....	53
3.3.2	Changes in the porosity of CSC paste after carbonation	54
3.3.3	The pore size distribution of CSC paste	56
3.3.4	Pore size distribution and porosity in ITZ of CSC mortars	57
3.3.5	Comparison with the OPC system.....	60
3.4	Conclusions.....	66
4.	THE RATE OF WATER ABSORPTION OF CARBONATED CSC SYSTEMS AND THE RELATIONSHIP WITH FREEZE-THAW RESISTANCE	67
4.1	Motivations and objectives	67
4.2	Materials and methods	68
4.2.1	Rate of absorption of water (sorptivity) test of paste and mortar specimens	68

4.2.2	Low temperature differential scanning calorimetry (LT-DSC).....	69
4.2.3	Freezing-thawing (F/T) experiment for paste and mortar specimens.....	70
4.3	Results and discussion	72
4.3.1	The rate of water absorption of carbonated CSC system	72
4.3.2	Effect of air entraining agent (AEA) on the rate of water absorption	74
4.3.3	Comparisons of the rate of water absorption with OPC system.....	75
4.4	The amount of freezable water in the carbonated CSC system	81
4.5	Freeze-thaw resistance of air entrained CSC system.....	82
4.6	Conclusion	86
5.	FREEZING-THAWING AND SCALING RESISTANCES OF CARBONATED CSC CONCRETE	88
5.1	Motivations and objectives	88
5.2	Materials and methods	88
5.2.1	Mixture proportions.....	89
5.2.2	Resistance to surface scaling	92
5.2.3	Freezing-thawing (F/T) test of concrete specimens - ASTM C666	92
5.2.4	SEM analysis	92
5.2.5	Air void spacing factor in hardened concrete	93
5.2.6	The volume of voids in hardened concrete.....	93
5.3	Results and discussion	94
5.3.1	Resistance to surface scaling	94
5.3.2	Resistance to freezing-thawing.....	96
5.3.2.1	Air entrained vs. non-air entrained CSCCs	96
5.3.2.2	Crushed granite vs rounded pea gravel (AE CSCCs).....	97
5.3.2.3	AE CSCC vs. AE reference concrete	99
5.3.3	SEM analysis	101
5.3.3.1	Edge of the concrete	101
5.3.3.2	Inside of the concrete.....	104
5.3.4	Air void spacing factor	106
5.4	Conclusions.....	107
6.	CONCLUSIONS AND FUTURE STUDIES	109

6.1	Conclusions.....	109
6.1.1	Pore system characterization of carbonated CSC paste and mortars.....	109
6.1.2	The rate of water absorption (sorptivity) of CSC paste and mortars.....	110
6.1.3	Effect of AEA on freeze-thaw resistance of CSC paste and mortars	111
6.1.4	Freeze-thaw resistance of CSCC vs. reference concrete	111
6.1.5	Methods for enhancement of freeze-thaw resistance of CSCC.....	112
6.2	Future study	113
	REFERENCES	114

LIST OF TABLES

Table 2.1 Typical oxide compositions of OPC.....	25
Table 2.2 Oxide composition of CSC.....	28
Table 2.3 CO ₂ emission during the production of OPC cement and Solidia cement clinker [37]	30
Table 2.4 Classification of pore sizes [19].....	31
Table 3.1 Mixture design by volume	48
Table 3.2 Properties of cements and sand.....	48
Table 3.3 Status of data collection from MIP and SEM analyses	48
Table 3.4 Summary of porosity of the CSC pastes with various w/c	54
Table 3.5 Porosity in ITZ of CSC and OPC mortars	63
Table 4.1 Test matrix and number of specimens	68
Table 4.2 Initial and secondary sorptivity of the CSC and OPC specimens (mm/sec ^{1/2}).....	77
Table 4.3 Total amount of freezable water in the CSC system	81
Table 5.1 Properties of aggregates.....	89
Table 5.2 Chemical components of cementitious materials	89
Table 5.3 Concrete Mixture Proportions	91
Table 5.4 Test matrix and the number of specimens	91
Table 5.5 Parameters related to air void system of air-entrained specimens.....	107

LIST OF FIGURES

Figure 2.1 The phase diagram of the CaO-SiO ₂ system (adapted from [12]) showing the approximate location of the composition of CSC.....	25
Figure 2.2 SEM image of Solidia cement particles after CO ₂ curing (adapted from [39]).	29
Figure 2.3 Conceptual picture of grains and water (adapted from [46])	32
Figure 2.4 Physical composition of sealed and fully hydrated Portland cement paste (adapted from [44]).....	33
Figure 2.5 Relationship between RH and Pore radius by Kelvin equation	37
Figure 2.6 Conceptual image of ice accretion due to osmotic theory.....	40
Figure 2.7 Pressure-temperature diagram for water: OB, ice-water vapor equilibrium curve; OD, supercooled water-water vapor equilibrium curve; O, triple point for water; O'A', liquid water-water vapor equilibrium curve for water containing dissolved substances (adapted from [75])..	41
Figure 2.8 Conceptual drawing of a situation in a freezing pore. Numbers 1, 2, and 3 denote different freezing conditions (adapted from [26])	42
Figure 2.9 Micro-ice-lens model. Part I shows the cooling and part II the heating phase of a freeze-thaw cycle (adapted from [76]).....	43
Figure 3.1 SEM images of the CSC pastes	55
Figure 3.2 Image J analysis – cumulative porosity and pore area distribution of CSC pastes	55
Figure 3.3 MIP results-(a)&(b), and SEM images-(c)&(d) of 0.3 w/c CSC paste	56
Figure 3.4 Pore characteristics in carbonation products of CSC paste	57
Figure 3.5 MIP (a)&(b), and TGA (c) results of CSC specimens	58
Figure 3.6 Percolation and wall effects in ITZ of CSC containing 55% aggregates (0.3w/c).....	59
Figure 3.7 Cumulative mercury intrusions of CSC and OPC pastes	60
Figure 3.8 Incremental mercury intrusions of CSC and OPC pastes.....	61
Figure 3.9 MIP results from CSC and OPC mortars (30% and 55% aggregates)	62
Figure 3.10 Percolation and wall effects in ITZ of 0.3P55.....	63
Figure 3.11 General view of 50um thickness of ITZ in mortar specimens	64
Figure 3.12 ITZs of CSC (left side) and OPC (right side) mortars.....	65
Figure 4.1 Temperature regime of one freezing-thawing cycle.....	71
Figure 4.2 Conceptual water absorption path depending on the volume of aggregates	72

Figure 4.3 Water absorption of the CSC system without AEA	73
Figure 4.4 Saturation level of CSC system without air entraining agent.....	74
Figure 4.5 Effect of AEA on the water absorption of the CSC system (A: air entrained)	74
Figure 4.6 Effect of air entraining agent on saturation level	75
Figure 4.7 Comparison of the characteristic of air voids in CSC and OPC.....	78
Figure 4.8 Rate of water absorption (sorptivity) test results from the paste and mortar specimens	79
Figure 4.9 Degree of saturation of the paste and mortar specimens	80
Figure 4.10 DSC results of melting ice in the CSC system	81
Figure 4.11 Relationship between the amount of freezable water and the CSC paste content.....	82
Figure 4.12 Relative dynamic modulus of elasticity (RDME) of CSC specimens under F/T cycles	83
Figure 4.13 Mass change of CSC specimens under F/T cycles	84
Figure 4.14 Close view of CSC specimens at the failures	84
Figure 4.15 Overview: the appearances of the CSC specimens exposed to F/T cycles	85
Figure 5.1 Locations of SEM samples	93
Figure 5.2 Mass changes of AE CSCC and AE Reference concrete (scaling test)	94
Figure 5.3 Appearances during scaling test (AE concretes)	95
Figure 5.4 Appearance of the CSCC specimens	97
Figure 5.5 Comparison of air entrained and non-air entrained CSCCs	97
Figure 5.6 Appearances of the AE CSCC specimens	98
Figure 5.7 Comparisons of crushed granite and pea gravel.....	99
Figure 5.8 Appearances of the specimens after freezing-thawing test	100
Figure 5.9 Results from freezing-thawing experiment	101
Figure 5.10 BSE images of the edge of each specimen.....	103
Figure 5.11 BSE images of the inside of the specimens.....	105

GLOSSARY

AE: air entrained

AEA: air entraining agent

ASTM: American society for testing materials

C₂S: dicalcium silicate or belite (2CaO·SiO₂)

C₃A: tricalcium aluminate (3CaO·Al₂O₃)

C₃S: tricalcium silicate or alite (3CaO·SiO₂)

C₃S₂: rankinite (Ca₃Si₂O₇)

C₄AF: tetracalcium aluminoferrite (4CaO·Al₂O₃·Fe₂O₃)

CaCO₃: calcium carbonate

CaO: lime

CaSO₄: gypsum or CaSO₄·H₂O

CH: calcium hydroxide or portlandite (Ca(OH)₂)

CO₂: carbon dioxide

CSC: low-lime calcium silicate cement (non-hydraulic cement) or Solidia Cement™

C-S-H: calcium silicate hydrate (C₃S₂H₈, 3CaO·2SiO₂·8H₂O)

DSC: differential scanning calorimetry

DVS: dynamic vapor sorption

F/T: freeze-thaw or freezing-thawing

H: water (H₂O)

HCO₃⁻: bicarbonate

ITZ: Interfacial transition zone

LT-DSC: low temperature-differential scanning calorimetry

MIP: mercury intrusion porosimetry

N/A: non-available

NAE: non-air entrained

OPC (PC): ordinary portland cement

RDME: relative dynamic modulus of elasticity

RH: relative humidity

S.G.: specific gravity

SCM: supplementary cementitious material

SEM: scanning electron microscope

SiO₂: silicon dioxide or silica

TGA: thermal gravimetric analysis

w/c: water-to-cement ratio

α-CS: pseudowollastonite (CaSiO₃)

β-CS: wollastonite (CaSiO₃)

ABSTRACT

Author: Jeong, HyunGu. PhD

Institution: Purdue University

Degree Received: May 2020

Title: The Influence of Pore System Characteristics on Absorption and Freeze-Thaw Resistance of Carbonated, Low-lime Calcium Silicate Cement (CSC) based Materials

Committee Chair: Jan Olek

The new cementitious binder, calcium silicate-based cement (CSC, a.k.a. Solidia cement™), was developed in order to combat the issue of CO₂ emissions during the cement manufacturing process. Currently, the production of 1 tonne of cement results in the emission of approximately 0.81 tonne of CO₂, mainly as a result of the decomposition of large quantities of limestone and high clinkering temperatures. CSC dramatically reduces the emission of during the manufacturing process CO₂ to levels of approximately 0.565 tonne per tonne of cement (30% reduction). However, unlike ordinary portland cement (OPC), CSC contains low levels of low-lime calcium silicate phases (mostly wollastonite, pseudowollastonite, and rankinite) and is therefore non-hydraulic. Thus, in order to harden, CSC must undergo the carbonation process, which is achieved by exposure to external source of CO₂.

In ordinary portland cement concrete, the inherent pore structure (i.e., gel pores, capillary pores, and air voids) of the material plays a significant role in its resistance to harsh environments (e.g., exposure to de-icing chemicals during cold weather and frequent freeze-thaw cycles). As an example, a larger number of saturated capillary pores reduces the freeze-thaw resistance of concrete, unless the concrete has been sufficiently air-entrained. Therefore, to facilitate the successful use of CSC in construction projects, in-depth evaluations of the properties of various types of concrete that can be produced using this new material are needed, including evaluation of mechanical performance, durability, and serviceability characteristics. Additionally, evaluating the pore system of CSC is also essential to achieve a comprehensive understanding of its functional behavior. Therefore, an in-depth investigation of the pore system of the carbonated CSC system was conducted, including assessment of the effects of the pore system on water absorption, which affects the freeze-thaw resistance of concrete. Specifically, the primary purpose of this research was to identify mixture design parameters that resulted in improved freeze-thaw resistance of CSC concrete.

To achieve this goal, pore characteristics of the carbonated CSC based systems (pastes and mortars that contained various amounts of aggregate) were evaluated using such techniques as mercury intrusion porosimetry (MIP), scanning electron microscopy (SEM), and image analysis. The types of the carbonated CSC systems investigated (i.e. paste and mortars) were shown to contain two types of pores: large capillary pores (greater than 30 μm) in the bulk matrix and small capillary pores (5 nm ~ 100 nm) between crystals of calcium carbonate. Reduction of paste content in the CSC mortars resulted in percolation (i.e. establishment of spatial connectivity of the pores) and an in generation of larger pores (i.e., pore with diameters between 0.1 and 4 μm) at the interfacial transition zone (ITZ). In contrast, the ITZ in the OPC mortars was relatively less porous. In addition, the CSC system contained a higher volume of capillary pores as compared to the OPC system.

The porosity characteristics of CSC affected its ability to absorb water. The CSC specimens had the highest initial rate of water absorption and absorbed the most water among all tested specimens, including the OPC series with various water-to-cement ratio (w/c) values. These tendencies of the CSC system were somewhat alleviated when the CSC was air-entrained (AE). Also, the time to reach peak saturation of the AE CSC was delayed. Thus, using air entraining agents (AEA) appeared to have a positive influence on the degree of saturation of the CSC system. However, the peak level of saturation (over 90%) of the CSC system was not reduced to the same degree as that of the OPC system.

When exposed to freeze-thaw (F/T) cycles, all non-AE CSC specimens (both paste and mortars) failed rather suddenly, after only a few (~4) F/T cycles. However, AE CSC systems showed improved F/T performance and no sudden failures were observed. In the case of AE CSC mortar that contained 55% aggregates, the values of the relative dynamic modulus of elasticity (RDME) were lower than that of AE CSC mortar that contained 30% aggregates. This was due to the increased porosity of the ITZ that led to the percolation (increase in connectivity) of the pores in this high (55%) aggregate volume mortar. Thus, to improve the performance of the CSC concrete, it will be essential to enhance its F/T resistance by densifying the porous ITZ or by reducing the surface area of the aggregates. Densification of ITZ can be accomplished by using well-graded and angular aggregates that yield better packing and bonding with cement paste. This will reduce connectivity of the pores and increase the tortuosity of the pore network

in any type of concrete, including CSC concrete (CSCC). Decreasing the surface area of aggregates can be accomplished by using larger size aggregates.

To evaluate the extent to which the differences in pore structure of the CSC and OPC systems influence the F/T resistance of corresponding concretes, three different CSCC mixtures were produced and tested. These included non-AE and AE concretes with crushed granite coarse aggregate and AE concrete with pea gravel. The F/T performance of these mixtures was compared to F/T performance of AE reference concrete. The reference concrete, based on binary binder system (OPC + 20% of fly ash) and crushed limestone as a coarse aggregate, was previously found to perform well under F/T conditions. The F/T performance of AE CSCC containing crushed granite was found to be comparable to that of the reference concrete whereas the other two CSCC mixtures suffered more severe damage.

1. INTRODUCTION

1.1 Background on sustainable binders

According to estimates included in the Emission Database for Global Atmospheric Research (EDGAR), the 2018 worldwide emissions of CO₂ from fossil fuels, industrial processes (including cement, steel, and chemicals), and product use totaled approximately 37.88 Gt [1]. Also, the United States Environmental Protection Agency (EPA) reported that, as of 2016, the production of cement in the US resulted in the release of approximately 0.394 Gt of CO₂, which accounts for ~1% of global CO₂ emissions [2], [3]. In 2016, cement production was reported to be responsible for CO₂ emissions totaling 1.45 ± 0.20 Gt [2]. Furthermore, since concrete is the second most used material in the world after water [4], even a small increase in CO₂ output due to production of cement results in a significant increase in the overall carbon footprint associated with construction infrastructure. Realizing these problems, the construction industry has been actively involved in various efforts to reduce CO₂ output over the last four decades or so; these efforts include the development of carbon capture and storage techniques, increasing the efficiency of thermal and electric energy, and the use of alternative fuels. Most notably, these efforts include a reduction in the overall amount of cement used in concrete (by partial substitution of cement with supplementary cementitious materials) and, more recently, attempts to develop alternative binders for low carbon cements.

As mentioned in the previous paragraph, one of the ways to reduce the amount of cement used in concrete is to replace the cement with various amounts of supplementary cementitious materials (SCMs). Depending on the type of SCM used, the replacement level can vary from approximately 5% (for silica fume) to as high as 60% (for slag cement or some of the fly ashes when used in high volume fly ash concrete). Typical SCMs are either siliceous or calcium-silico-aluminous by-products generated in various industries, including the manufacture of silicon or ferrosilicon alloys, the manufacture of iron, or the burning of coal in electric power plants. The use of these materials is not only beneficial from the perspective of reusing byproducts, but it also increases the service life of concrete due to the participation of SCMs in the so-called “pozzolanic reaction”, in which the SCMs react with calcium hydroxide (CH or portlandite, which is the by-product of a hydraulic reaction involving ordinary portland cement (OPC)) to

form calcium-silicate-hydrate (C-S-H). This C-S-H produced by the pozzolanic reaction is the same as the C-S-H produced by hydration of cement. Since “pozzolanic reaction derived” C-S-H is formed in addition to the C-S-H produced from OPC hydration by consuming the “easily-leachable” CH, the net results are microstructure densification and reduced potential of water ingress or other harmful ionic species [5].

In addition to the industrial by-products mentioned in the previous paragraph, certain processed natural materials (e.g., calcined clay, shale, and metakaolin) are also often used as SCMs [6]. As an example, calcined clays have been used to increase the resistance of concrete to sulfate attack, to reduce expansion due to alkali-silica reactivity, and to reduce permeability. Similarly, metakaolin (which has been used as both an additive and a replacement for cement) lowers the permeability of concrete and increases its strength [5].

In summary, although the use of SCMs in concrete offers some benefits (reducing the amount of cement and improving service life), these types of concrete still require a certain amount of OPC in their mixture. This is due to the fact that the presence of CH, which results from OPC hydration, is necessary for the pozzolanic reaction to initiate.

It should be pointed out that SCMs can also be activated by mixing them with other chemicals, as exemplified by the development of so-called “geopolymers”. These materials were first introduced in 1979 by Davidovits who initially contributed to the development of rapid setting concrete [7]. Geopolymers do not require OPC or CH to initiate the hardening process. Instead, the hardening is initiated by alkaline solutions (e.g., sodium hydroxide or sodium silicate) [7], [8]. Although geopolymer concrete has a high degree of strength and high resistance to chemicals and temperature and, when cured at an elevated temperature (60°C), also has low creep and shrinkage, it requires special handling (i.e., the use of costly chemical activators). Currently, geopolymer concrete is probably best suited for the production of precast elements [9], [10].

Another attempt at lowering the CO₂ footprint associated with cement clinker production involved lowering the clinkering temperature and the amount of limestone. The OPC is produced by heating a finely divided mixture consisting of approximately 80% limestone and 20% clay in a rotary kiln to a temperature of approximately 1450°C. This process results in the decomposition of limestone and generates approximately 0.5 tonne of CO₂ for every tonne of clinker (60% of 866 kg CO₂/t of clinker without including the contribution from the burning of

the fuel) [11]. The resulting OPC clinker contains mostly alite (Ca_3SiO_5) and belite (Ca_2SiO_4). The alite starts to form above 1250°C and the reactive form of belite forms mainly between $1000\sim 1200^\circ\text{C}$ [12].

Since alite hydration plays an essential role in forming the mechanical properties of concrete (the hydration is faster than that of belite), lowering the kiln temperature, which limits the production of alite, has been problematic in the cement industry. Development of the product Aether cement by the Lafarge group is an example of an attempt at lowering the CO_2 output at a semi-industrial scale associated with the production of the OPC clinker, which involved lowering the temperature of the kiln [13]. Aether cement, also referred to as belite-calcium sulfoaluminate-ferrite (BCSAF) cement, has been reported to require clinkering temperatures below 1300°C [14], [15]. The hydration process of Aether cement is different from the hydration process of the OPC. First, the calcium sulfoaluminate in BCSAF cement reacts with soluble calcium sulfate and produces ettringite and amorphous aluminum hydroxide gel (AH_3). When the soluble sulfate is no longer available, monosulfoaluminate (AFm) and AH_3 are forming. The AH_3 reacts with belite to produce crystalline stratlingite (C_2ASH_8). Finally, at a later age, the C-S-H can also form due to hydration of belite hydrates [16].

Most recently, Solidia Technologies Inc. introduced non-hydraulic, low-lime calcium silicate cement (CSC), called Solidia CementTM. The sintering temperature of this product is approximately 1200°C , which is 100°C lower than what is required for the production of BCSAF cement [17]. Furthermore, as compared to the OPC, the production of CSC requires only approximately 50% of limestone, with clay-like materials serving as a source of silica. It is expected that production of this cement will result in an approximate 30% reduction in CO_2 emissions as compared to production of the OPC [18]. The CSC is composed mostly of non-hydraulic, low-calcium silicates, including wollastonite, pseudowollastonite (CaSiO_3), rankinite ($\text{Ca}_3\text{Si}_2\text{O}_7$), and a small amount of belite (Ca_2SiO_4). The CSC hardens as a result of carbonation, rather than hydration, and during the process, the cement consumes CO_2 . Additional details regarding this non-hydraulic cement binder are presented in Section 2.3.

1.2 Research motivation

Since the previously mentioned non-hydraulic cement called Solidia CementTM (which will be abbreviated as CSC throughout this dissertation) is a new material, extensive research needs

to be performed in order to fully characterize its properties that will help to understand its applicability as a construction material. Similarly, comprehensive characterization of the properties of the CSC mortar and concrete will also be required.

Compressive strength is one of the key properties of any concrete used in construction, since this is a primary parameter specified in structural codes. In addition to being vital from the perspective of load-bearing capacity and safety, compressive strength is also linked to other important physical and mechanical properties of concrete such as density, tensile strength, and modulus of elasticity. For example, denser concrete (i.e., concrete with lower porosity) typically has higher compressive strength [19]. Similarly, concrete with higher compressive strength will also have higher elastic modulus and higher tensile strength [19]. However, the strength of concrete alone does not adequately represent all aspects of its durability (also called service life).

In terms of controlling the service life of concrete, the porosity of the hardened cement paste is one of the most important parameters. This is because pores represent internal defects that affect physical and mechanical properties of concrete, such as strength, elasticity, diffusivity, and permeability. However, it is important to note that the concretes given the same volume of pores may have very different properties as, in addition to total porosity, the interconnectivity (and the relative size) of the pores also plays a major role [20]. Since the porosity of the CSC concrete is the result of the carbonation process (and not hydration, unlike ordinary portland cement (OPC)), it is crucial to characterize the system of pores of this new material and its influence on the durability of concrete.

Carbonation of CSC raises the possibility that the resulting hardened matrix will have a different pore system as compared to the pore system of OPC that results from hydration. In the OPC system, most of the mixing water becomes chemically and physically bound to the hydration products, with some of the free water evaporating at a sufficiently low relative humidity (RH) (up to approximately 40%). However, in the case of CSC, most of the mixing water evaporates during the carbonation process, with some of the water potentially becoming trapped in the amorphous silica gel, which is one of the reaction products. Some of the water can also be physically adsorbed on the surfaces of unreacted cement particles or calcium carbonates (which are the main binding phase in carbonated CSC systems). As a result, the pore structure of carbonated CSC systems may be quite different from that of the OPC system and therefore may have different effects on the durability of CSC concrete under certain environmental conditions.

This is because the durability of concrete is significantly influenced by its porosity, which is typically directly related to the permeability of the material. In turn, the permeability of the material depends on pores size, shape, and connectivity, since these factors determine how fast the material can absorb liquids from external sources.

Based on the potential differences in the characteristics of the pore system that is present in carbonated CSC concrete and OPC, the focus of this study was to evaluate how they influence freeze-thaw and scaling resistance of the material, as both of these properties are highly dependent on the nature of the pore system [21]–[31].

Since the pore structure of carbonated CSC paste has not been extensively studied, there is a need to identify the range of pore sizes and the volume of each distinct size of pore (e.g., gel, capillary, and larger pores). In addition, the rate of absorption (i.e., sorptivity) as well as total absorption need to be identified. These values are compared to those obtained for the OPC system. In addition, changes in the characteristics of the pore system resulting from varying the volume of aggregate in the mixtures is also be evaluated. Lastly, freeze-thaw resistance of CSC concrete is tested following the ASTM C666-2003 (procedure A) standard and the results are compared to those obtained for the reference concrete (20% OPC replaced with Class C fly ash).

1.3 Research objectives

This study consists of three distinct phases and the specific objectives of each phase are described as follows:

- a) Phase I (Chapter 3): Pore system characterization of carbonated CSC paste and mortar
 - Evaluation of pore size distribution in carbonated CSC systems
 - Classification of pores in carbonated CSC systems
 - Comparison of the pore size distribution in carbonated CSC with the pore size distribution in the hydrated OPC system
- b) Phase II (Chapter 4): Determination of the absorption and sorptivity properties of CSC systems and their effects on freeze-thaw resistance
 - Evaluation of the absorption and sorptivity properties of carbonated CSC systems containing various proportions of fine aggregate
 - Comparison of the absorption and sorptivity properties of carbonated CSC systems with or without air entrained agent (AEA)

- Comparison of the absorption and sorptivity properties of carbonated CSC systems to the properties of hydrated OPC mortars.
- c) Phase III (Chapter 5): Freeze-thaw and scaling resistance of carbonated CSC concrete
- Evaluation of freeze-thaw and scaling resistance of carbonated CSC concretes comprised of various mix designs and comparison to the resistance of air entrained reference concrete (20% OPC replacement with Class C fly ash).

1.4 Structure of the thesis

This dissertation contains six chapters. Chapter 1 includes a discussion of the need for non-hydraulic cement (CSC), discusses the motivation for the research, and presents the objectives. Chapter 2 discusses the production, composition, and hardening processes of OPC and CSC, which is followed by a review of the pore system of hardened cementitious materials and a discussion of degradative mechanisms during freeze-thaw cycles, both of which highlight the effects of porosity on the freeze-thaw resistance of concrete. Chapter 3 describes the characterization of pore systems of carbonated CSC paste and mortars. Chapter 4 discusses the sorptivity and freeze-thaw resistance of carbonated CSC systems (paste and mortars). Chapter 5 describes the freeze-thaw and scaling resistances of carbonated CSC concrete. Chapter 6 contains the conclusions of this study and suggestions for future works.

2. LITERATURE REVIEW

2.1 Overview

This chapter starts with a brief description of the history, production, and the hardening process of each type of cement (both hydraulic and non-hydraulic). This is followed by a discussion of carbon emissions during the production of both ordinary portland cement (OPC) and non-hydraulic cement (CSC). Then, the following characteristics of cement are reviewed: (i) the pore systems of OPC and CSC pastes; (ii) interfacial transition zone (ITZ) and air voids in OPC concrete; and (iii) capillary condensation in capillary pores. Finally, the mechanisms of freeze-thaw degradation of concrete, which is the main focus of this study, are reviewed, which included a discussion of frost damage and the role of capillary pores.

2.2 Hydraulic cements

2.2.1 History (development of portland cement)

Hydraulic cements were discovered in the 18th and 19th centuries by several researchers: James Parker in 1796 (England), Vicat in 1813 (France), and James Frost in 1822 (England). In 1824, Joseph Aspdin termed hydraulic cement as “portland cement”, which was based on the limestone quarry on the Isle of Portland. The portland cement under Aspdin’s patent was prepared by calcining a mixture of finely ground limestone and clay. In 1845, Isaac Johnson introduced a type of portland cement that was produced by burning raw materials at a high clinkering temperature (above 1400°C), which ensured a proper clinker composition for hydration of cement. In the United States, David Saylor received the first patent for American portland cement in 1871. After 1909, Thomas Edison received several patents for rotary kilns and the addition of gypsum to clinker that increased the setting time of portland cement was introduced. Following the development of portland cement, it has been widely used in the field of construction [19].

2.2.2 Production of hydraulic cement (ordinary portland cement, OPC)

The raw materials used in the manufacturing of OPC include limestone (calcium carbonate) and clay (or silts) as sources of calcium oxide (CaO) and silica (SiO₂), respectively. Once the raw materials are adequately proportioned, they are loaded into the cement kiln where they undergo several transformations, depending on the temperature. These include water evaporation, calcination, and clinkering. The limestone starts to decompose above 600°C and the initial chemical reaction between CaO and SiO₂ occurs at approximately 1200°C, which results in the formation of dicalcium silicate (C₂S). In the temperature range between 1200~1450°C (the clinkering zone), the more reactive (C₃S) phase forms by a reaction between C₂S and CaO (lime). The phases present in OPC are shown in Figure 2.1 as a function of temperature and CaO content. The typical oxide composition of OPC is shown in Table 2.1. The main phases present in OPC include tricalcium silicate (3CaO·SiO₂, C₃S, alite), dicalcium silicate (2CaO·SiO₂, C₂S, belite), tricalcium aluminate (3CaO·Al₂O₃, C₃A), and tetracalcium aluminoferrite (4CaO·Al₂O₃·Fe₂O₃, C₄AF, ferrite). As C₃S can only form above 1400°C, it requires a significant amount of energy. However, this phase is the most critical with respect to strength development, especially at early ages (up to 28 days). The contribution of the remaining phases to strength development is much less significant except for the C₂S that contributes to strength at later ages.

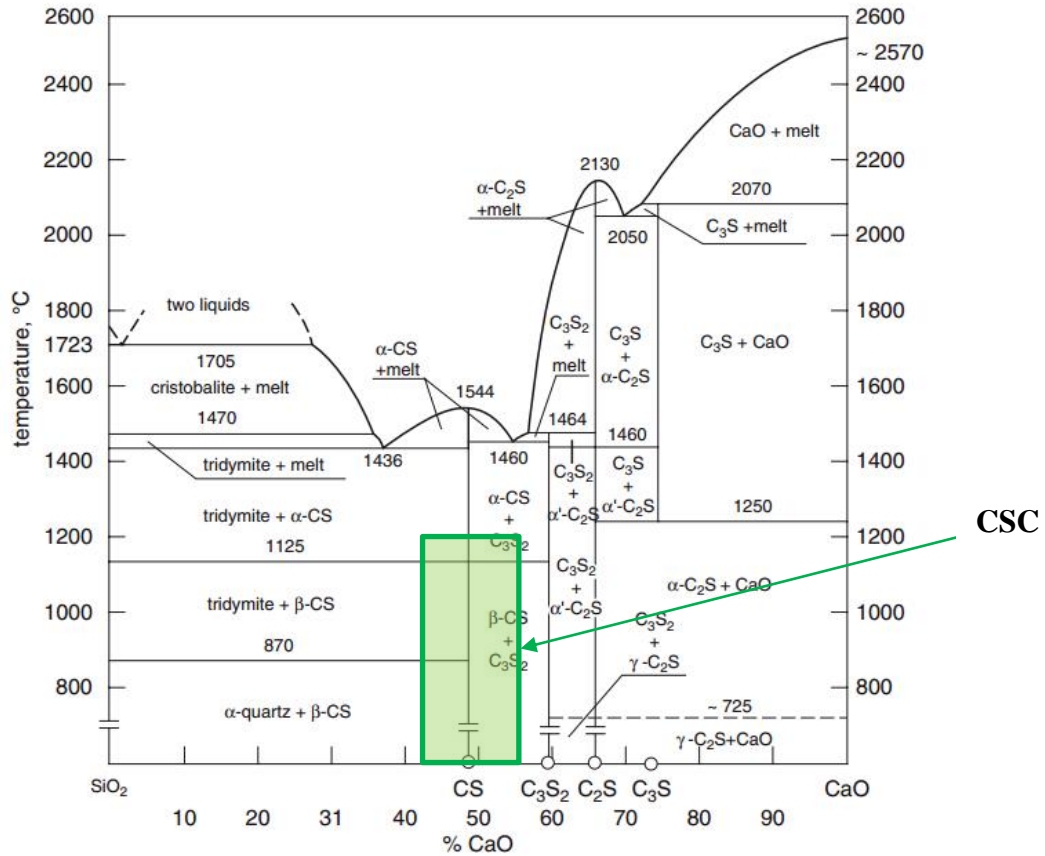


Figure 2.1 The phase diagram of the CaO-SiO₂ system (adapted from [12]) showing the approximate location of the composition of CSC

Table 2.1 Typical oxide composition of OPC

SiO ₂	21.03%
Al ₂ O ₃	6.16%
Fe ₂ O ₃	2.58%
CaO	64.67%
MgO	2.61%
SO ₃	2.02%
Na ₂ O	0.33%
K ₂ O	0.60%
Total	100.00%

2.2.3 Hydration of hydraulic cement (OPC)

When OPC reacts with water, a series of chemical reactions occur that produce hydration products. The rate of hydration of OPC are in the following order: $C_3A > C_3S > C_4AF > C_2S$. If not controlled, rapid hydration of C_3A will cause so called “flash set” due to formation of large amounts of monosulfoaluminate or calcium aluminate hydrates [19]. Thus, addition of gypsum is required to slow down this process. As shown in Equation 2.1 and Equation 2.2, the main hydration products of C_3S and C_2S are calcium silicate hydrates ($C_3S_2H_8$, C-S-H). Both C_3S and C_2S contribute to ultimate strength, but the rate of hydration of C_2S is significantly slower than that of C_3S . Thus, in most cases, it is desirable for cement to have a higher content of C_3S .



where C, S, and H indicate CaO, SiO₂, and H₂O respectively.

The composition of the hydration product is quite variable and the formula $C_3S_2H_8$ is only approximate. Due to its poor crystalline structure, this product is typically called C-S-H gel. In addition to being a major contributor to strength, the porosity of C-S-H also plays a vital role in controlling the durability properties of hardened concrete. More details regarding the nature of porosity present in C-S-H are provided in Section 2.4. In contrast to C-S-H, calcium hydroxide ($Ca(OH)_2$, CH), which is an additional hydration product, has a crystalline structure with fixed chemical composition. CH dissolves readily in water and releases OH⁻ ions that help to maintain a high pH level in the pore solution. Furthermore, dissolution of CH increases porosity of the matrix, which reduces its durability.

2.3 Non-hydraulic cements

2.3.1 History

Before the development of portland cement, various types of non-hydraulic cements were used as early as 6,500 B.C. by Syrians. Subsequently, Romans refined the usage of these cements in concrete mixtures [32]. At that time, the primary materials used as non-hydraulic cements were gypsum ($CaSO_4 \cdot H_2O$) and lime (CaO). The reaction of lime with water produces calcium

hydroxide. Upon dissolution in water, atmospheric CO₂ forms carbonate ions (CO₃²⁻) that, upon combining with hydrogen ions (H⁺), form bicarbonate ions (HCO₃⁻). At the same time, calcium hydroxide releases calcium ions (Ca²⁺) and hydroxyl ions (OH⁻). These dissolved ions form calcium carbonate (CaCO₃), as shown in the equations below [33]–[35].



Since the production of lime (CaO) from limestone (CaCO₃) requires high temperature (approximately 1000°C), Egyptians preferred to use gypsum (2CaSO₄·2H₂O) that is obtained by mixing hemihydrate (2CaSO₄·1/2H₂O) with water. The advantage of using hemihydrate is that its production from naturally occurring bassanite (2CaSO₄·H₂O) requires a much lower temperature, only up to 130°C.

Development of hydraulic cement greatly diminished the need for non-hydraulic cements. However, production of hydraulic cement is responsible for approximately 8% of total CO₂ emissions. As discussed in Chapter 1, reducing CO₂ emissions from cement production has been encouraged. In response to these concerns, the use of non-hydraulic cement to reduce the greenhouse effect seems appropriate, but it faces practical challenges in construction projects as compared to the use of hydraulic cement: slow strength development and speed of construction [36]. Recently, Solidia TechnologyTM developed a new non-hydraulic cement to meet both requirements of reducing CO₂ emissions and fast strength development that uses a temperature (1200°C) and lime content (below 45%) that are both lower than those used in hydraulic cement production.

2.3.2 Production of Solidia CementTM (CSC)

The manufacturing process of CSC is very similar to that used for manufacturing OPC except for the relative proportions of components in the raw mix and clinkering temperature. During the first stage of the production process, a mixture of limestone, sand, clay or shale (as sources of lime (CaO) and silica (SiO₂)) are injected into the same type of kiln that is used for production of OPC. The maximum temperature needed to manufacture CSC is ~1200°C, which is roughly 250°C lower than that required for OPC production.

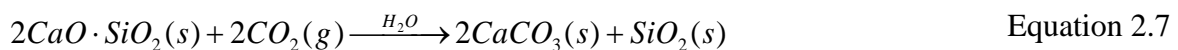
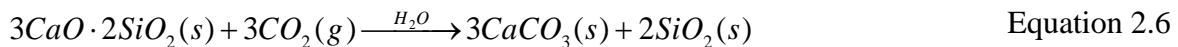
As shown in Figure 2.1, at temperatures above 1200°C, C₃S and C₂S are the dominant phases present in the CaO-SiO₂ system with high CaO content. C₃S and C₂S are the main reactive phases present in OPC. However, in the case of CSC, due to the lower amount of limestone in the mixture of raw materials, α-CS (pseudowollastonite) is the main phase. In addition, below 1200°C, β-CS (wollastonite) is likely to be present as a second primary material of CSC. Also, depending on the CaO content (above 50~60%), rankinite (C₃S₂) and belite (C₂S) are also produced. Unlike OPC, since CSC is non-hydraulic, additional gypsum is not required for set-controlling.

Table 2.2 Oxide composition of CSC

SiO ₂	44.02%	P ₂ O ₅	0.06%
Al ₂ O ₃	5.13%	Mn ₂ O ₃	0.04%
Fe ₂ O ₃	1.79%	SrO	0.12%
CaO	43.64%	Cr ₂ O ₃	0.01%
MgO	1.15%	ZnO	0.01%
SO ₃	0.16%	BaO	0.03%
Na ₂ O	0.33%	L.O.I. (950°C) ²	0.71%
K ₂ O	1.94%		
TiO ₂	0.22%	Total	99.36%

2.3.3 Carbonation of CSC

As mentioned in Section 2.3.2, the main components of CSC are wollastonite, pseudowollastonite (CaSiO₃), rankinite (Ca₃Si₂O₇), and belite (Ca₂SiO₄). These phases undergo the CO₂ curing process to generate the desired strength as conventional OPC concrete. Unlike the hydration of OPC, CSC does not react with water during the hardening process, as shown in the chemical reactions below.



Theoretically, water acts as a transport medium that carries CO_2 for the reaction between HCO_3^- and CaO . This reaction is an exothermic reaction that releases 87kJ/mole of heat, and the water absorbs the heat and evaporates during this process [37].

As shown in Figure 2.2, when CSC reacts with CO_2 , CaCO_3 starts to form between cement particles, and CaCO_3 , the product, glues the cement paste and aggregates together. In addition, out-rims of the reacted particles remain as the dominant silica phase. It is assumed that Ca^{++} ions leach out from CSC particles to react with CO_2 [38].

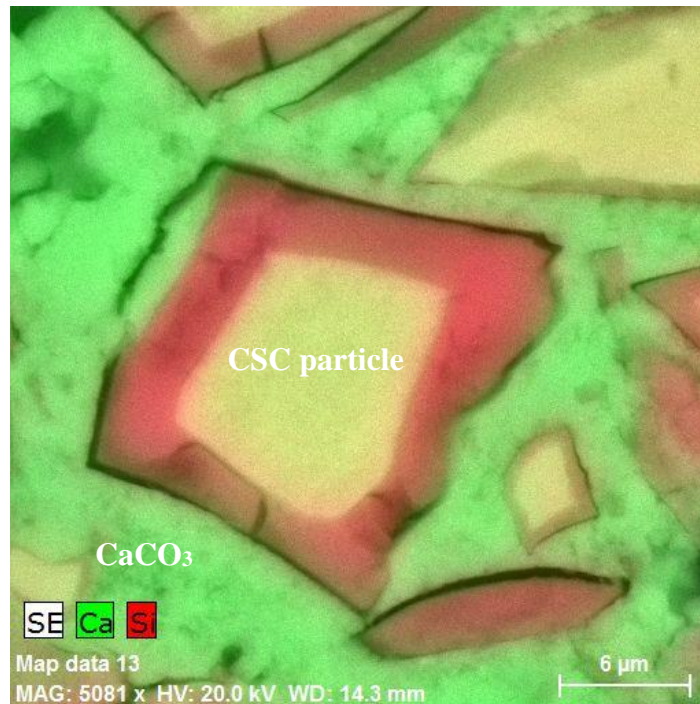


Figure 2.2 SEM image of Solidia cement particles after CO_2 curing (adapted from [39]).

2.3.4 Reduction in CO_2 emission rate of CSC

As shown in Table 2.3, 1 tonne of cement emitted 810 kg of gaseous CO_2 when limestone decomposes to lime during OPC production, which requires a higher amount of an energy source (fuel) to heat the kiln to 1450°C . However, in the case of CSC, it requires a lower proportion of limestone (~50% of raw materials) as compared to OPC (~70% of raw materials), and this directly reduced the CO_2 emission to 80% of the total CO_2 emission during the production of OPC. Additionally, a 10% reduction in total CO_2 emission can be achieved because the required manufacturing temperature for producing CSC is 250°C lower than for producing OPC.

Table 2.3 CO₂ emission during the production of OPC cement and Solidia cement clinker [37]

CO ₂ emissions from	Per tonne of OPC clinker	Per tonne of CSC clinker
Limestone decomposition (required limestone)	540kg (~70% of raw materials)	375kg (~50% of raw materials)
Fossil fuel combustion (required temperature in kiln)	270kg (~1450°C)	190kg (~1200°C)
Total CO ₂ emissions	810kg	565kg

2.4 Pore system of cementitious materials

2.4.1 Introduction

As briefly mentioned in Chapter 1, the performance and durability of concrete are directly related to its pore system, which influences both the mechanical properties and chemical resistance of the material.

The internal pore system in hardened concrete contains a wide range of pore sizes that can be roughly divided into the following three categories (see Table 2.4): i) gel pores (up to 10 nm), ii) capillary pores (between 10 nm and 10 μm) and iii) air voids (larger than 10 μm); entrained air bubbles are typically in the range of 100 μm (0.1 mm) to 1,000 μm (1 mm). The porous interfacial transition zone (ITZ) typically contains entrapped and entrained air voids.

The gel pores are responsible for such properties as shrinkage and creep while the capillary pores influence the strength and permeability of the cement paste. Combining paste with fine aggregate produces mortar while addition of coarse aggregate to mortar results in formation of concrete. In each case, the incorporation of aggregates results in the creation of voids in the interfacial zone between cement paste and aggregates due to the so-called “wall effect”. Entrained air can be found in concrete that is intended for use in a cold environment that protects cement paste from internal pressure while freezing. A more in-depth discussion of the porosity of hydrated cement paste is presented in the following sections.

Table 2.4 Classification of pore sizes [19]

Pore size (diameter)	Type of pore	Role of water	Effects on paste
~0.5 nm	Gel pore	Chemically binding water	Shrinkage, Creep
0.5 nm ~ 2.5 nm	Gel pore	Adsorbed water	Shrinkage, Creep
2.5 nm ~ 10 nm	Small (gel) capillary pore	Cause high surface tension	Shrinkage
10 nm ~ 50 nm	Medium capillary pore	Moderate surface tension	Strength, Permeability, Shrinkage
50 nm ~ 10 μ m	Large Capillary pore	Bulk water	Strength, Permeability
0.1 mm ~ 1 mm	Entrained air	-	Strength

2.4.2 Gel and capillary pores in cement paste

2.4.2.1 Hydraulic cementitious materials

As briefly mentioned in Chapter 1, cement paste pores are classified as either gel or capillary pores based on pore size.

Gel pores range between 0.5 nm and 10 nm [20]. Gel pores form in C-S-H layers during hydration of cementitious materials. In addition, when the interlayer water in C-S-H (or the adsorbed water on C-S-H) is drying at high temperature or below 50% RH, the interlayer space becomes gel pores. Thus, gel pore volume increases as the amount of cement particle hydrates or the degree of hydration increases. Gel pores usually cause shrinkage and creep of cement paste below 50% relative humidity (RH), since the gel pores create internal pressure while the gel water is drying.

Capillary pores range between 10 nm and 10 μ m. Initially, capillary pores are filled with mixing water in fresh concrete, but then become empty when the pore water is consumed for hydration of cementitious material. Unlike the gel pores, as hydration progresses, the volume of the capillary pores is reduced, since the capillary size of the space filled with water becomes smaller due to the growth of the hydration products in that space. Capillary pores can be classified into two groups: large (50 nm~10 μ m) and medium (10 nm~50 nm). Due to pore size, capillary water can be easily vaporized above 50% RH level at room temperature, which plays a significant role in permeability and strength. For instance, as capillary pore volume decreases,

the permeability of concrete decreases and the strength of concrete increases. Over the past decades, several researchers have developed models describing the formation of C-S-H structure [40]–[43]. A conceptual picture of C-S-H gel is shown in Figure 2.3.

Regarding hydrated OPC, T.C. Powers developed a robust model several decades ago that describes the physical structure of hardened cement paste. Later, Hansen used this model to promote a better understanding of a few fundamental ideas to cement researchers. Powers and Hansen [43]–[45] developed mathematical approaches that can be used to predict the fractional volume of pores in hardened cement paste. The volume of gel and capillary pores can be estimated using the following equations.

$$(a) \text{ Fractional volume of gel pores} \quad \frac{0.19\alpha}{(w_o/c) + 0.32} \quad \text{Equation 2.8}$$

$$(b) \text{ Fractional volume of capillary pores} \quad \frac{(w_o/c) - 0.36\alpha}{(w_o/c) + 0.32} \quad \text{Equation 2.9}$$

where (w_o/c) is the original water-cement ratio by weight, and α is a degree of hydration ($0 \leq \alpha \leq 1$).

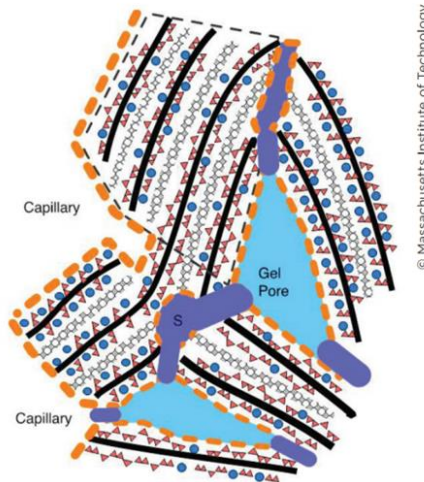


Figure 2.3 Conceptual picture of grains and water (adapted from [46])

According to Powers and Brownyard [47], in addition to pores, cement paste contains three additional phases: capillaries (capillary water), unhydrated cement (unreacted cement particle), and cement gel that includes solid hydrated cement and water-filled gel pores. When cement

paste is sealed, no external source of water is provided, and the volume fraction of each phase can be calculated using the following equations:

(a) fractional volume of cement gel $\frac{0.68\alpha}{(w_o / c) + 0.32}$ Equation 2.10

(b) fractional volume of unhydrated cement $\frac{(1-\alpha)\times 0.32}{(w_o / c) + 0.32}$ Equation 2.11

(c) fractional volume of empty capillary pores $\frac{0.0575\alpha}{(w_o / c) + 0.32}$ Equation 2.12

Hansen plotted the volume of each phase in cement paste, which depends on the water-to-cement ratio when the degree of hydration reaches 100% ($\alpha=1$), as shown in Figure 2.4 [44].

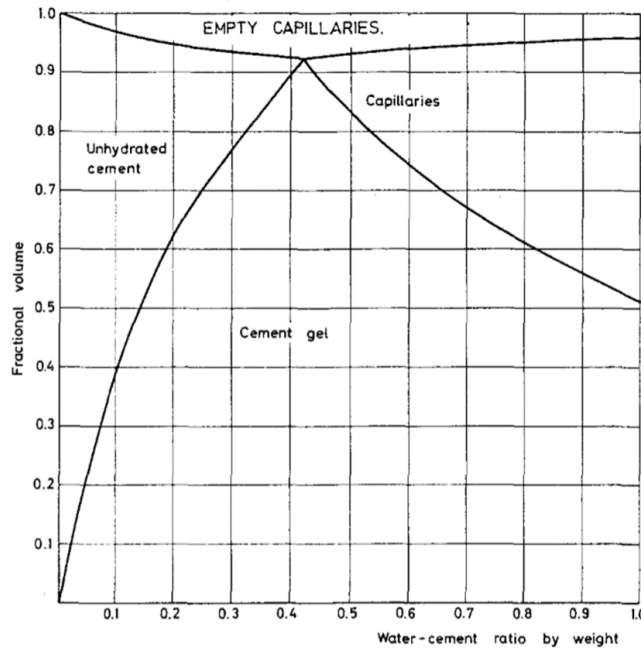


Figure 2.4 Physical composition of sealed and fully hydrated Portland cement paste (adapted from [44])

In the case of a non-hydraulic cement (CSC) system, its physical structure of hardened (or carbonated) cement paste has yet to be fully described. Villani et al. [48] studied the pore size distribution of carbonated natural wollastonite, which is one of the raw constituents of non-hydraulic cement. Based on the Dynamic Vapor Sorption (DVS) technique, the authors concluded that as the degree of carbonation increases, the volume of porosity of its system

decreases. In other words, as carbonation increases, the volume of gel pores (< 10 nm) increases and the volume of capillary pores (> 10 nm) decreases. In addition, the range of pore size was similar to OPC (w/c 0.42), but the volume of each pore size was not presented [48].

2.4.3 Carbonated low-lime calcium silicate cement (CSC) based materials

Only a few researchers [48], [49] have studied the pore system of carbonated wollastonite (CaSiO_3). According to Ashraf [49], gel pores and capillary pores were about 32.3% and 67.7% of the total volume of pores, respectively. The ranges of capillary pore sizes were 10~41 nm (3.2% of the total volume of pores) and larger than 40 nm (64.5% of the total volume of pores). In the case of carbonated rankinite, which is an additional phase of non-hydraulic binder in this study, Ashraf reported that the total volume of pores is comprised of 45.6% gel pores, 6% capillary pores, and 48.5% capillary pores larger than 40 nm. The total volume of pores is approximately 0.136 ml/g of rankinite in 0.4 w/c system. Another researcher, Villani, reported that, as the degree of wollastonite carbonation increases, the volume of gel pores (< 10 nm) increases with 0.2 w/c [48].

2.4.4 Pores in the interfacial transition zone (ITZ)

When cement particles hydrate and bind aggregates together in concrete, the cement paste around the surface of aggregates may have different characteristics relative to other parts of the concrete. This region is called the interfacial transition zone (ITZ). Several researchers found that the ITZ can influence the mechanical strength of concrete and can also affect the durability of the concrete, depending on the porosity (or density) of ITZ or the chemical product that fills ITZ [50], [51]. When cement particles, aggregates, and water are mixing together, the water tends to separate the cement particles from the aggregates (wall effect), which causes more water to accumulate in the region around the aggregates. Thus, this zone remains porous after hydration, which results in a weak zone within the concrete matrix. Typically, the thickness of ITZ is 20~50 μm . Due to its larger pore size, the ITZ also influences the strength and permeability of concrete.

As explained above, the wall effect by the water between particles of cement grains and aggregates, CSC concrete system would also have this interfacial transition zone. Ashraf et al.[52]

found that elastic modulus in ITZ is 30~35% weaker than the bulk modulus of carbonated cement paste. However, the porosity of ITZ has not been explained.

2.4.5 Air voids

Entrapped and entrained air are considered to be large pores in concrete. Entrapped air forms irregularly shaped air pockets that are relatively larger than entrained air voids. Entrapped air results from improper mixing, such as segregation, dry mix, and less slump. This is not considered to be pores in cement paste, but entrapped air has adverse effects on concrete: low strength and low durability. In contrast, entrained air is regularly sphere-shaped, with sizes ranging between 10 μm to 1 mm. Entrained air is intentionally induced by chemical admixtures that have both hydrophobic and hydrophilic properties, like soap or detergents. Changes in the mechanical properties of concrete are dependent on the volume of entrained air. However, uniform distribution of air voids would significantly improve durability in cold regions.

2.5 Water content (saturation level)

2.5.1 Kelvin equation and relative humidity (capillary condensation)

Typically, the saturation level of gel and capillary pores in cement paste vary with the level of relative humidity. According to Brunauer–Emmett–Teller (BET) theory [53], at relative humidity below 35%, the monolayer of water molecules (adsorbate) is physically adsorbed onto the surface of pores within solids (adsorbent), and the monolayer attracts additional water molecules so that the monolayer of water turns into multilayers of water molecules on the surface of the pores. When the level of relative humidity is above 40%, capillary pores become filled with water due to capillary condensation. As the van der Waals interactions between vapor phase molecules increases, vapor condensation increases in confined capillary pores, because of the meniscus that forms at the liquid-vapor interface that allow equilibrium to be established below the saturation vapor pressure. The relationship between vapor pressure and the surface tension of liquid-vapor phase molecules can be explained by a mathematical approach for the pore size distribution of porous materials, as shown by the Kelvin equation below [20], [54]. Note that it is assumed the pores have a cylindrical shape.

$$r_k = \frac{-2\gamma V_{\text{mol}} \cos \theta}{RT \ln(P/P_0)} = \frac{k}{\ln(P/P_0)} \quad \text{Equation 2.13}$$

where $k = \frac{-2\gamma V_{\text{mol}} \cos \theta}{RT}$ that is constant for the liquid adsorbate,

r_k is the radius of the pore in which condensation occurs (m),

γ is the surface tension of the liquid adsorbate (N/m),

V_{mol} is the volume occupied by one mole of condensate at temperature T (m³/mol),

θ is the contact angle between the liquid and the pore wall,

R is the gas constant (8,314 J/Kmol·K),

T is the temperature (K),

P is the pressure (N/m²), and

P₀ is the saturation vapor pressure (N/m²).

In the case of water as a liquid adsorbate at ambient temperature, γ is 72.8×10^{-3} (N/m), V_{mol} is 17.98×10^{-6} (m³/mol), θ is assumed to be zero between cement paste and water, and T is 298.15 K. So, k for water at ambient temperature is -1.056 and r_k is $-0.156/\ln(P/P_0)$ (m). According to the Kelvin equation, in a pore radius range of 1.5 nm to 105 nm, the pores are always filled with water (or pore solution) at 50~99% RH level due to equilibrium vapor pressure. However, only pores up to a radius of 105 nm (RH up to 98.5%) can be mathematically estimated as shown in Figure 2.5. Furthermore, the actual upper limit in the pore radius of this relationship is 50 ~ 60 nm, since the pressure change of 0.981 to 0.984 is almost negligible [55], [56].

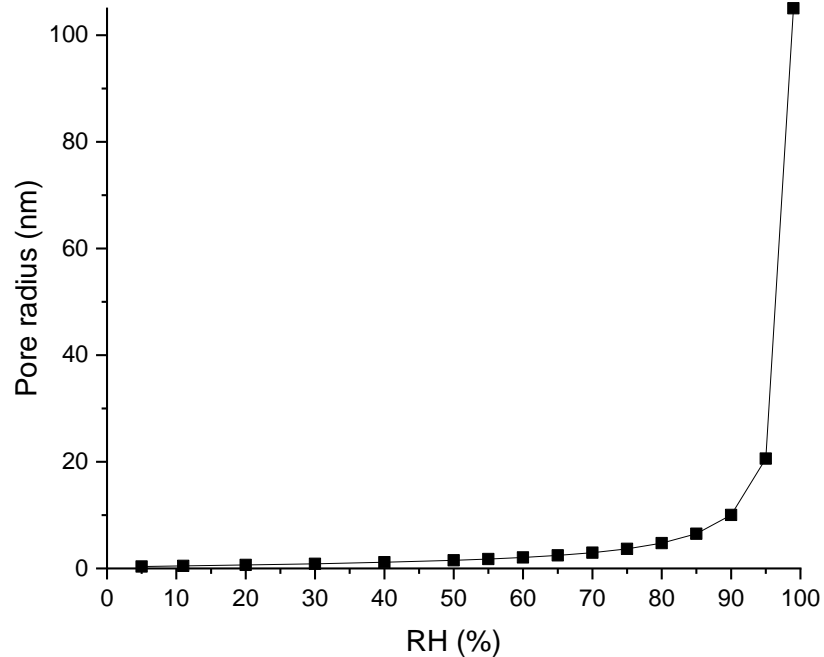


Figure 2.5 Relationship between RH and pore radius based on the Kelvin equation

2.5.2 Air voids

Capillary condensation (mentioned in Section 2.5.1) does not occur within capillary pores that are larger than 1 μm and also not within entrained and entrapped air voids since vapor saturation pressure is low in air voids. Thus, larger pores are typically filled with air unless they are infiltrated by external water. The distribution of entrained air voids in hardened cement paste is a critical parameter with respect to the prevention of freeze-thaw damage, since the additional void space relieves the internal pressure caused by freezing water.

2.6 Freeze-thaw behavior of hardened cementitious material

2.6.1 Introduction

When exposed to freezing temperatures, concrete that contains a sufficient amount of internal moisture (i.e., having a degree of saturation higher than approximately 85% [28]) can suffer both internal and external degradation. This is primarily due to the fact that freezing of moisture leads to an approximate 9% increase in its volume, which generates internal pressure within the water-filled pores. Also, the ice keeps growing because the water near the ice migrates

toward the freezing site. If the growing volume of ice (developing pressure) can no longer be accommodated by the pore space, damage to the microstructure will occur [57].

Surface scaling is the most common form of external degradation and it is greatly accelerated by the presence of deicing chemicals [58]. Scaling involves loss of paste or mortar from the very top layer of concrete (typically approximately 1 mm) and is commonly visible on the surface of parking lots, slabs, sidewalks, bridge decks, and pavements. Although the damage due to scaling is typically “cosmetic” in nature, in more severe cases it may lead to significant changes in surface roughness. On the other hand, internal damage typically manifests in the form of microcracking within the paste and an associated loss of strength. This type of damage can directly affect the service life of the structure, since an increase in the cumulative number of freeze-thaw cycles will lead to the formation of additional cracks. The higher number of cracks will in turn increase the likelihood of external water and deicing chemicals entering into the interior of the structure. In addition to physical damage, deicing chemicals can also cause chemical degradation of the paste [58]. While the internal physical damage can be effectively controlled by the creation of a proper air-void system, the control of chemical degradation remains a challenge.

2.6.2 Mechanism of freeze-thaw degradation

As mentioned in Section 2.6.1, freeze-thaw deterioration is categorized as physical damage. The mechanism of frost damage of cementitious materials was initially described by T.C. Powers, based on hydraulic and osmotic pressure theories [21], [59], [60]. However, this mechanism was not completely explained, because it is also dependent on the size of pores, the distribution of pores, and the ionic concentration of pore solutions. Because of this complexity, additional attempts have been made to completely describe the mechanism based on different viewpoints, such as thermodynamics and poromechanics, as described by Helmuth [22], Litvan [61], [62], Marchand [63], Scherer [64], Coussy [65], Setzer [66]–[68]. However, it should also be mentioned that to date, no consensus has been reached regarding the actual mechanism that leads to the damage of cementitious materials during exposure to freezing-thawing (F/T) [58]. The details of the development of the mechanism of frost damage are provided in the following sections.

2.6.2.1 Hydraulic and osmotic pressure mechanisms (Powers and Helmuth)

T.C. Powers studied and proposed a mechanism of freeze-thaw degradation in concrete over several decades. At first, from 1945-1949, he thought it was simply because of excessive internal pressure resulting from the increased volume of water due to ice formation. However, he found that unfrozen water is forced to move away from the site of frozen water, once water in pores starts freezing [24]. If the empty space in the concrete matrix is not sufficient to accommodate the unfrozen water, it builds up excessive internal pressure (i.e., hydraulic pressure). As a result, the concrete matrix would be susceptible to micro-cracking. Based on this finding, he also suggested that if voids are well-spread throughout the concrete matrix in the range of specific distance (0.008in), it will reduce the damage due to the action of freeze-thaw. Another researcher by the name of Helmuth [22], [69] found that, depending on the pore size, the melting point of ice crystals can vary. He described that as pore size becomes smaller, the melting point of ice is reduced. Thus, the pore size (a few μm) in cement paste is considered to be small enough to lower the melting point. Moreover, in a pore solution, alkalis lower the melting point of ice, but the effect of alkalinity on lowering the melting point of ice is not as great as the effect of the size of pores. From this point of view, a pore solution at 0°C remains unfrozen and the pore solution will be forced to move away from the frozen site. Thus, Powers and Helmuth thought that hydraulic theory itself was not sufficient to understand the mechanism of degradation due to freeze-thaw.

In 1975, Powers found another cause that may explain the mechanism of freeze-thaw damage in concrete [21]. As mentioned earlier, most of the pore solution in concrete contains alkalis; therefore, the freezing temperature of pore solution should be substantially low enough. Thus, when the pore solution starts to freeze, it is divided into two regions in the pores: ice and unfrozen pore solution. Furthermore, by this process, the unfrozen pore solution becomes more concentrated alkaline solution. Due to the increased alkali concentration in the unfrozen pore solution, a low alkali concentration solution near that area tends to move toward the high alkali concentration solution by osmosis. During this process, osmotic pressure develops that maintains an equilibrium. Once again, the diluted high alkali concentration solution has now become the lower alkali concentration solution, and this causes additional ice growth to form in the concrete. This phenomenon is called ice-accretion and is shown in Figure 2.6.

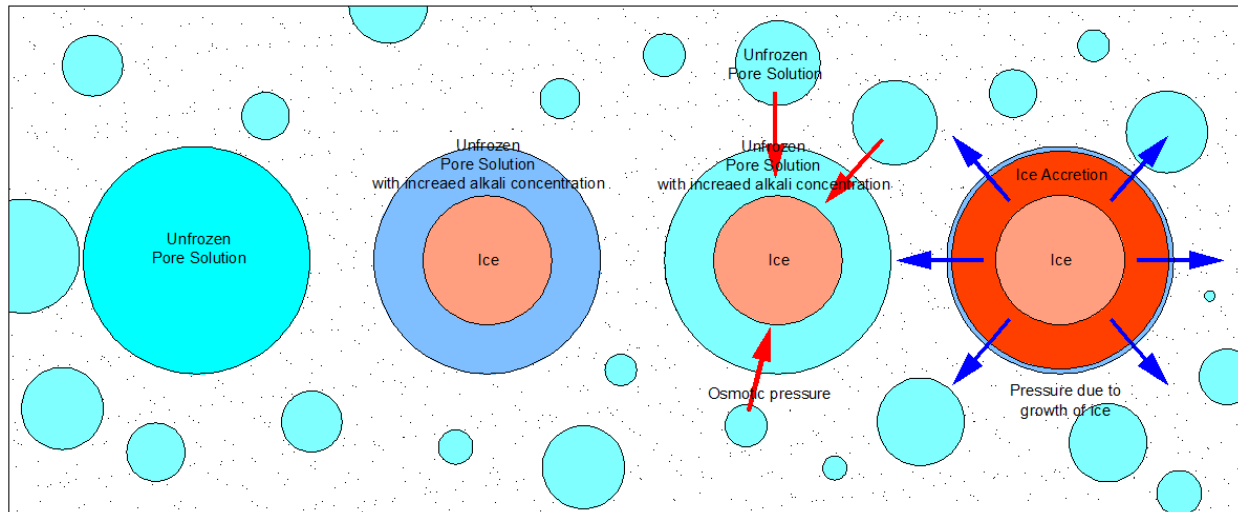


Figure 2.6 Conceptual image of ice accretion due to osmotic theory

2.6.2.2 Critical degrees of saturation level and void spacing (Fagerlund)

According to hydraulic and osmotic pressure mechanisms, water should be present in pores in order to cause damage from freeze-thaw cycles. Therefore, water content in the pores (i.e., the saturation level of the pore) is an essential parameter for determining the degree of freeze-thaw damage. In 1972, Fagerlund introduced the concept of “critical degree of saturation” [70], which was combined with the concept of “critical spacing factor” from Powers’ study [60]; the term, “critical spacing factor”, indicates the limiting distance of water flow between pores that prevents frost damage [23]. He mentioned that air-filled capillary pores absorb water and are saturated first and then smaller sized pores become saturated. In other words, with a high volume of water-filled pores, the concrete is susceptible to freeze-thaw damage if the distance of water flow is longer than the critical spacing factor. As a result, this causes significant internal pressure during freezing because the water released from the saturated pores cannot migrate toward near air-filled pores. Furthermore, some water is trapped in the pathway and freezes. Fagerlund calculated saturation level as the ratio of the total volume of evaporable water to the total porosity in concrete. He also suggested that if the saturation level exceeds 90%, significant damage from a single freezing cycle could occur [23]. Nowadays, in terms of a critical spacing factor for avoiding or minimizing freeze-thaw damage, the Portland Cement Association (PCA) recommends an empirical spacing factor that is shorter than 0.008 inch [71].

2.6.2.3 Migration of water from smaller pores to larger pores (Litvan)

Litvan conducted freeze-thaw experiments on hydrated cement pastes [61], [62], [72]–[74]. He monitored dimensional changes of the specimens in order to evaluate the influence of parameters such as the water-to-cement ratio, air entrainment, and the degree of saturation. Based on these studies, Litvan observed that repetitive adsorption and desorption (and the associated phase transition of the adsorbate) accelerates frost damage to cement paste. Based on these observations, he proposed a mechanism of frost action based on adsorption and desorption behaviors at temperatures below the freezing point of the adsorbate. This finding confirmed the osmotic pressure theory. Litvan agreed that frost damage occurs when water moves toward a freezing site (i.e., flowing from smaller pores to larger pores), especially when de-icing salts are present in the pore solution. The presence of deicing chemicals in the pore solution increases the migration of water since deicing salts decrease the vapor pressure in pores; preventing water from drying increases the difference in vapor pressure between the external ice layers on the surface of cement paste and the water in capillary pores. Thus, he concluded that the vapor pressure difference causes the forced migration of water (i.e., desorption and adsorption of adsorbate) to reestablish the vapor pressure equilibrium.

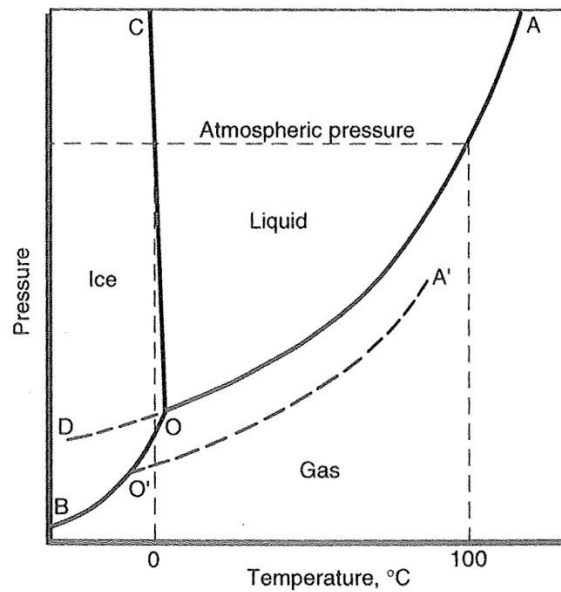


Figure 2.7 Pressure-temperature diagram for water: OB, ice-water vapor equilibrium curve; OD, supercooled water-water vapor equilibrium curve; O, triple point for water; O'A', liquid water-water vapor equilibrium curve for water containing dissolved substances (adapted from [75])

2.6.2.4 Pore pressure (Penttala)

Since the 1980s, for modeling the frost action mechanism using a poroelastic approach, researchers have focused on the freezing action around the gel and capillary pores. Because of the non-freezable water layer on the capillary pore walls, several researchers have studied the different pressures affected by the pore entrance size, curvature of the pore walls, and phase of adsorbate (water). As shown in Figure 2.8, Penttala [26] divided a pore into three different conditions regarding the phase of water and the pressure level in the pore, which varies based on the boundary condition between the two different phases of water. According to his modeling (see Figure 2.8), the freezing pressures at 2 and 3 are approximately 10 times higher than the pressure at 1; thus, if there were more scenarios of 2 and 3 in porous solid materials, then the material would be susceptible to freezing. As an example, his experimental results showed that a non-air entrained mortar specimen experienced the highest freezing pressure (4~7 times higher as compared to the air entrained mortar specimens).

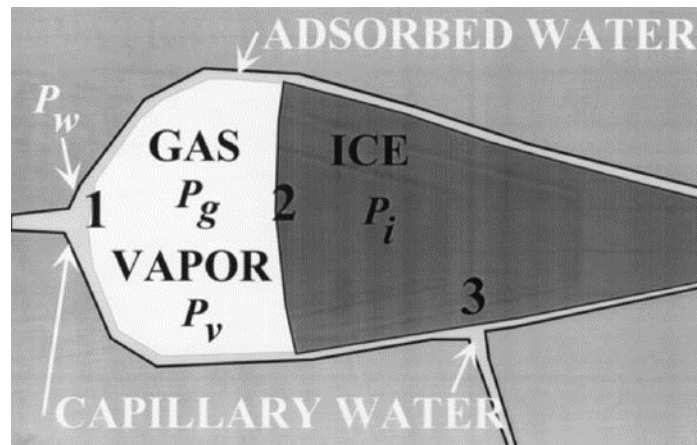


Figure 2.8 Conceptual drawing of a situation in a freezing pore. Numbers 1, 2, and 3 denote different freezing conditions (adapted from [26])

2.6.2.5 Micro-ice-lens-theory (Setzer)

According to Power's hydraulic theory, a porous solid material should expand due to ice formation but Setzer found that a porous material undergoes frost shrinkage (abnormal contraction) after initial ice formation because of the water that is squeezed out of the gel-matrix [66], [67]. Then, the water is supposed to transfer back into the expanding gel space during heating. However, the micro-ice-lenses in larger pores hinder water from flowing back into its

original space and this would suck in more external water during heating, as shown in Figure 2.9. IIb. Thus, the temperature acts as a piston and micro-ice-lens acts as a valve for water transfer. Setzer named this physical phenomenon the Micro-Ice-Lens theory or model. This model is based on the fundamentals of nonequilibrium thermodynamic treatment, the affinity of the freezing and thawing process in microporous systems, and the velocity of mass transfer. Setzer pointed out that the three phases (liquid, vapor, and ice) of water coexist over a wide temperature range, that differences in pressure are only due to temperature, and during cooling, the degree of saturation in the gel is reduced while the degree of saturation in larger ice-filled pores increases. Thus, as the number of freezing-thawing cycles increases, the porous solid material absorbs additional external water.

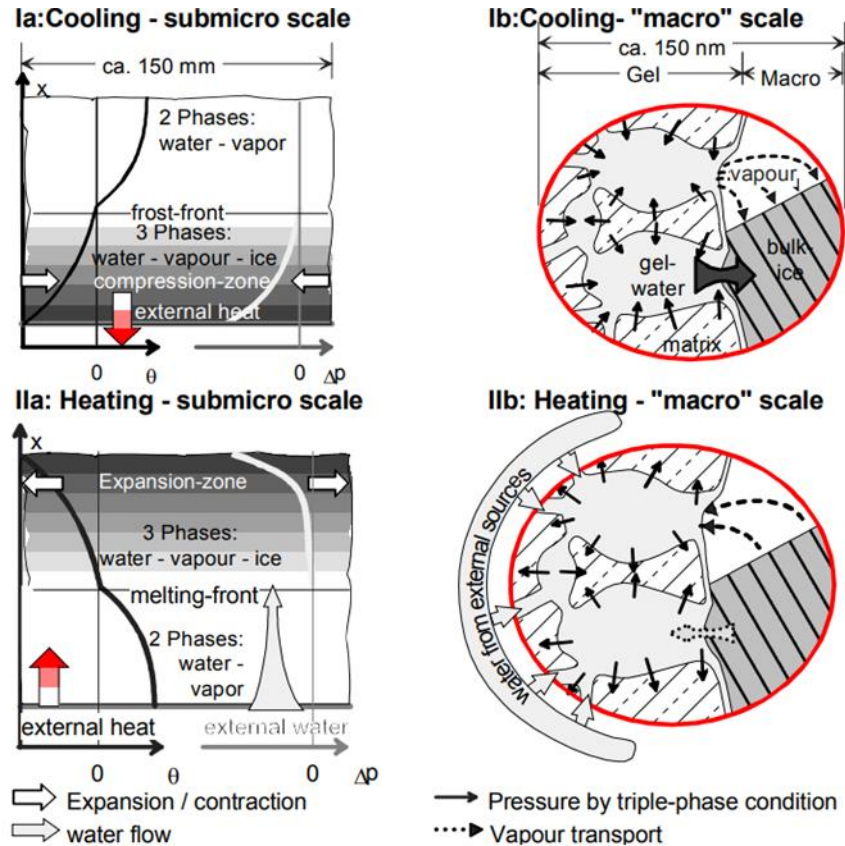


Figure 2.9 Micro-ice-lens model. Part I shows the cooling and part II the heating phase of a freeze-thaw cycle (adapted from [76])

2.6.2.6 Disjoining pressure and ice penetration (Scherer)

Scherer explained the concept of ice penetrating (or propagating) into a pore system based on the Gibbs-Thomson equation [64]. Ice penetrates the next smaller size of pores (r_p) once the T satisfies the condition, as shown in Equation 2.14. Ice nuclei in the pores that are larger than r_p attract water from the surrounding capillary pores until the T is decreased in order to penetrate the next smaller size of r_p . In addition, in the same cylindrical size of pores, ice cannot drain water away from the same size of pores because the curvatures of the liquid and vapor interface are always less than that of the crystal liquid interface. The pressure from ice growth is greater than the pressure from water vapor at the other side of cylindrical pore. If the ice growth rate in the pores is rapid, then the body of the pores expands [22] since there is less time for the excess water to evaporate.

$$r_p \geq \delta + \frac{2\gamma_{CL}}{(T_m - T)\Delta S_{fv}} \quad \text{Equation 2.14}$$

where δ is the thickness of the liquid film between the crystal and the pore wall; for water, $\delta \approx 0.9$ nm, γ_{CL} is the specific energy of the crystal/liquid interface, T_m is the melting point of a crystal, and ΔS_{fv} is the molar entropy of fusion; for ice, $\Delta S_{fv} = (S_L - S_C)/v_c \approx 1.2$ J/(cm³·K).

2.6.3 Discussion on frost damage and the role of capillary pores

Frost damage mechanisms of concrete are still the subject of scientific debate due to the contradictions between hydraulic and osmotic pressure theories. Hydraulic pressure theory initially stated that frost damage results mainly from ice expansion, and ice formation forces the water to move out from the freezing site of capillary pores. However, experimental results showed that the water moves to the freezing site of capillary pores from near gel or capillary pores [21], [26], [64], [67], [70]. Furthermore, some researchers found that dilation of cement paste samples occurs within the organic pore solution (benzene) that does not expand as it freezes [77], [78]. Thus, the hydraulic theory itself cannot truly explain the entire frost damage mechanism of cement paste. To provide a better understanding of the migration of water during ice formation, the osmotic pressure theory was introduced.

As shown in Figure 2.6, ice crystals in pores attract additional water from the smaller pores near the ice crystal, which amplifies the volume of the ice. However, osmotic pressure theory

itself cannot explain the role of air voids that prevent the migration of water from gel and capillary pores by providing larger pores. As mentioned in Section 2.5.1, the water in air voids evaporates as soon as the relative humidity falls below 100% if an external source of water is unavailable. Thus, according to Powers, air voids are partially filled with water and ice starts to form on the wall of the air voids. Then, the ice begins to attract water from capillary and gel pores near the air voids, which eventually prohibits ice from forming in the smaller pores. However, when the freezing rate (ice growth rate) is fast, ice forms instantly such that there would be no time for water to travel inside of the porous medium to reach the site of the ice crystals in large air voids. Therefore, osmotic pressure theory itself cannot fully explain the frost damage of concrete.

Typically in the winter, relative humidity is approximately 50~70% and thus pores smaller than 10 nm in diameter are saturated at an equilibrium state. When the weather changes, the surface of the cement paste is susceptible to changes in relative humidity. Thus, when the relative humidity reaches higher than 60~70%, the capillary pores near the surface of the cementitious material tend to adsorb or absorb water faster than the air voids (10~100 μm). Also, the capillary pores tend to hold water longer than the air voids until ice starts to form in the capillary pores. Eventually, the capillary pores are likely to be saturated first with water. The water content in capillary pores are more susceptible to changes in temperature and relative humidity, as explained in Section 2.5. Moreover, the saturated capillary pores become filled with air due to the ice accretion in larger air voids. The repetition of this phenomena brings more external water into the air-filled capillary pores if external water is available. As freezing-thawing cycle or the duration of freezing increases, the ice penetration depth from the surface of the cementitious material increases.

3. CHARACTERIZATION OF PORES IN CARBONATED CSC SYSTEMS

3.1 Motivations and objectives

For carbonation of CSC particles, hypothetically, a barrier consisting of a film of water around CSC particles needs to be formed during mixing. The water film accommodates calcium ions that leach from raw materials (uncarbonated CSC) and carbon dioxide. In the water film, gaseous carbon dioxide (CO_2) is converted into bicarbonate (HCO_3^-), and the bicarbonate attracts calcium ions to form calcium carbonate, which induces the cement particles and aggregates to bind together. After carbonation, theoretically, the mixing water is not bound to any chemical product (Equation 2.5 and Equation 2.6). However, a certain amount of water will either be chemically bound or physically absorbed to Ca-modified silica gel and amorphous calcium carbonates [49], [79]. Most of the mixing water may evaporate because of the exothermic reaction that results from the carbonation of CSC and the curing temperature (60°C). Eventually, this evaporation of water will contribute to increased porosity of CSC. Unlike the carbonation of CSC, water reacts with OPC particles and most of the mixing water is chemically bound to hydrated OPC products. This indicates that as the mixing water is consumed for hydration, the volume of hydrated products, including gel pores, grow in the space where the mixing water was accessible. At the same time, the volume of capillary pores decreases as hydration progresses, which causes the OPC paste to construct a denser structure over time. Thus, in carbonated CSC paste, the pore system is unique due to the evaporation of water and much larger pores compared to that of the same w/c of OPC paste.

As previously mentioned in Section 2.4.2, extensive studies on the pore structure of hardened OPC paste have been performed by many researchers. Powers and Brownyard [43] developed a basic model that linked the volume of various components in the hydrated matrix to the initial w/c and the degree of hydration. Similarly, the properties of the pore structure of OPC paste have been extensively characterized by several researchers [40], [41], [55], [80]–[83] using such techniques as mercury intrusion porosimetry (MIP) and scanning electron microscopy (SEM). However, as mentioned in Section 1.2, these studies were not conducted with systems that were made with the CSC binder. For this reason, this chapter focuses on the following tasks: a) determination of the pore size distribution of carbonated CSC paste and comparison of this

distribution with the distribution of typical pore size categories (e.g., gel and capillary pores) that are present in OPC systems, b) determination of the pore size distribution of carbonated CSC mortars containing various volumes of fine aggregate. The results of this chapter are used to determine the role of the characteristics of the pore system in sorptivity of the carbonated CSC system (in Chapter 4) and in the resistance of CSC-based concretes to freezing and thawing as well as scaling (in Chapter 5).

3.2 Materials and methods

For characterization of the OPC and CSC pore systems, a series of pore characterization analyses were performed: MIP, SEM, and Image J software. MIP analysis was used to determine the pore size distribution of the hardened cement system and the total porosity. SEM analysis was conducted to identify the location, shape, and size of pores in the hardened cement systems. Image J software was used to analyze the porosity and the pore size histogram using the SEM images.

For both MIP and SEM, three 0.5(d) × 0.5(h) cylindrical samples were casted from the same batch. After casting, OPC specimens were cured for 28 days in the moist curing room (23°C and 98 ± 2% RH) and CSC specimens were cured for 7 days in a carbonation chamber (60°C, greater than 80% RH, and 20% CO₂). After one day of CO₂ curing, CSC specimens were removed from the molds and placed back into the CO₂ chamber for another 6 days of CO₂ curing.

Table 3.1 Mixture design by volume

w/c & type	0.3 & CSC			0.3 & OPC (PC)			0.42 & OPC (PC)			0.6 & OPC (PC)		
Label	0.3C0	0.3C30	0.3C55	0.3P0	0.3P30	0.3P55	0.42P0	0.42P30	0.42P55	0.6P0	0.6P30	0.6P55
OPC	-	-	-	51%	36%	23%	43%	30%	19%	35%	24%	16%
CSC	54%	38%	24%	-	-	-	-	-	-	-	-	-
Sand	0%	30%	55%	0%	30%	55%	0%	30%	26%	0%	30%	55%
Water	46%	32%	21%	49%	34%	22%	57%	40%	22%	65%	46%	29%

Table 3.2 Properties of cements and sand

	Specific Gravity	Absorption
OPC	3.15	-
CSC	2.85	-
ASTM C778 Ottawa Sand	2.65	0%

Table 3.3 Status of data collection from MIP and SEM analyses

Analysis	0.3 CSC			0.3 OPC (PC)			0.42 OPC (PC)			0.6 OPC (PC)		
	0.3C0	0.3C30	0.3C55	0.3P0	0.3P30	0.3P55	0.42P0	0.42P30	0.42P55	0.6P0	0.6P30	0.6P55
MIP	○	○	○	○	○	○	○	○	○	○	○	○
SEM	○	○	○	○	○	○	×	×	×	×	×	×

○ – data obtained and × – no data

3.2.1 Mercury intrusion porosimetry (MIP)

Mercury intrusion porosimetry (MIP) is a well-known technique that can measure a wide range of pore sizes, from 3 nm to 360 μm . This technique is based on the concepts of fluid dynamics and capillary hydrostatics that are applied to the properties of mercury. Mercury has a non-wetting characteristic toward many solids; thus, mercury can be intruded into hardened cement paste under various pressure levels. An individual level of pressure can be converted into a specific pore size by Equation 3.1. L. Edel'man et al. [84] were the first to apply MIP to concrete research. Since this initial work, MIP has been widely used to evaluate the pore size distribution of hardened cement paste. This technique may not provide a true pore size distribution because it assumes that all pores are cylindrical and depend on the size of the pore entrance where mercury intrusion initiates; for example, the large voids with small pore entrances will be detected as the large volume (i.e., the same as the volume of the large voids) of the small pore. However, MIP is relatively easy, quick, and more importantly, it can almost detect an entire range of pore sizes in hardened cement paste as compared to other techniques, such as gas adsorption, water absorption, thermoporometry, nuclear magnetic resonance, optical microscopy, and electron microscopy. The radius of pores is calculated by the E. Washburn equation (Equation 3.1), who derived the equation based on Young and Laplace's work in 1921 [85].

$$r = \frac{2\gamma \cos \theta}{P} \quad \text{Equation 3.1}$$

where r is the radius of the pore (m),

γ is the surface tension of the liquid adsorbate (N/m),

θ is the contact angle between mercury and the pore wall (degrees), and

P is the pressure applied on mercury to intrude the pore (N/m^2).

Each specimen tested by MIP was immersed in water for 28 days after casting. Next, the specimens were dried at 80°C for 24 hours and were then weighed and placed in a penetrometer. Note that ettringite in the hydrated OPC (Type I) sample can decompose at 80°C , which can increase the total porosity volume. However, the increment of porosity due to decomposition of ettringite can be insignificant because the amount of ettringite in the sample at 28 days is almost

negligible as compared to the other OPC hydration products [86], [87]. After being placed in the penetrometer, the specimen was cleaned in the penetrometer by an evacuation process that removed air and adsorbed species inside of the specimen. The cell (the penetrometer with the specimen) was evacuated until the pressure dropped below 0.002 psi (1.3×10^{-4} atm) and then the specimen was pressurized, from 0.55 psi up to 60,000 psi. The Micromeritics AutoPore IV 9500 porosimeter was used in this study. Data points representing pore diameters lower than 0.004 μm (4 nm) were removed from the analysis because of test artifacts that persisted even after data analysis corrections described in the next paragraph.

These data analysis corrections included blank correction to account for the compressibility of the penetrometer, compressibility of the mercury, and the temperature increase resulting from pressurization. Other correction factors that were initially suggested by R. Cook and K. C. Hover [88] were also implemented to account for the volume and the compressibility of the sample (i.e., the so-called differential mercury compression effect and sample compression effect). These additional corrections were applied to the raw mercury intrusion data using the equations listed below:

$$V''_{\text{cHg}} = 0.175(BV_{\text{sample}}) \log_{10} \left(1 + \frac{P}{264,000 \text{psi}} \right) \quad \text{Equation 3.2}$$

where V''_{cHg} is differential mercury compression,

BV_{sample} is bulk volume of the sample, and

p is pressure (psi).

$$V_{\text{cs}} = p(\psi_{\text{sample}})(UV_{\text{sample}}) \quad \text{Equation 3.3}$$

where V_{cs} is sample compression,

p is pressure (psi),

ψ_{sample} is coefficient of compressibility of sample (concrete $\sim 0.7 \times 10^{-7}$ to $\sim 6 \times 10^{-7}$ in²/lb), and

UV_{sample} is volume of the sample without intrusion of mercury.

Thus, the final intrusion of volume of mercury (V_{int}) is

$$V_{\text{int}} = V_o - V_{\text{blank}} + V''_{\text{cHg}} - V_{\text{cs}} \quad \text{Equation 3.4}$$

where V_o is the uncorrected volume reading and V_{blank} is the blank volume readings.

3.2.2 Scanning electron microscope (SEM)

Scanning electron microscope (SEM) was used for imaging of a material's surface in order to investigate the topography, morphology, and composition of materials. In 1983, K. L. Scrivener and P. L. Pratt were the first to use this technique to image morphologies of cement paste [89] and used this technique to quantify pores larger than 50 nm [90]. Since then, this technique has been broadly used to determine the pore structure of cementitious materials by backscattered electron (BE). Unlike MIP analysis, SEM reveals the actual shape and size of pores at microscale without making any assumptions regarding the shape of the pore and calculations. However, SEM can only show the surface of material; thus, the volume of a pore cannot be accurately determined, in contrast to the MIP technique. Thus, in this study, SEM was used to find the location, shapes, and sizes of the pores (2D) in OPC and CSC systems.

The FEI NOVA nanoSEM Field Emission SEM equipped with Through-the-Lens detector (TLD) and Gaseous Analytical Detector (GAD) was used in this study. The probe voltage was set to 10 kV for high-resolution images at a 5 mm working distance, whereas a 10 mm working distance was used for the Energy Disperse X-ray (EDX) mode. Initially, the images were captured at 1,000X magnification and then the images were enlarged to 7,000X magnification to increase pixel resolution. One pixel represents approximately 0.3 μm at 1,000X magnification and 0.05 μm (50 nm) at 7,000X magnification.

Before each sample was placed in the SEM instrument, several sample preparation steps were performed: drying, epoxying, cutting, polishing, and platinum coating. First, each sample was dried in an oven at 80°C for 3 days. Next, each sample was removed from the oven and was then impregnated with a low viscosity epoxy (medium hardness) [91]. Next, each sample was kept in a vacuum desiccator for one day to ensure the quality of the epoxy impregnation. Once the sample was de-aired and the epoxy was impregnated, the sample was placed in an oven at 70°C for at least 6 hours to harden the epoxy. Then, the top 1 mm of the sample was cut using a rotating diamond saw at 50 rpm. Next, the epoxy-impregnated-sample was polished using the following abrasive diamond discs: 45 μm , 30 μm , 15 μm , 9 μm , 6 μm , 3 μm , 1 μm , and 0.25 μm . The sample was subjected to grinding on each disc for 8 minutes (1 minute for every 90-degree rotation). During polishing, the sample was cleaned with acetone at least every 2 minutes. Finally, the polished sample was coated with platinum for 60 s using a Cressington turbo-pumped sputter coater.

3.2.3 Image J analysis

Image J is widely used in a variety of research areas that require analysis of sizes and shapes of objects in images. Image J counts the number of pixels and the arrangement of pixels. Image J supports multiple image formats (TIFF, JPEG, BMP, PNG, and others). Particularly in the area of cement and concrete research, this software can be useful for measuring air voids and pore size distributions. Once images are acquired from various sources (e.g., scanners, optical microscopes, scanning acoustic microscope, and SEM), the images are pre-processed by Image J based on the individual's interest. In this study, the following procedures were adopted. Initially, the images were set to 8-bit and 73-threshold level. Next, the images were changed to binary images (i.e., black and white) in order to define the black and white regions as pores and solids, respectively. Then, the areas of all individual pores were measured using the Analyze Particles function in Image J. For this study, Image J 1.51j8 was downloaded from "<https://imagej.nih.gov/ij>" and the TIFF image format was used. At least 25 images at 7,000X magnification were analyzed in order to reduce type I error of t-distribution. Also, an area that was constructed by one pixel was considered to be noise and was discarded in the final analysis.

3.2.4 Thermal gravimetric analysis (TGA)

Each sample was ground by a mortar and pestle, and then the ground powers were sieved through a #200 sieve to increase the precision of the results. TGA was used to confirm the degree of carbonation of each CSC sample. The mass of the powder sample was recorded while the sample was exposed to increasing temperature, from 23 to 1000°C. According to the stoichiometries (Equation 2.5-Equation 2.7), wollastonite, rankinite, and belite capture 27.5%, 31.4%, and 33.8% CO₂ by weight, respectively. In this study, the CSC paste regularly stored 12~13% CO₂ by weight after carbonation; Ashraf reported (Chapter 3, [49]) that wollastonite, rankinite, and γ -belite stored 19.23%, 20.21%, and 20.27% CO₂ by weight, respectively, after 80 hours of carbonation (curing at 100% CO₂ concentration, 55°C, and 94% RH).

3.2.5 Dynamic vapor sorption (DVS)

In general, DVS is used to detect nano-sized pores with a pore radius below 40 nm according to the Kelvin equation (Equation 2.13). However, in this study, this technique was

performed to verify the changes in pores before and after the removal of carbonation products in the CSC system. Samples of 1 mm thickness were prepared using the carbonation curing regime (60°C, >80% RH, and 20% CO₂ for 7 days). Once curing was complete, each sample was kept in deionized water (under vacuum) for 2 days to saturate the samples before running DVS. The individual steps for RH (desorption) were 97.5, 94, 90, 85, 80, 75, 70, 60, 50, 40, 30, 20, 11, 5, and 0%; the adsorption process was conducted in the opposite order. The device maintained the RH level at each step until the mass of the sample was stabilized to within 0.001% of mass change (tolerance level).

3.3 Results and discussion

3.3.1 Changes in the porosity of CSC paste with various w/c

Water-to-cement ratio was varied in order to identify changes in porosity and to calculate how much water will evaporate after the carbonation reaction. In this experiment, the mass of the specimen after 7 days of carbonation (60°C, greater than 80% RH, and 20% CO₂) was recorded at three different moisture contents: 50% RH (at 23°C for 14 days), vacuum saturation (for a day), and oven-dry (at 105°C for three days). A total of six replicates (1~2 mm thickness) were made for each w/c of the specimen. A summary of the results is shown in Table 3.4. As water-to-cement ratio increased, the total porosity of the carbonated CSC paste increased. Total porosity was calculated as the mass of the absorbed water divided by the oven-dry mass of the sample. Approximately, 1.2~1.35% of the pores were filled with water at 50% RH, which indicates that 6~7% of the total porosity in CSC paste were gel and small capillary pores (diameter less than 4 nm). The volume of this range of pores was similar to the volume of the chemically bound water in CSC paste reported by Ashraf et al. [79]. In other words, 1 g of CSC was able to bind 0.012~0.0135 g of water.

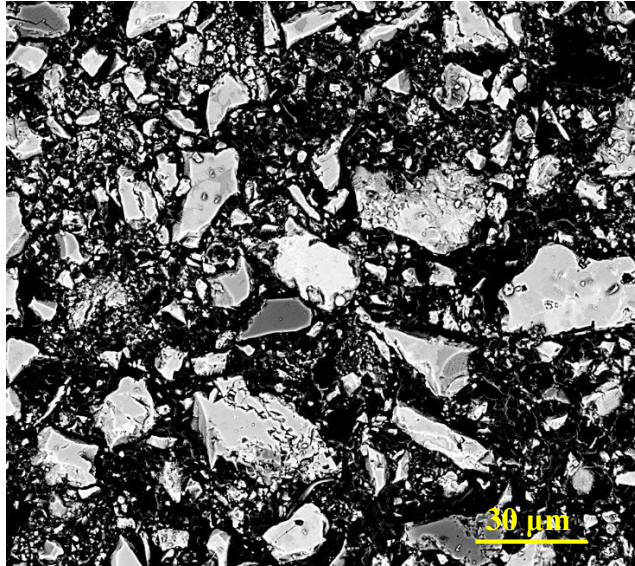
Table 3.4 Summary of porosity of the CSC pastes with various w/c

w/c	before carbonation		after carbonation					
	type	mass (g)	mass of specimen (g)		absorption		stored at 50%RH	
			saturation	oven-dry.	water (g)	porosity (%)	water (g)	empty pores (%)
0.3	CSC	15.3701	20.7198	17.6864	3.0334	17.15	0.2092	15.97
	water	4.6110						
0.35	CSC	14.2691	19.6705	16.5793	3.0912	18.64	0.2239	17.29
	water	4.9945						
0.4	CSC	13.3198	18.8598	15.4130	3.4468	22.36	0.2024	21.05
	water	5.3279						

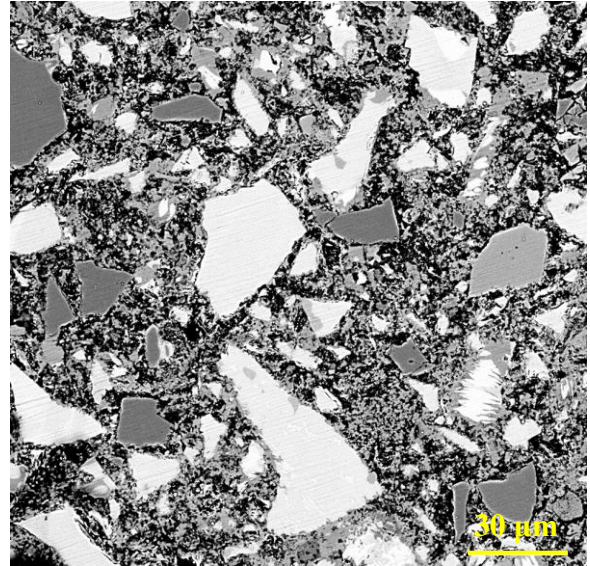
3.3.2 Changes in the porosity of CSC paste after carbonation

An uncarbonated sample was prepared in order to investigate the change of porosity before and after the carbonation of CSC pastes. Two samples were prepared for before and after carbonation. A direct comparison of the same sample was unattainable in this case because of the process of SEM sample preparation that involved epoxy impregnation. Thus, SEM images had to be collected from two different samples. In Figure 3.1, the black area represents the porosity of the specimens. Also, the grey and white tones indicate the CSC particles and carbonation products. The images in Figure 3.1 were changed to binary images via Image J, as shown in Figure 3.2 (a) and (b), in order to analyze the porosity of the specimen. Based on Image J analysis, the porosity of uncarbonated CSC paste was estimated to be approximately 56%, which was assumed as the volume of mixing water. Initially, the total volume of uncarbonated CSC paste was supposed to contain approximately 54% of the CSC particles (S.G. 2.85) and approximately 46% of the mixing water (S.G. 1), as shown in Table 3.1. After carbonation, the porosity, initially filled with the mixing water, was filled with carbonation products, which reduced the porosity of CSC paste. The carbonation products consist of calcium carbonates and silica gel. According to Ashraf et al. [52], these are Ca-modified silica gel, composite phase, and calcium carbonate.

As shown in Figure 3.2 (c), the total porosity was reduced from 56% to 20% when the carbonated specimen contained approximately 30% calcium carbonates by weight. The area of the largest single void in uncarbonated CSC paste was $14,700 \mu\text{m}^2$; the void started to break into smaller pores with the growth of calcium carbonates. The small pore area created by carbonation products was well-distributed within a range of 0.003 to $204 \mu\text{m}^2$.

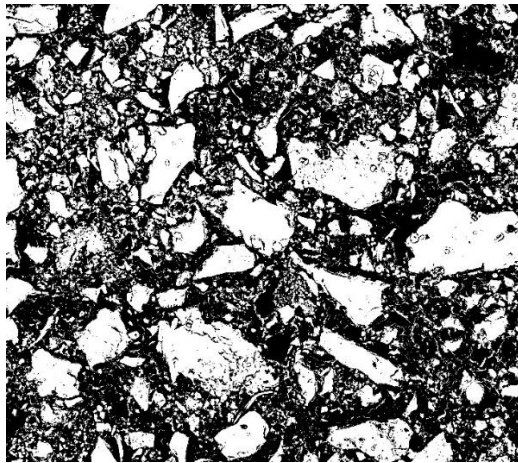


(a) uncarbonated CSC paste ($173 \times 153 \mu\text{m}^2$)

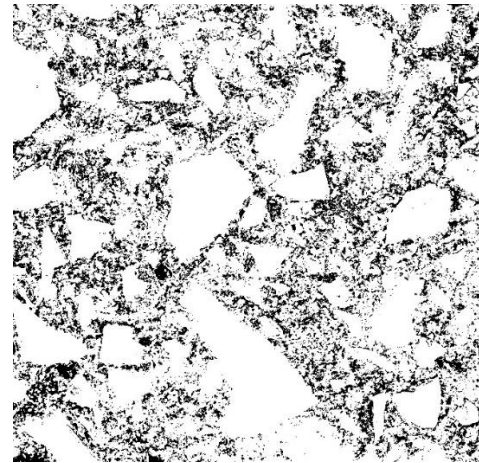


(b) carbonated CSC paste ($174 \times 174 \mu\text{m}^2$)

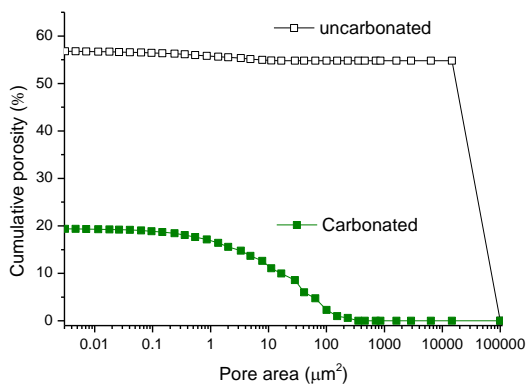
Figure 3.1 SEM images of the CSC pastes



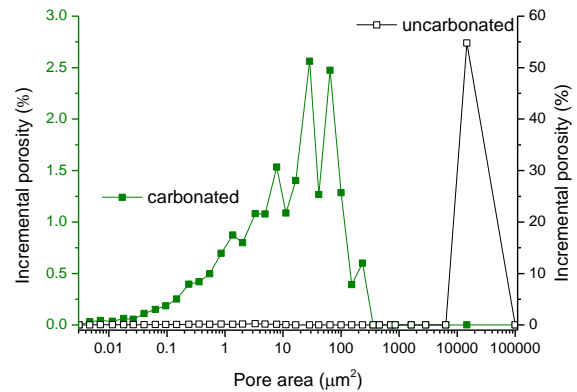
(a) uncarbonated CSC paste (Image J)



(b) carbonated CSC paste (Image J)



(c) cumulative porosity of CSC pastes

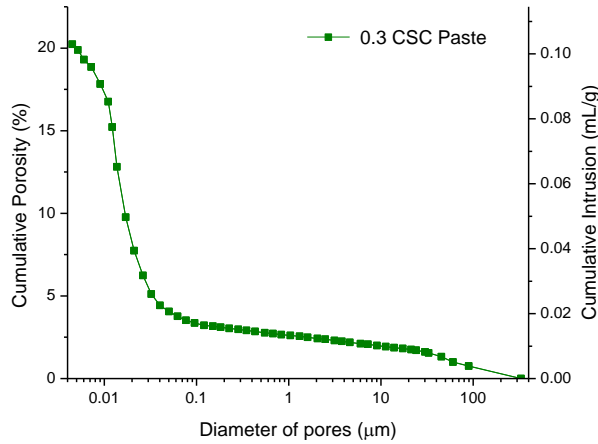


(d) pore area distribution of CSC pastes

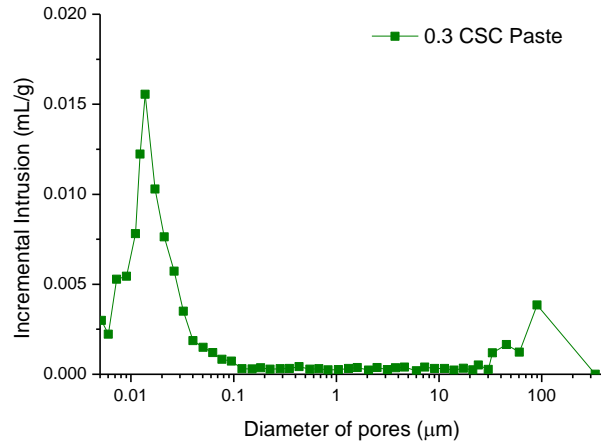
Figure 3.2 Image J analysis – cumulative porosity and pore area distribution of CSC pastes

3.3.3 The pore size distribution of carbonated CSC paste

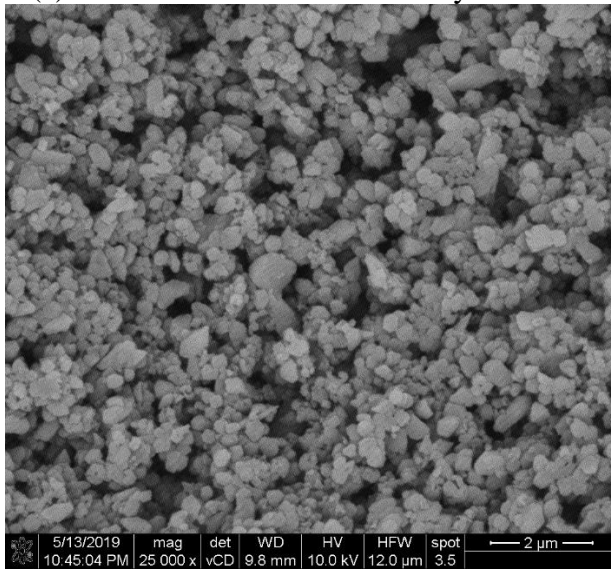
As shown in Figure 3.3 (b), two distinctive regions in carbonated CSC paste were found: small capillary pores (5 nm ~ 100 nm) and large capillary pores (30 μm ~ 100 μm). The small capillary pores were found in carbonation products (Figure 3.3 (c)), and the large capillary pores were found in the bulk matrix that had no carbonation products (Figure 3.3 (d)). The pore diameter threshold was 0.04 μm (40 nm).



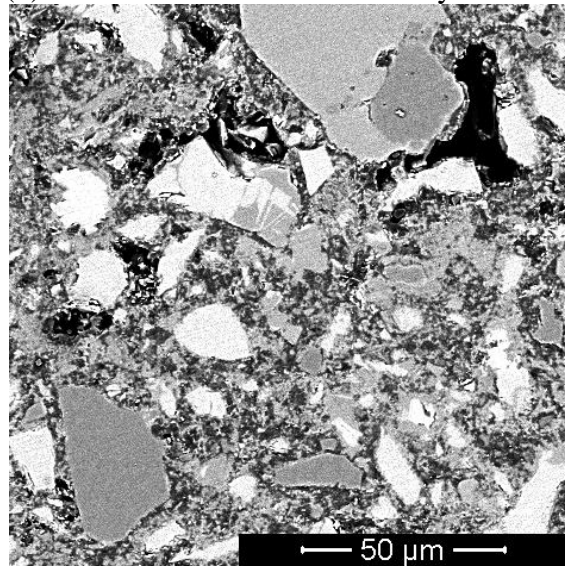
(a) cumulative volume of mercury intrusion



(b) incremental volume of mercury intrusion



(c) crystals of calcium carbonates (SE)

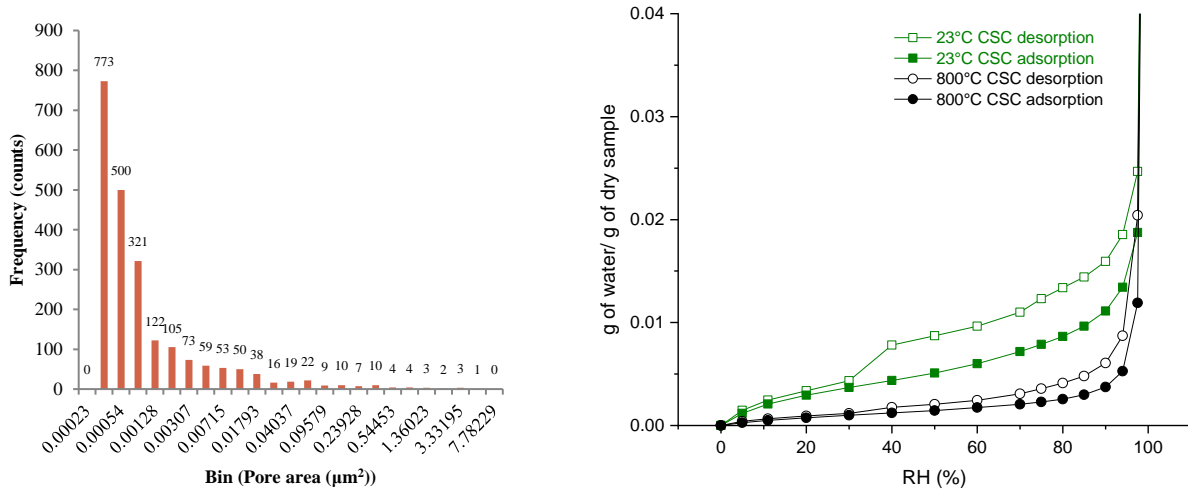


(d) large capillary pores in CSC paste (BSE)

Figure 3.3 MIP results-(a)&(b), and SEM images-(c)&(d) of 0.3 w/c CSC paste

In addition, desorption isotherm curves (Figure 3.4 (b)) showed that the volume of small capillary pores (0.8 ~ 80 nm in pore diameter) in 0.3 CSC paste was 1.9% (0.01874 g of water per g of dry CSC paste). However, this volume of pores was reduced to 1.2% (0.01191 g of

water per g of dry CSC paste) after the decomposition of carbonation products at 800°C; the calcium carbonates decompose completely at temperatures above 750°C (Figure 3.5 (c)). This indicates that a range of pore diameters between 0.8 ~ 80 nm was present in carbonation products of CSC paste. Also, the gap between desorption and adsorption isotherms after decomposition of the carbonation products was almost negligible, which reflects the collapse (decomposition) of the bulk volume of amorphous and crystalline calcium carbonates.



(a) Histogram (Image J) on Figure 3.3 (c) (b) adsorption and desorption isotherms
Figure 3.4 Pore characteristics in carbonation products of CSC paste

3.3.4 Pore size distribution and porosity in ITZ of carbonated CSC mortars

As aggregates were integrated into the CSC system, the total volume of mercury intrusion in 0.3C30 (30% aggregates) was reduced to approximately 50% of CSC paste (0.3C0) because of the reduced volume of CSC paste. As a result, the 0.3C30 specimen contained a smaller volume of mercury intrusion in the range below 0.04 μm of pore diameter as compared to CSC paste (0.3C0), because the smaller pores (≤ 0.1 μm) were formed as a result of carbonation. In other words, the total mass loss due to CaCO₃ decomposition decreased as the volume of aggregates increased in the CSC system, as shown in Figure 3.5 (c).

With the presence of aggregates in the cementitious matrix, another phase was introduced that is called the interfacial transition zone (ITZ) between aggregates and the cement paste. As described in Section 2.4.4, ITZ is considered to be a porous and weak part of the matrix that may reduce mechanical performance [92]–[94]. ITZ was also present in the CSC mortar system. Unlike the pore size distribution of other specimens, 0.3C55 (55% aggregates) had a primary

pore range of 0.1 to 4 μm . Also, the total volume of intrusion was slightly higher than the 0.3C30 specimen, although 0.3C55 retained a higher volume of aggregates. This additional pore size range may have been caused by the combined effect of percolation and porous ITZ in CSC mortars depending on the volume of aggregates. Winslow et al. [95] studied OPC mortars (0.4 w/c) containing over 40% sand, which started showing percolation (interconnected pores). Later, Diamond S. [50] described that interconnected pores were due to the highly porous region of paste in the OPC mortar containing 55.4% sand (0.4 w/c) from incomplete consolidation, rather than from the percolated effect.

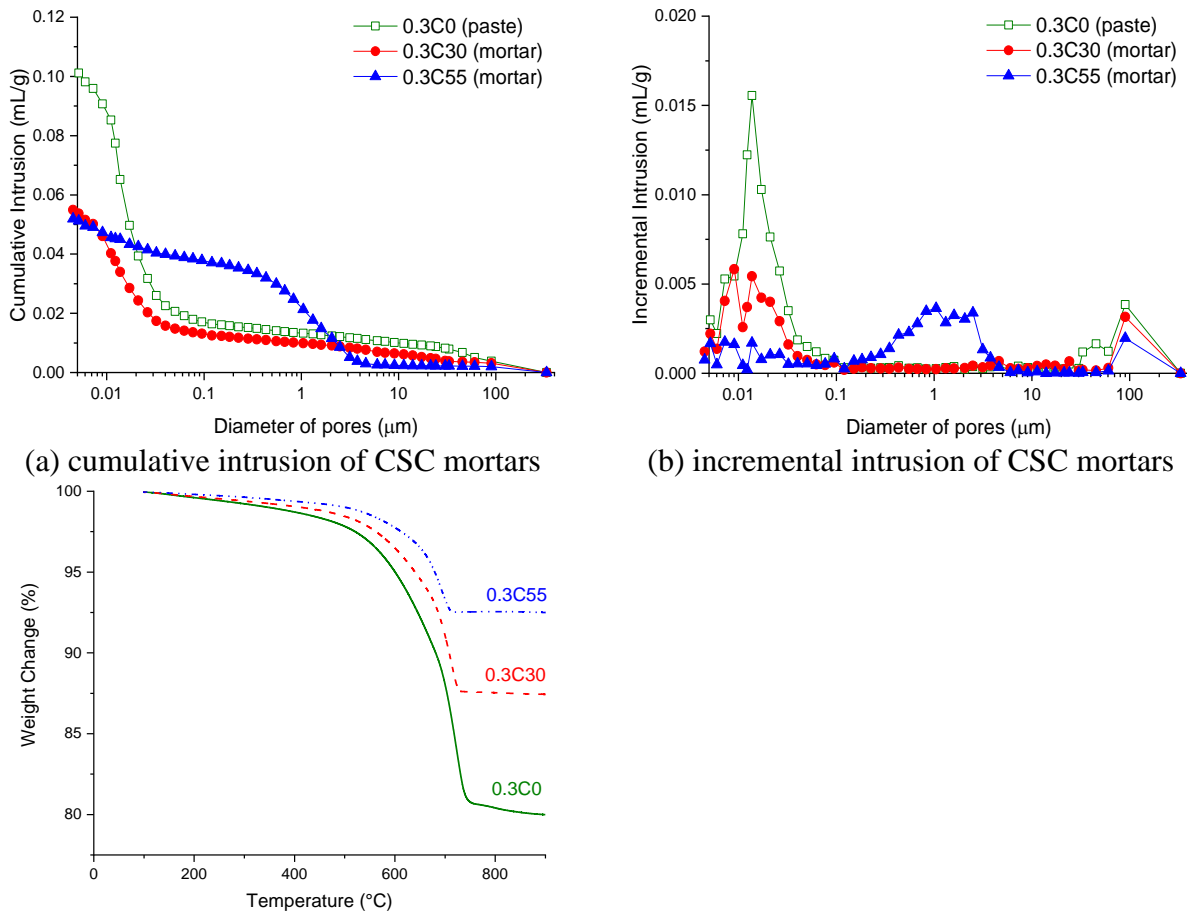
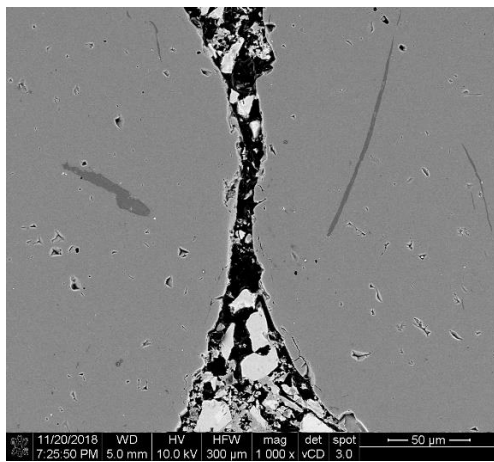


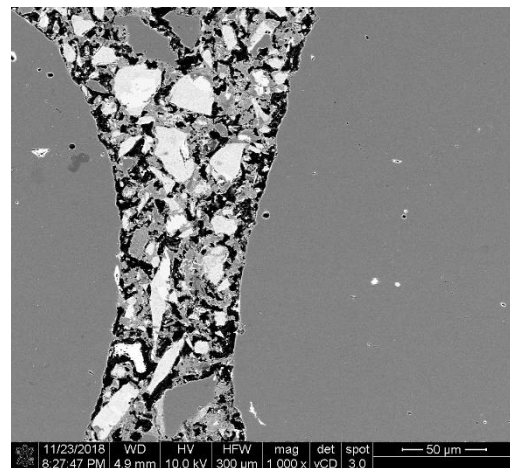
Figure 3.5 MIP (a)&(b), and TGA (c) results of CSC specimens

To verify the pore range (0.1~4 μm) of 0.3C55 mortar, SEM and Image J analyses were performed in the area that was located 50 μm from the aggregates of the CSC mortars (Figure 3.11). The magnification of the SEM images was 1,000X and the pixel resolution was 3.5 pixels/ μm . As shown in Figure 3.6, the porosity between aggregates increased as the distance

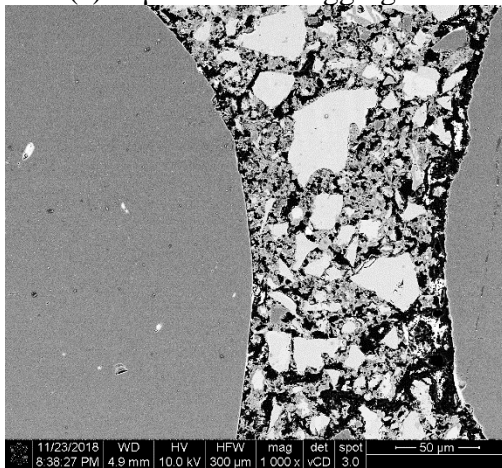
between aggregates decreased. When the distance between aggregates was within 10 μm , the percolation was present, which decreased as the distance increased; however, percolation was not found in CSC mortar containing 30% aggregate because the specimen did not contain enough aggregate. Instead of percolation, the wall effect appeared to be critical in CSC mortar specimens, irrespective of the volume of aggregates due to the non-hydraulic characteristic of CSC, as hypothesized in Section 3.1. Therefore, the water filled space between the aggregates and CSC particles became pores after carbonation due to an exothermic reaction and high curing temperature; only 6~7% of the total porosity was comprised of the small capillary pores that may be chemically bound water, as mentioned in Section 3.3.1.



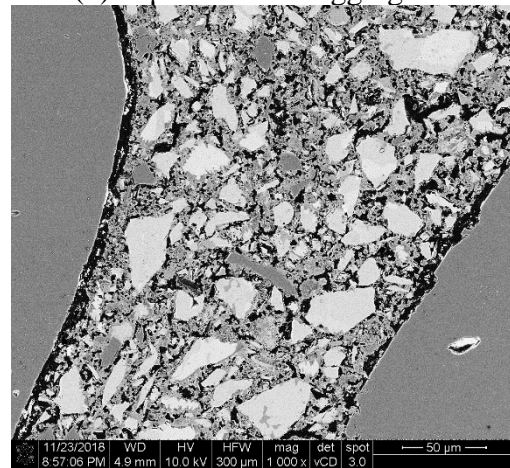
(a) 10 μm between aggregates



(b) 50 μm between aggregates



(c) 100 μm between aggregates

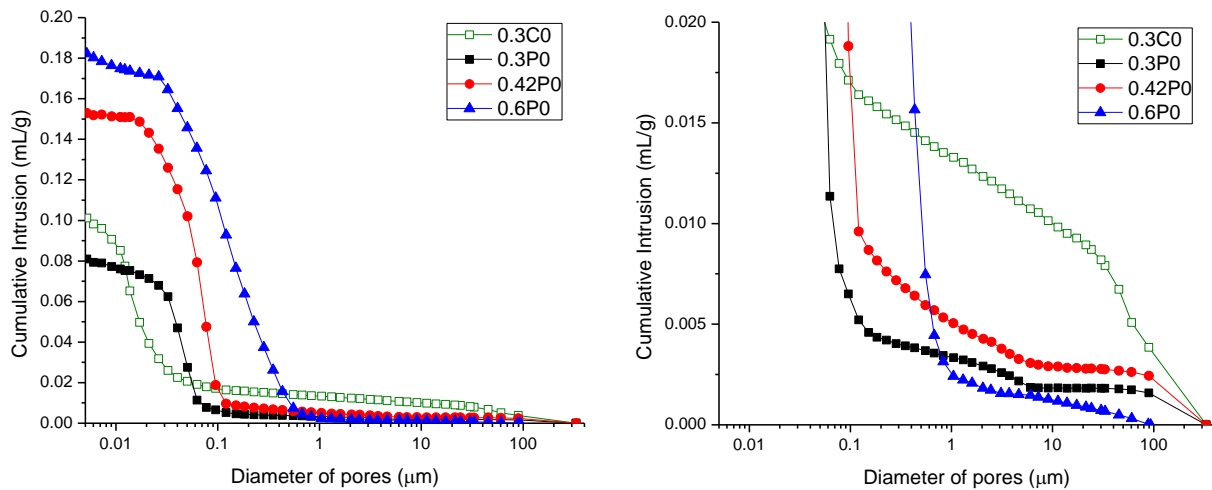


(d) 150 μm between aggregates

Figure 3.6 Percolation and wall effects in ITZ of CSC containing 55% aggregates (0.3w/c)

3.3.5 Comparison to the OPC system

With the same water-to-cement ratio (0.3 w/c), the CSC paste (0.3C0) had a 0.02 mL/g higher volume of porosity as compared to the OPC paste (0.3P0) and, additionally, the pore range of the CSC paste was different than the range of the OPC paste. CSC contained a higher volume of pores that were below 30 nm and above 20 μm in size; whilst the primary pore range of OPC paste was between 10 nm to 0.1 μm . Also, the threshold pore diameter of the CSC paste (~ 25 nm) was smaller than that of the OPC paste (~ 65 nm). Before the pressure of mercury intrusion reached the threshold diameters of each paste specimen, it was found that the mercury in CSC paste gradually intruded into the pores (> 0.1 μm) while the mercury started to intrude OPC paste at pore openings smaller than 5 μm (Figure 3.7 (b)). This indicates that the pore network of CSC paste was more likely interconnected throughout the whole range of pore diameters as compared to OPC paste. Also, as the w/c of OPC increased, the threshold pore diameter and the connectivity of the pore network increased. In general, the connectivity of the pore network was significantly affected by the volume of the capillary pores [96]; 0.3C0 contained a larger volume of capillary pores as compared to 0.3P0.



(a) cumulative intrusions in pastes

(b) magnified view of (a) below 0.02mL/g

Figure 3.7 Cumulative mercury intrusions of CSC and OPC pastes

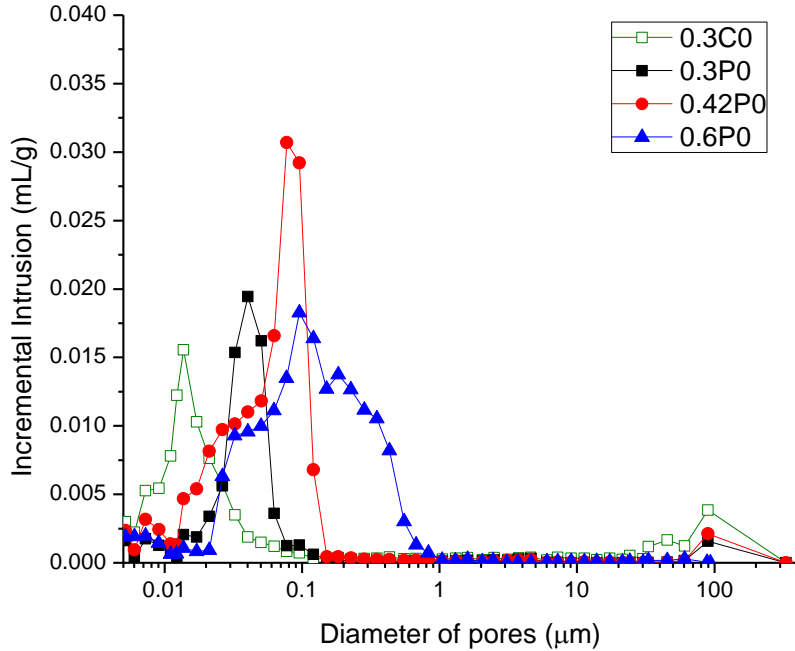
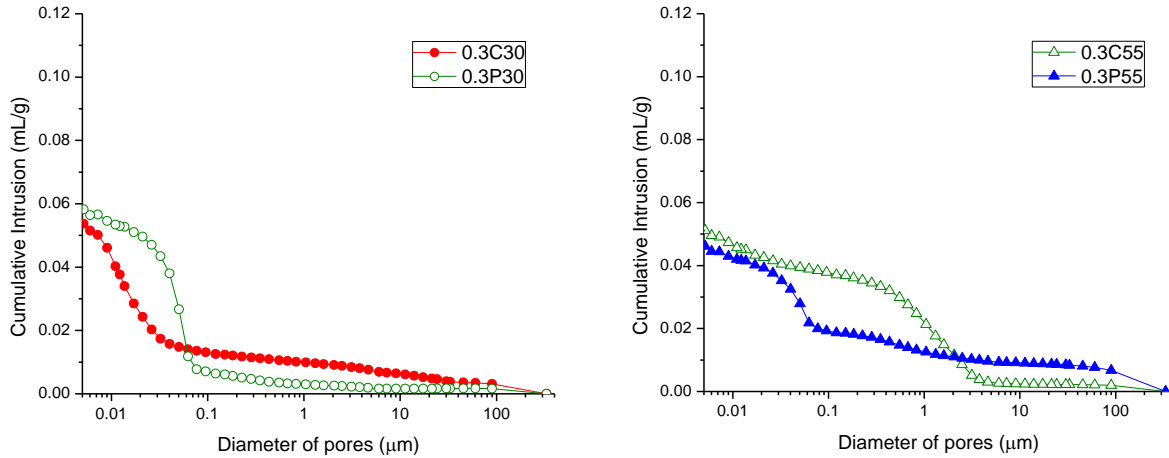


Figure 3.8 Incremental mercury intrusions of CSC and OPC pastes

Unlike the paste specimens, the difference between CSC and OPC mortars for total volume of mercury intrusion was nearly negligible. Additionally, when the mortars contained 30% aggregates by volume, the threshold pore diameter did not change from the threshold value of the paste specimens. However, with 55% aggregates in the CSC mortar, larger threshold values were detected because of the wall and percolation effects [95], which increase the connectivity of pore networks [97]. As mentioned previously, the wall and percolation effects in CSC mortar containing 55% aggregates created a higher volume of larger pores as compared to the OPC mortar containing 55% aggregates. As a result of these effects, the resulting pore ranges for 0.3C55 and 0.3P55 were 0.1~4 μm and 0.7~1 μm , respectively. Also, the CSC mortars contained more porous ITZ as compared to the OPC mortars, as shown in Figure 3.11 and Table 3.5.



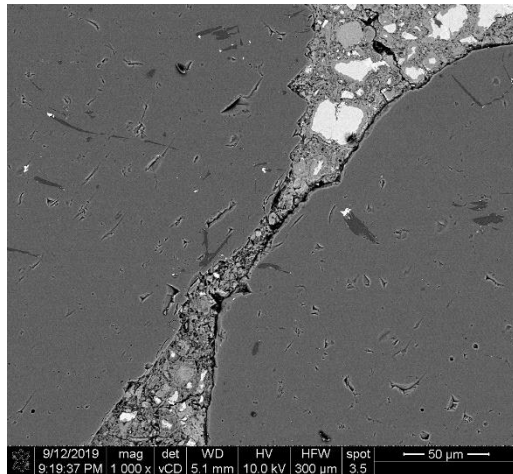
(a) mortars containing 30% aggregates

(b) mortars containing 55% aggregates

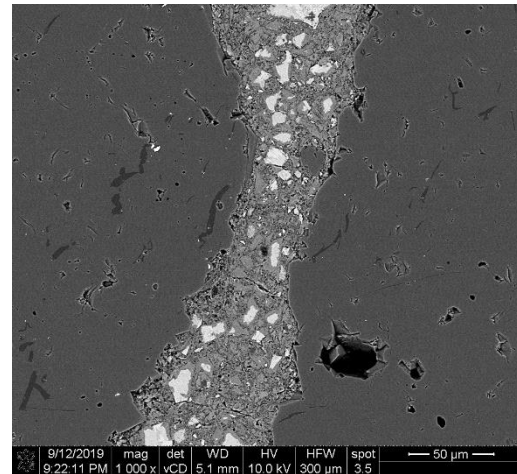
Figure 3.9 MIP results from CSC and OPC mortars (30% and 55% aggregates)

Because the actual pore size distribution may not be detected by the MIP technique, as described in Section 3.2.1, SEM and Image J analyses were required to obtain more detailed information of the surrounding ITZ within 50 μm from the aggregate (Figure 3.11). The porosity at every 10 μm from the aggregate was determined by Image J analysis and the results are shown in Table 3.5. SEM images at 7,000X and 5,000X magnification were used for the distance between 0~20 μm and 20~50 μm, respectively.

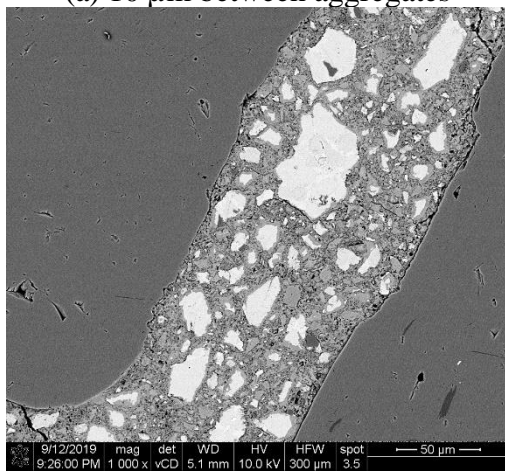
Both types of mortars contained a relatively highly porous area within a 10 μm distance from the aggregate because of the wall effect; however, the effect seemed to be more critical for the CSC mortars as compared to the OPC mortars. As the location of cement paste moved further from the aggregates, the cement pastes tended to contain less porosity. Also, in the OPC system, several micro-cracks were found around the aggregate due to autogenous shrinkage of cement paste [98], but these cracks were not found in the CSC system. Nonetheless, the CSC system contained larger sizes and irregular shapes of pores near ITZ (Figure 3.12 (a) and Figure 3.12 (c)). This finding leads to the point that the wall and percolation effects on CSC mortars are observed more often, especially when the distance between aggregates was narrow (within 10 μm), as shown in Figure 3.6 and Figure 3.10.



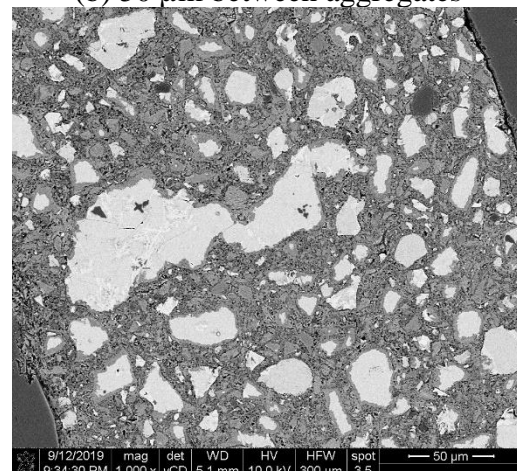
(a) 10 μm between aggregates



(b) 50 μm between aggregates



(c) 100 μm between aggregates

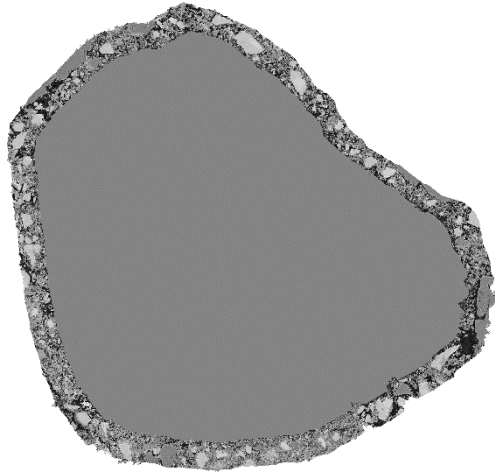


(d) 200 μm between aggregates

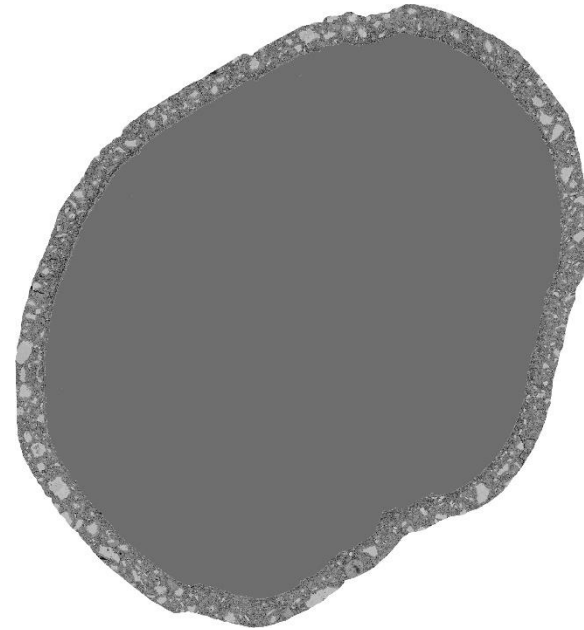
Figure 3.10 Percolation and wall effects in ITZ of 0.3P55

Table 3.5 Porosity in ITZ of CSC and OPC mortars

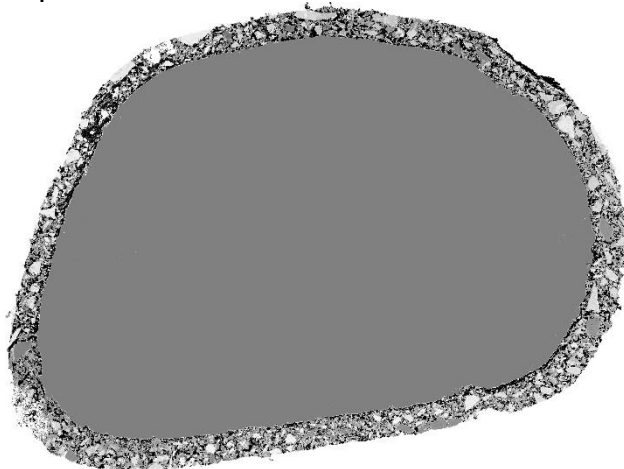
Distance (μm)	Specimens			
	0.3C30	0.3P30	0.3C55	0.3P55
	Porosity (%)			
~10	34.80	20.77	40.29	22.00
10~20	25.81	14.04	26.09	11.30
20~30	23.75	10.70	23.85	9.51
30~40	23.36	11.29	20.87	8.49
40~50	20.73	11.62	20.87	7.80



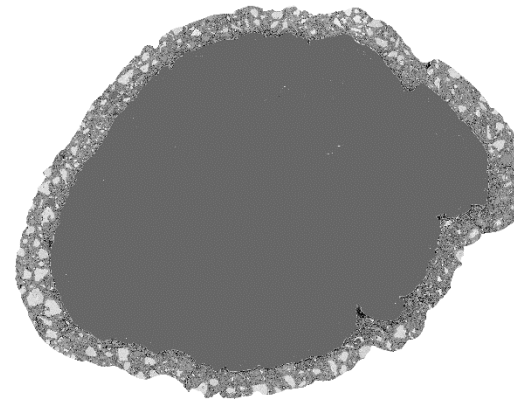
(a) 50 μm thickness of interfacial zone in 0.3C30 mortar



(b) 50 μm thickness of interfacial zone in 0.3P30 mortar

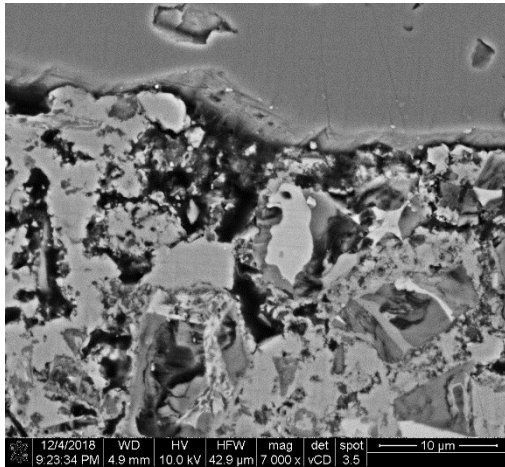


(c) 50 μm thickness of interfacial zone in 0.3C55 mortar

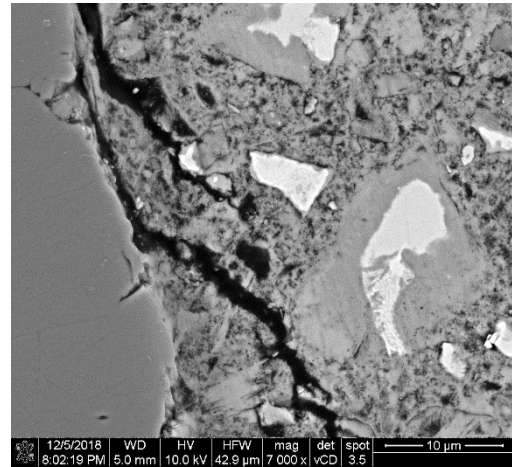


(d) 50 μm thickness of interfacial zone in 0.3P55 mortar

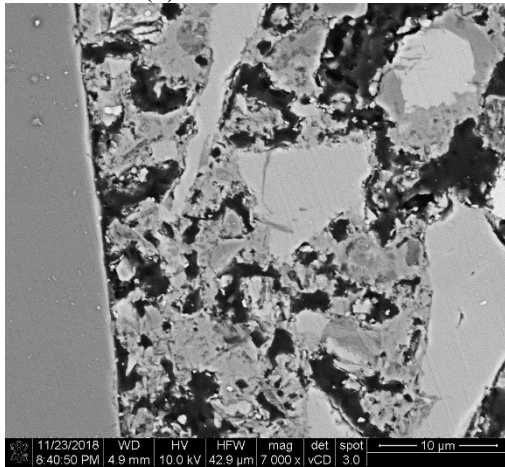
Figure 3.11 General view of 50 μm thickness of ITZ in mortar specimens



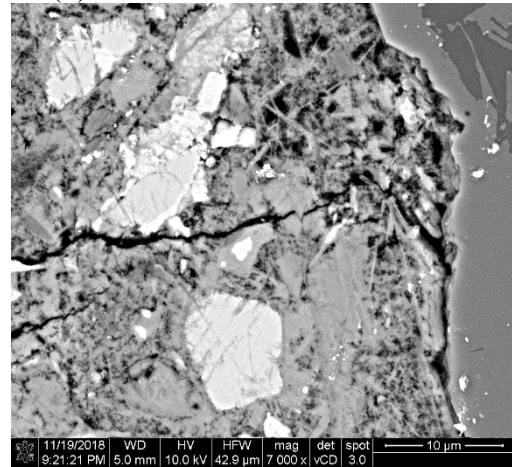
(a) 0.3C30 mortar



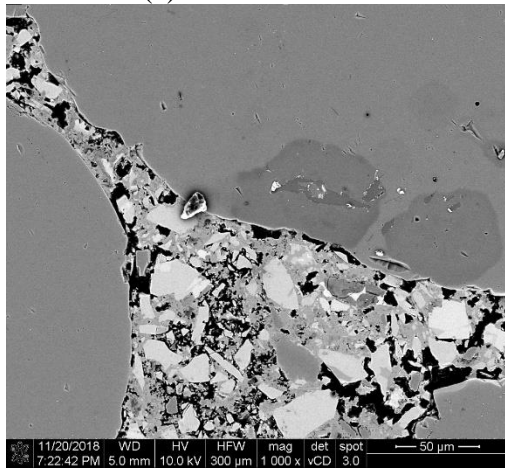
(b) microcracks in 0.3P30 mortar



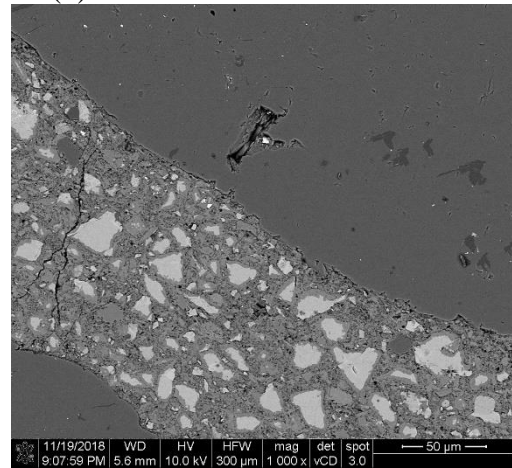
(c) 0.3C55 mortar



(b) microcracks in 0.3P55 mortar



(e) 0.3C55 mortar



(f) microcracks in 0.3P55 mortar

Figure 3.12 ITZs of CSC (left side) and OPC (right side) mortars

3.4 Conclusions

In this chapter, the pore system of the CSC paste and mortars was characterized based on the results of MIP, SEM, and Image J analyses. Before carbonation curing, the mixing water occupied 46% of the total volume of the CSC paste (0.3 w/c) and the porosity (the area of impregnated epoxy) consisted of approximately 56% uncarbonated CSC paste. This large porosity became filled with carbonation products as the carbonation curing continued. The porosity had been reduced to 20% at the completion of carbonation curing. Carbon and CSC paste had two distinct regions within their pore size distribution: one below 0.1 μm and another greater than 30 μm . Small capillary pores were found in the carbonation products and large capillary pores were found in bulk matrix.

As the volume of aggregates in the CSC mortar increased, the total porosity significantly decreased. The 0.3C55 mortar contained distinctive pores (0.1~4 μm) because of the combined effects of the wall and percolation; the percolation effect only was observed within 10 μm of thickness from the aggregates. As the distance from the aggregates increased, the porosity of the cement paste resulting from the wall or percolation effect was diminished. Due to this tendency, the ITZ of CSC mortar specimens contained much higher porosity as compared to OPC mortars.

In terms of pore connectivity, the CSC system was more interconnected because of the large volume of capillary pores in bulk matrix and porous ITZ as compared to the OPC system; the pores in 0.3 w/c OPC were mainly gel and small capillary pores (less than 65 nm). This unique pore characteristic of the CSC system could affect not only the rate of water absorption but also freeze-thaw resistance, which can directly impact the durability performance of CSC. Thus, the evaluation of sorptivity and freeze-thaw resistance of CSC-based materials are necessary in order to evaluate the effect of pore characteristics on the durability of the CSC system.

4. THE RATE OF WATER ABSORPTION OF CARBONATED CSC SYSTEMS AND THE RELATIONSHIP WITH FREEZE-THAW RESISTANCE

4.1 Motivations and objectives

As discussed in the previous chapter, the CSC system attained a high volume of large capillary pores and pore connectivity because of the carbonation of CSC and the porous ITZ. The mixing water leaves the CSC system due to the carbonation reaction (exothermic) and the non-hydraulic characteristics of CSC, which results in a high volume of capillary pores, although some of the water was bound to carbonation products (silica gel and amorphous calcium carbonates) [49], [79]. Because of the high volume of large capillary pores, the CSC system would have a different rate of water absorption (sorptivity) as compared to the OPC system if both systems have the same water-to-cement ratio. It is assumed that unsaturated the CSC system absorbs water faster than the OPC system.

In this chapter, the discussion of the rate of water absorption of CSC paste and mortars is based on the results from ASTM C1585 [99], which estimates the susceptibility of an unsaturated CSC system to the penetration of water. This absorption behavior is significantly affected by the characteristics of the material of the pore system (i.e., volume of capillary pores and pore connectivity); hence it is often used to indicate durability performance of such fluid transport properties, electrical resistivity, and freeze-thaw resistance of the cementitious materials [28], [67], [100]-[103]. Freeze-thaw resistance can be easily predicted by the rate of water absorption (critical saturation level), as described in Section 2.6.2.2. In the case of the CSC system, the rate of water absorption is expected to be high because of the high volume of capillary pores and pore connectivity.

Thus, to correlate the rate of water absorption with freeze-thaw performance, freeze-thaw resistance of CSC paste and mortars was studied and compared to the OPC system. Additional test specimens were prepared in order to inspect the effectiveness of an air entrainment agent (AEA) in the CSC system. Generally, in the OPC system, entrained air (i.e., air bubbles of a few hundred microns) provides better resistance to freeze-thaw conditions not only because it relieves the internal stress from ice formation but also it slows the rate of water absorption. In other words, bubbles of entrained air delay the time to reach the peak saturation level.

4.2 Materials and methods

The same mixture design shown in Table 3.1 was used. Additionally, the properties of the materials were the same as those shown in Table 3.2. In the case of the specimens with the air entraining agent (AEA), the dosage of AEA for each mixture was 30 ml/cwt. Additionally, to improve the workability of the mixtures (except the 0.6OPC series), superplasticizer was used at a dosage of 70 ml/cwt.

Table 4.1 Test matrix and number of specimens

Type of specimen	Label		Experiment & # of specimens	
	Non-AE*	AE**	Sorptivity ASTM C1585	F/T resistance
0.3 CSC paste	0.3C0	0.3C0A	3	3
0.3 CSC 30% agg.	0.3C30	0.3C30A	3	3
0.3 CSC 55% agg.	0.3C55	0.3C55A	3	3
0.3 OPC paste	0.3P0	0.3P0A	3	3
0.3 OPC 30% agg.	0.3P30	0.3P30A	3	3
0.3 OPC 55% agg,	0.3P55	0.3P55A	3	3
0.42 OPC paste	0.42P0	0.42P0A	3	3
0.42 OPC 30% agg.	0.42P30	0.42P30A	3	3
0.42 OPC 55% agg,	0.42P55	0.42P55A	3	3
0.6 OPC paste	0.6P0	0.6P0A	3	3
0.6 OPC 30% agg.	0.6P30	0.6P30A	3	3
0.6 OPC 55% agg,	0.6P55	0.6P55A	3	3

*Non-AE: non-air entrained and ** AE: air entrained

4.2.1 Rate of absorption of water (sorptivity) test of paste and mortar specimens

Disc molds (4”(d)×2”(h)) were prepared for this test. OPC specimens were cast in the molds and plastic wrap was used to cover the top of the specimens. In the case of CSC, the specimens were stored in a carbonation chamber (65°C, 60~65% RH, and highly pure CO₂ at a pressure of 1 atm) without a plastic wrap cover for one day. Both types of specimens were demolded one day after casting. After demolding, OPC specimens were stored in a moist curing room (23°C and 98 ± 2% RH) for another 27 days and CSC specimens were stored in the carbonation chamber for 6 days. Once carbonation curing was complete, the CSC specimens were shipped to the Purdue Construction Materials Lab (i.e., Pankow lab). Upon arrival, the specimens were kept in a moist curing room as OPC specimens. Once both types of specimens had aged for 28 days after casting, the specimens were kept in an oven (50 ± 2°C and 80 ± 3%

RH) with saturated potassium bromide for 3 days; the potassium bromide did not contact the specimens. After three days in the oven, both specimens were placed in an environmental chamber (23°C and 50% RH) for at least 15 days. During this curing stage, the side surfaces of the specimens were sealed with epoxy that is used for coating steel rebars. Then, plastic wrap was used to cover the top surfaces of the specimens that was held in position with elastic bands. While the specimens were curing, a water container was prepared and the level of water was set according to ASTM C1585 [99]. Once all the specimens were ready for the test, the initial mass of the specimens was measured and were immediately exposed to the water in the containers that had been prepared in advance. The measurement time interval was based on ASTM C1585 [99]. Absorption was calculated by

$$I = \frac{m_t}{a \times d} \quad \text{Equation 4.1}$$

where I is the absorption, in mm,

m_t is the change in specimen mass in grams, at the time t,

a is the exposed area of the specimen, in mm², and

d is the density of the water in g/mm³.

To estimate initial absorption, the points measured up to 6 hours used and I (initial absorption) was calculated by

$$I = S_i \sqrt{t} + b_i \quad \text{Equation 4.2}$$

where I is the absorption,

S_i is the initial rate of absorption (initial sorptivity).

And for the secondary absorption, the points measured after the first day were collected and I (secondary absorption) was calculated by

$$I = S_s \sqrt{t} + b_s \quad \text{Equation 4.3}$$

where S_s is the secondary rate of absorption.

4.2.2 Low temperature differential scanning calorimetry (LT-DSC)

This technique is based on the same mechanism as differential scanning calorimetry (DSC), which is widely used in cement chemistry, but the temperature range of LT-DSC includes negative temperatures in Celsius. In this study, to measure the amount of freezable water in the CSC system, DSC-Q2000 manufactured from TA instruments and a temperature range of -80°C

to 23°C were used. The heating and cooling rates in the test was 0.05°C/sec. Sample preparation was the same as what was done for the DVS test.

4.2.3 Freezing-thawing (F/T) experiment for paste and mortar specimens

Both OPC and CSC pastes and mortars were cast in 2”(w) × 6”(l) × 1”(h) molds and the molds were removed one day after casting. Prior to the freezing-thawing test, the specimens were exposed to different curing regimes depending on the type of cement. OPC specimens were stored in the moist curing room (23°C and 100% RH) for 27 days; however, the curing regime from ASTM C666 recommends 14 days of moist curing [104]. CSC specimens were cured in the carbonation chamber (65°C, 60~65% RH, and high purity CO₂ at a pressure of 1 atm) for another 6 days and the specimens were shipped from Solidia Technologies (the CSC specimens for this test were provided by Solidia Technologies). After the specimens arrived at the Purdue Construction Materials Lab (Pankow lab), the CSC specimens were stored in the moist curing room until the test started.

Once the specimens were ready for the test, the specimens were immediately removed from the moist curing room and the initial mass and resonant frequency (transverse mode) were recorded according to ASTM C215 [105]. These measurements were recorded at least every 28 F/T cycles. ASTM E 1876 [106] was used to evaluate the dynamic modulus of elasticity to consider the mass variation and the equations are shown below:

$$E = 0.9465 \times (m \times f_f^2 / b) \times (L^3 / t^3) \times T_1 \quad \text{Equation 4.4}$$

where,

E – Young’s Modulus, Pa,

m – Mass of the specimen, g,

b – Width of the specimen, mm,

L – Length of the specimen, mm,

t – Thickness of the specimen, mm,

f_f – Fundamental resonant frequency of the specimen in flexure, Hz, and

T₁ – Correction factor for fundamental flexural mode to account for finite thickness of specimen, Poisson’s ratio (μ = 0.19):

$$T_1 = 1 + 6.585 \times (1 + 0.0752 \times \mu^2) \times (t/L)^4 - 0.868 \times (t/L)^4$$

$$- \frac{8.340 \times (1 + 0.2023 \times \mu + 2.173 \times \mu^2) \times (t/L)^4}{1 + 6.338 \times (1 + 0.1408 \times \mu + 1.536 \times \mu^2) \times (t/L)^2}$$

Equation 4.5

Following Equation 4.4 and Equation 4.5, the relative dynamic modulus of elasticity was calculated by

$$P_c = (E_c / E_0) \times 100$$

Equation 4.6

where,

P_c = relative dynamic modulus of elasticity, after c cycles of freezing and thawing, percent,

E_0 = dynamic Young's modulus of elasticity at 0 cycles of freezing and thawing, and

E_c = dynamic Young's modulus of elasticity at c cycles of freezing and thawing.

The equation used to calculate P_c is based on the assumption that the dimensions of the specimens remain constant during the test period. The temperature regime of the chamber is illustrated in Figure 4.1.

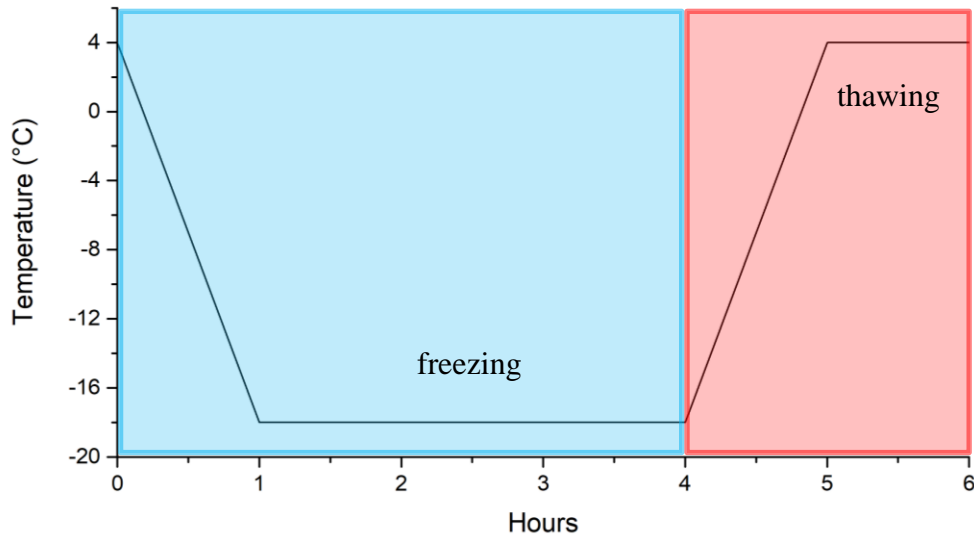


Figure 4.1 Temperature regime of one freezing-thawing cycle

4.3 Results and discussion

4.3.1 The rate of water absorption of carbonated CSC system

The initial water absorption of CSC paste at 6 hours was $12.9 \text{ mm}^3/\text{mm}^2$ and, after a day, water absorption remained constant, at approximately $15.5 \text{ mm}^3/\text{mm}^2$ over 90 days. However, as the volume of the paste in the specimen decreased, initial water absorption of CSC specimens (mortars) and total water absorption decreased dramatically. In addition, the time to reach peak water absorption took longer, which was approximately 6~7 days. This behavior indicates that the aggregate in the CSC system plays an important role in impeding water uptake, as shown in Figure 4.2, which increases the tortuosity of the pore network and decreases pore connectivity [107], [108].

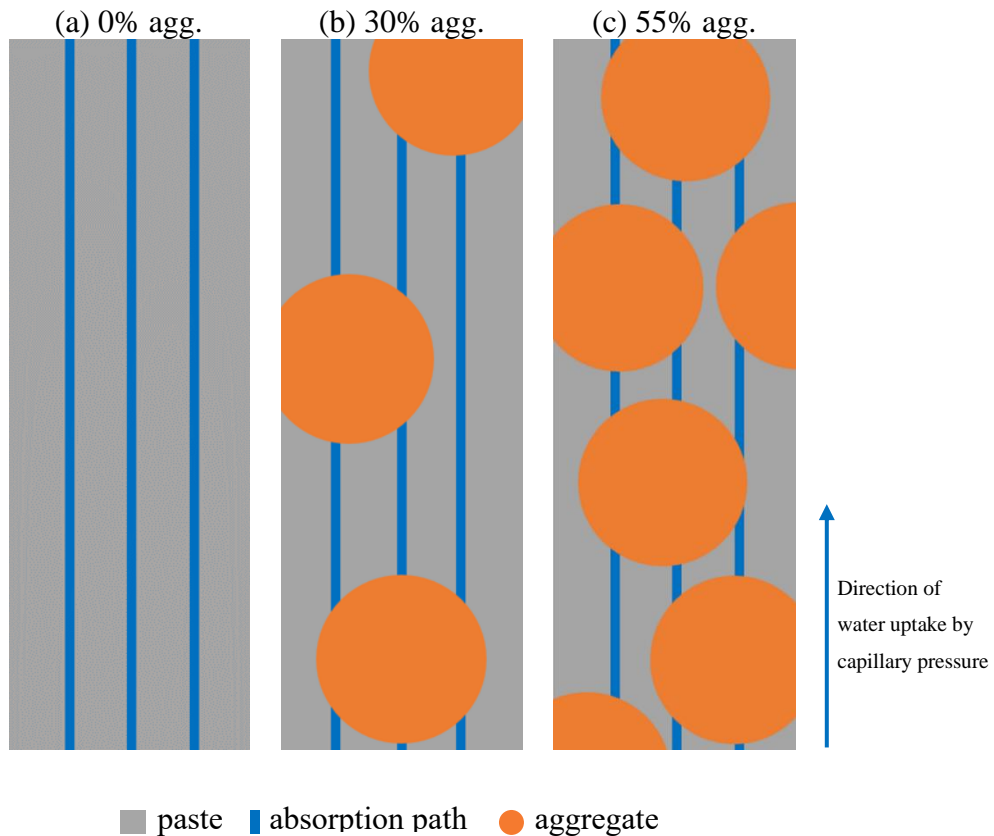
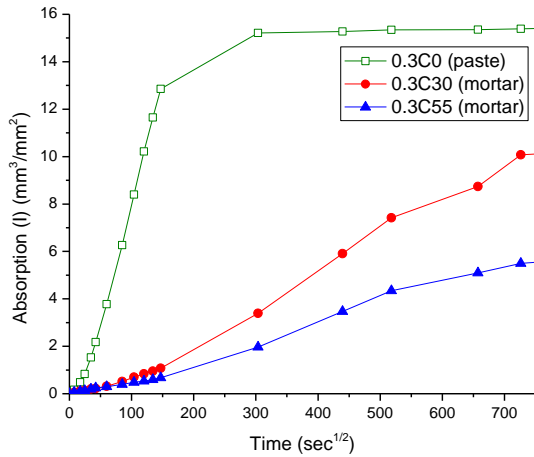
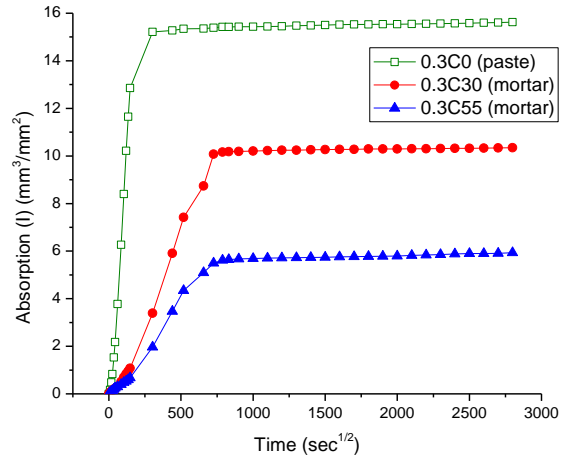


Figure 4.2 Conceptual water absorption path depending on the volume of aggregates



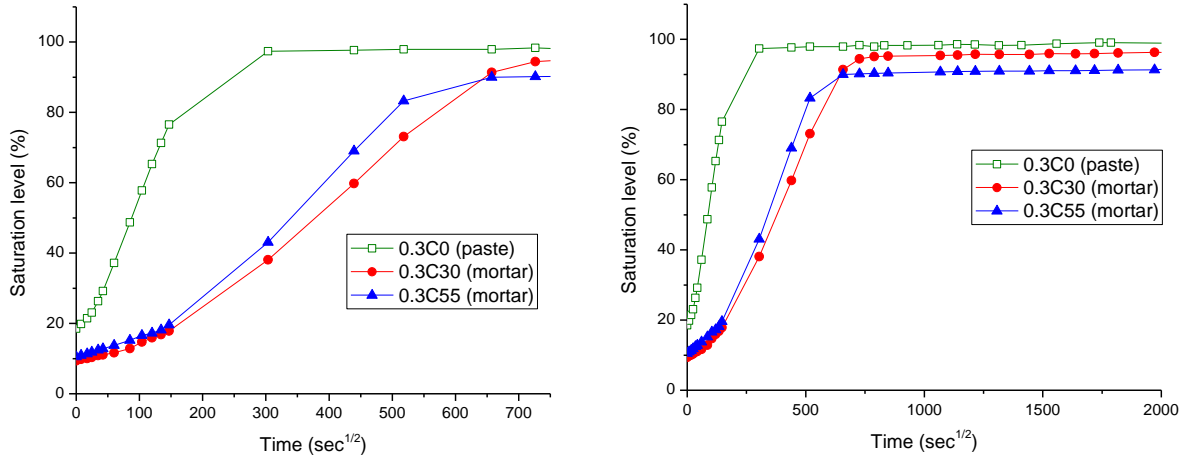
(a) absorption of CSC system for 6 days



(b) absorption of CSC system for 90 days

Figure 4.3 Water absorption of the CSC system without AEA

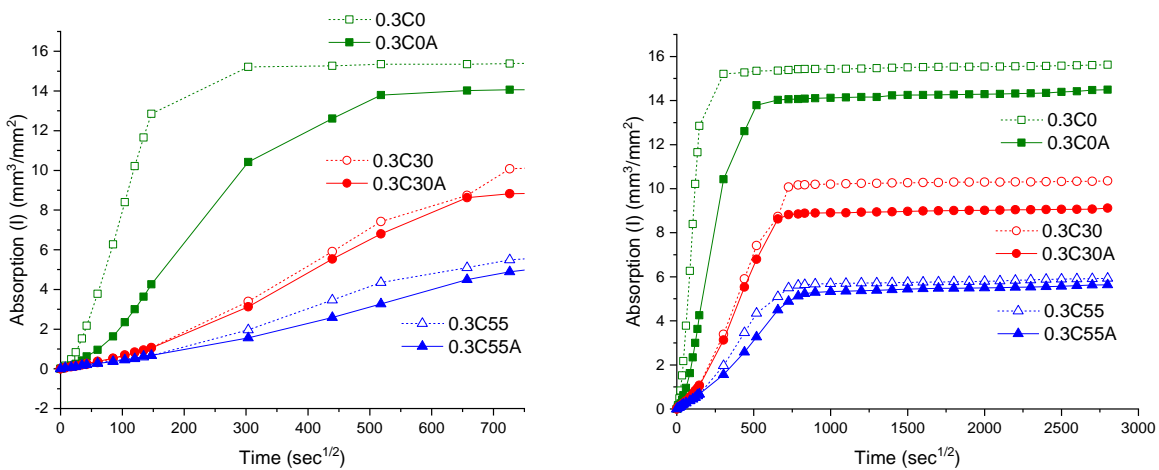
Once the specimen reached peak water absorption, the specimens did not absorb additional water. This may have been due to the fact that the specimen was completely saturated at peak water absorption; thus, it would be beneficial to plot the saturation level over time, as shown in Figure 4.4. Initially, for CSC paste, 20% of the total porosity volume was filled with water prior to initiating the absorption test because of the smaller capillary pores ($< 3\sim 4$ nm in diameter; Equation 2.13) that were saturated at 50% RH. For the other mortar specimens, approximately 10% of the total porosity volume was saturated prior to the absorption test, irrespective of the volume of aggregates. As soon as the absorption test started, the CSC paste absorbed water faster than the mortar specimen, and it reached 97% saturation in a day; while the mortar specimens reached approximately 40% saturation in a day. The rate of saturation of 0.3C30 (30% aggregates) was slightly slower than the mortar containing 55% aggregates over the first six days, but the saturation level of 0.3C30 was higher at a later age.



(a) saturation level of CSC system for 6 days (b) saturation level of CSC system for 90 days
Figure 4.4 Saturation level of CSC system without air entraining agent

4.3.2 Effect of air entraining agent (AEA) on the rate of water absorption

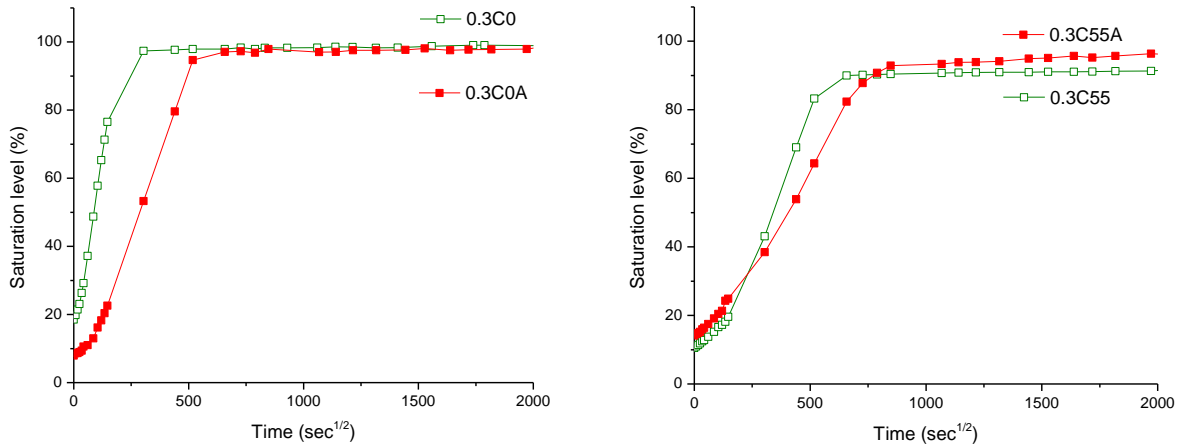
As a result of the addition of AEA to the CSC system, the total absorption of water and the initial sorptivity of the CSC specimens were decreased, as shown in Figure 4.5. The difference in these parameters between the specimens with air entrained and non-air entrained decreased as the paste content decreased. This tendency was expected, as described in Section 4.1. Also, due to the larger size of air bubbles (a few hundred microns), it was assumed that the time to reach critical saturation would be delayed. To verify this, the degree of saturation over time is discussed in the next paragraph.



(a) absorption of CSC system for 6 days (b) absorption of CSC system for 90 days
Figure 4.5 Effect of AEA on the water absorption of the CSC system (A: air entrained)

In CSC paste, entrained air reduced the initial slope of the saturation level over time until 3 days (e.g., 0.46%/sec^{1/2} for non-air entrained and 0.19%/sec^{1/2} for air entrained) and extended the time to reach critical saturation, from 1 day to 3 days. However, at a later age, both specimens had a similar level of saturation; thus, the difference was negligible.

In AE mortar specimens, the slope of the initial saturation level (0~6 hours) was lower than that of non-AE mortar specimens, but air entrainment had an insignificant impact on the time to reach critical saturation. At a later age, the AE mortar containing 55% aggregates continued to absorb water; therefore, the saturation level gradually increased. It is not clear whether the porous ITZ or the air entrained voids caused this tendency.



(a) saturation level of CSC paste

(b) saturation level of CSC mortar

Figure 4.6 Effect of air entraining agent on saturation level

4.3.3 Comparisons of the rate of water absorption with OPC system

The total amount of water absorption by the CSC system was significantly higher than that of the OPC system, regardless of the water-to-cement ratio of in OPC system; although there is a slight difference in the total porosity of the specimens with the same water-to-cement ratio. This is because the water absorption test is highly dependent on the pore characteristics of unsaturated specimens: pore connectivity, tortuosity, and the volume of capillary pores, as mentioned in Section 4.1. In the case of the OPC system, the ratio of the volume of capillary pores to the volume of gel pores increases as the water content (or w/c) in the OPC system increases. Thus, with a lower water-to-cement ratio, the OPC system contains a higher volume of gel pores and a lower volume of capillary pores. For example, according to Powers and Hansen [43]–[45], 6.6%

and 22% of the total volume of 0.3 w/c OPC paste consists of capillary pores and gel pores, respectively, at a 72% degree of hydration. This implies that 22% of the total volume of the OPC paste is already saturated before the water absorption test and only 6.6% pores are empty. In other words, 77% of the total porosity in 0.3 w/c of OPC is already saturated before the test and 23% of total porosity remains as an empty space that can absorb water. However, in CSC paste, the majority of pores were capillaries (80~90% of total porosity, as shown in Figure 4.9) so that the total water absorption was higher than the OPC system during the test; even though the total porosities of 0.42 and 0.6 of the OPC system were higher than the 0.3 of the CSC system. Thus, the initial sorptivity of CSC system was higher but the secondary sorptivity was not much different from OPC. This tendency also occurred in the OPC system; as the water-to-cement ratio increased, total water absorption and the initial sorptivity increased due to the higher volume of capillary pores. In both types of specimens, total water absorption and the initial sorptivity decreased as the paste content of the specimens decreased.

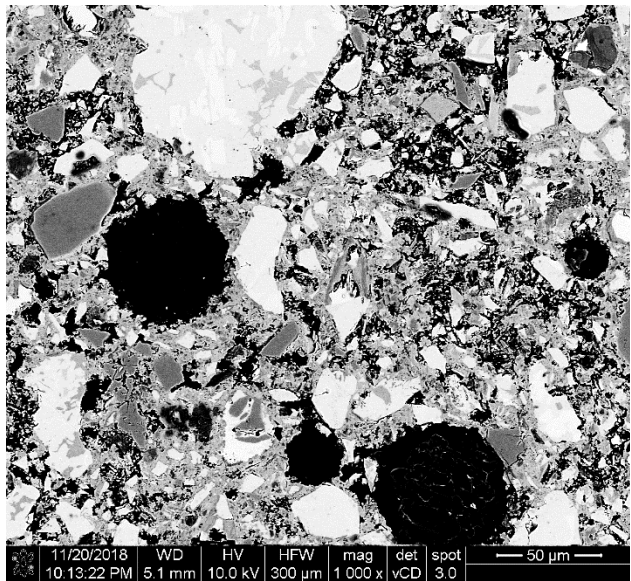
In terms of the saturation level of the specimens, all non-AE paste specimens except 0.3 OPC exceeded 90% saturation. The peak level of saturation of the specimens declined as the volume of aggregates in the specimens increased. Also, the peak level of saturation was reduced by air entrainment. Furthermore, entrained air decreased the initial sorptivity and delayed the time to reach the peak level of saturation. In the case of OPC mortars, entrained air maintained the degree of saturation below 85%; however, in the 0.6 w/c OPC paste specimen, the effect of AEA was insignificant because of the lack of shearing force during mixing of the raw particles, which creates larger sized air voids (lower specific surface area of the air voids) [109]–[111]. Also, as the water-to-cement ratio of the OPC system increased, changes in the degree of saturation consistently increased during the test period because of the high volume of capillary pores. Thus, using AEA is beneficial if the specimen contains a higher volume of capillary pores; in the AE OPC mortars that contained 55% aggregates, the peak level of saturation was similar regardless of the water-to-cement ratio.

On the other hand, air entrainment was not much effective on the peak saturation level of the CSC system as compared to that of the OPC system, although total water absorption by the AE CSC system was reduced as compared to the non-AE CSC system. For example, without AE, both types of mortars that contained 55% aggregates had a similar level of saturation but in both cases, when AEA was used, only peak saturation of the OPC specimens was affected; the values

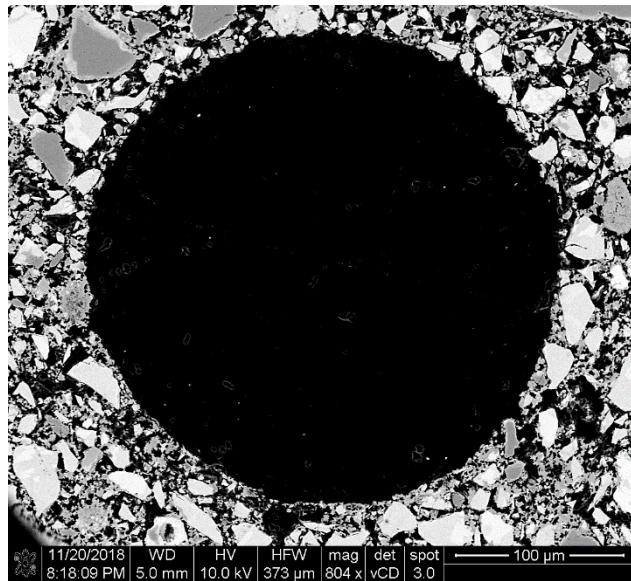
of OPC mortars decreased to 80%. Moreover, in the CSC system, the peak level of saturation was greater than 90% that was reached faster as compared to the OPC system. In general, greater than 88~92% saturation is critical to the freeze-thaw performance of the OPC system [28], [70]. The ineffectiveness of AEA in the CSC system may have been caused by the imperfect circular shapes and porous boundary of the entrained air (Figure 4.7) and the stabilization of air bubble during the special carbonation curing process: high temperature and loss of water and a somewhat inconsistent degree of carbonation throughout the specimens. In addition, the air voids in the CSC system may be connected to more capillary pores (water path) [112], [113]. Although the entrained air voids system of CSC was not explored in this study, studying this may result in improvements to the quality of the CSC system, especially under freeze-thaw conditions. Although AEA does not seem to be useful regarding peak level of saturation, it did help to reduce initial sorptivity. This tendency may still be useful for improving the performance of the CSC system under freeze-thaw conditions. Therefore, the next section discusses the effect of AEA on freeze-thaw resistance of the CSC system.

Table 4.2 Initial and secondary sorptivity of the CSC and OPC specimens (mm/sec^{1/2})

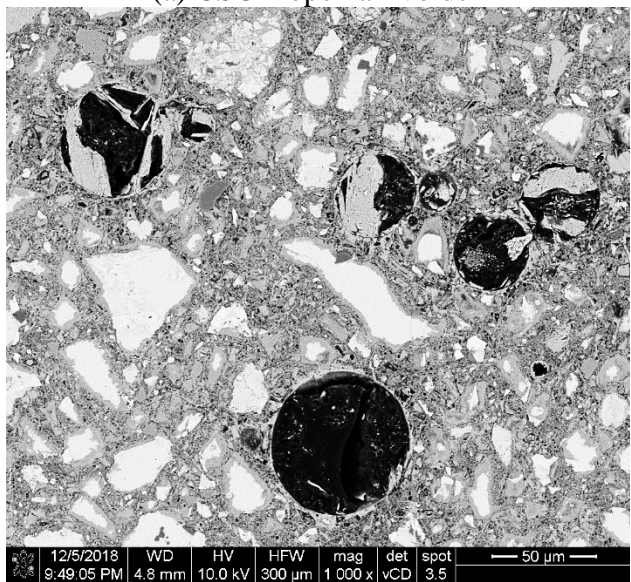
Non-AE			AEA		
specimen	initial sorptivity	secondary sorptivity	specimen	initial sorptivity	secondary sorptivity
0.3C0	0.09240	0.00010	0.3C0A	0.03140	0.00020
0.3C30	0.01430	0.00009	0.3C30A	0.01350	0.00001
0.3C55	0.00820	0.00010	0.3C55A	0.00680	0.00020
0.3P0	0.00540	0.00060	0.3P0A	0.00390	0.00040
0.3P30	0.00080	0.00030	0.3P30A	0.00070	0.00020
0.3P55	0.00150	0.00020	0.3P55A	0.00090	0.00020
0.42P0	0.00700	0.00070	0.42P0A	0.00580	0.00030
0.42P30	0.00400	0.00040	0.42P30A	0.00390	0.00020
0.42P55	0.00340	0.00030	0.42P55A	0.00210	0.00030
0.6P0	0.02150	0.00002	0.6P0A	0.01860	0.00002
0.6P30	0.01220	0.00003	0.6P30A	0.00670	0.00030
0.6P55	0.00570	0.00010	0.6P55A	0.00410	0.00030



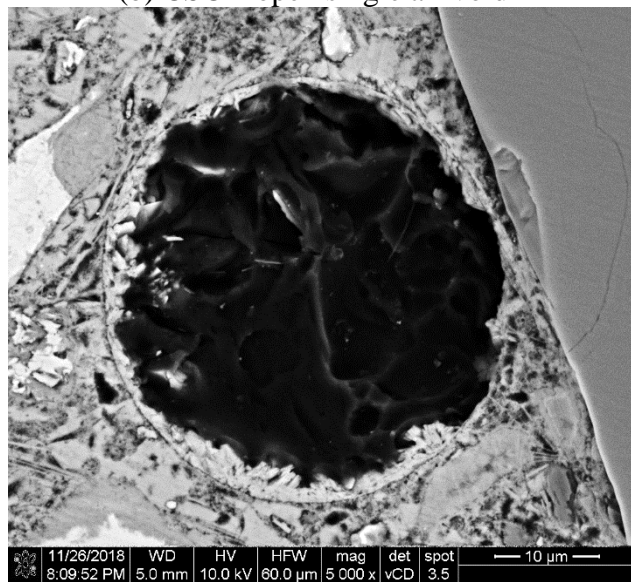
(a) CSC – open air voids



(b) CSC – open single air void

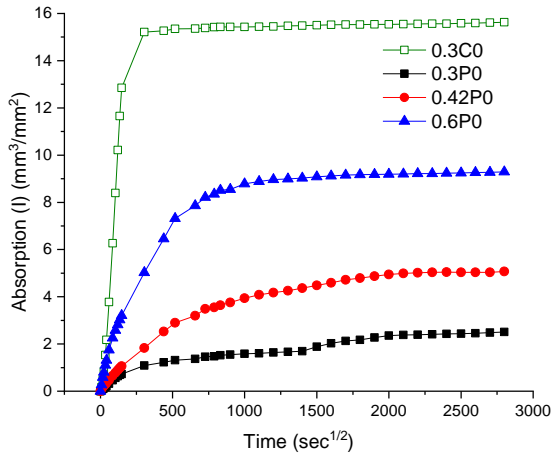


(c) OPC – closed air voids

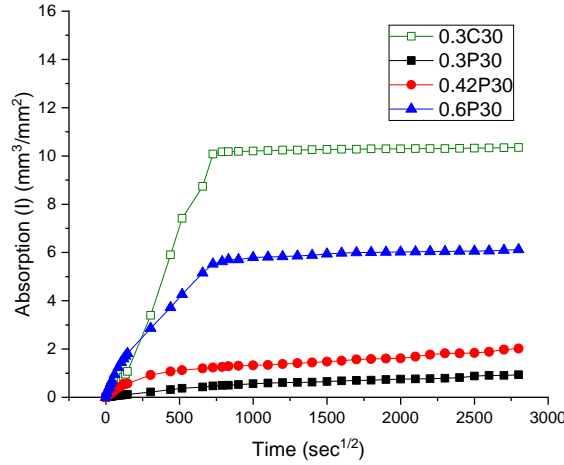


(d) – closed single air void

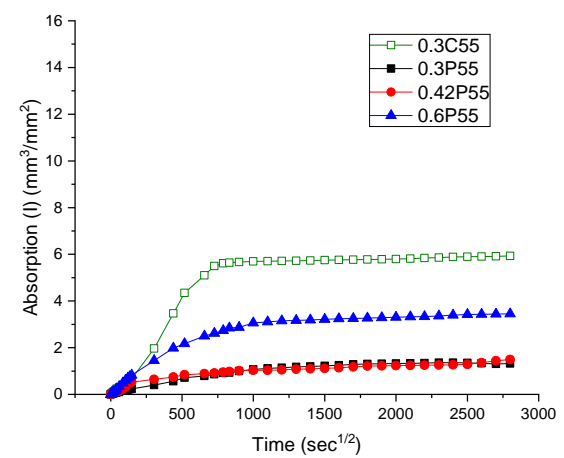
Figure 4.7 Comparison of the characteristic of air voids in CSC and OPC



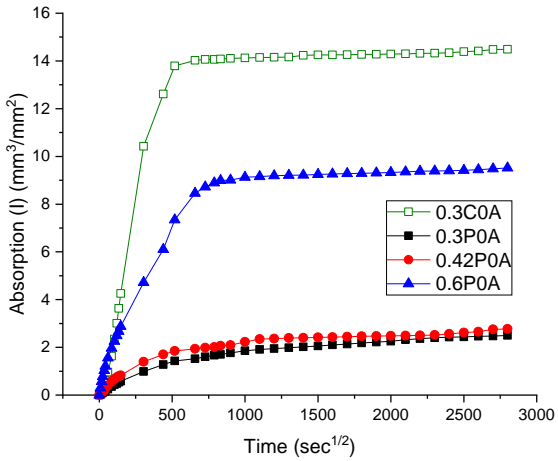
(a) Non-AE pastes



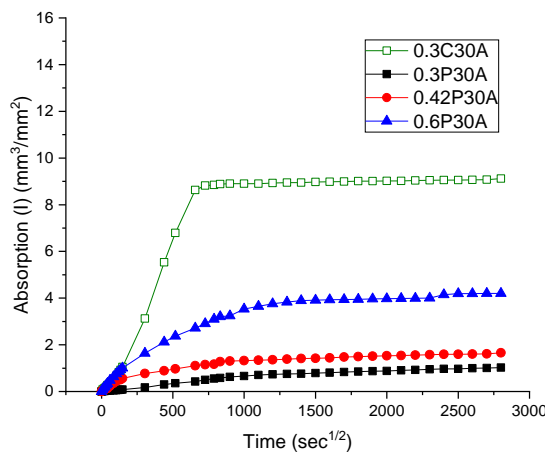
(b) Non-AE mortars containing 30% agg.



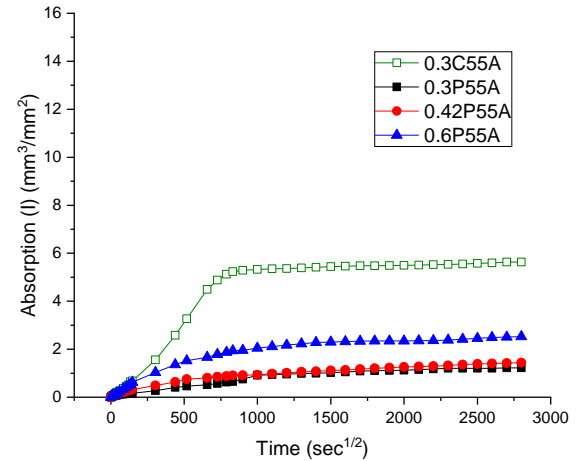
(c) Non-AE mortars containing 55% agg.



(d) AE pastes

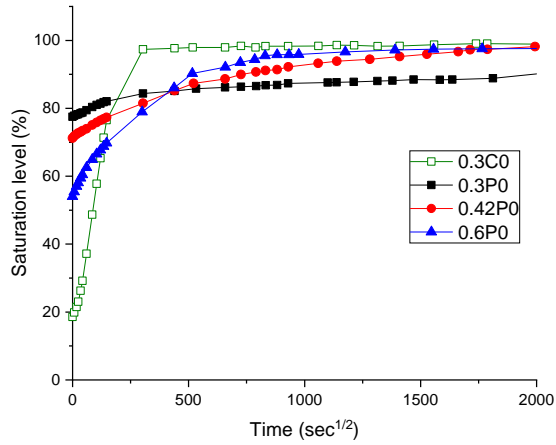


(e) AE mortars containing 30% agg.

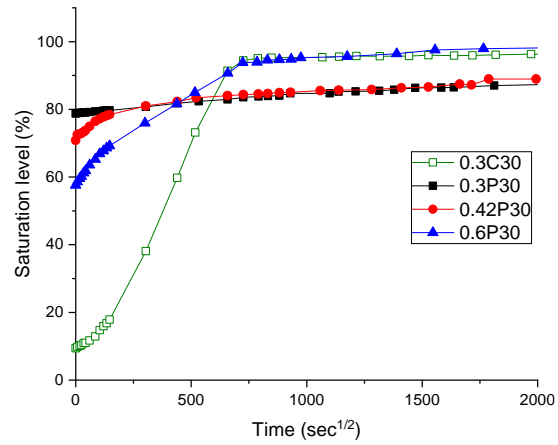


(f) AE mortars containing 55% agg.

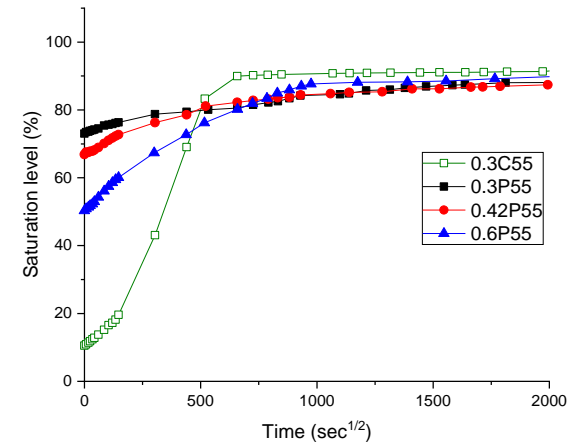
Figure 4.8 Rate of water absorption (sorptivity) results for the paste and mortar specimens



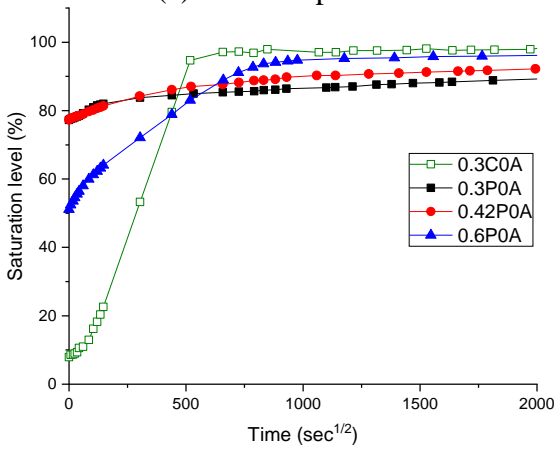
(a) Non-AE pastes



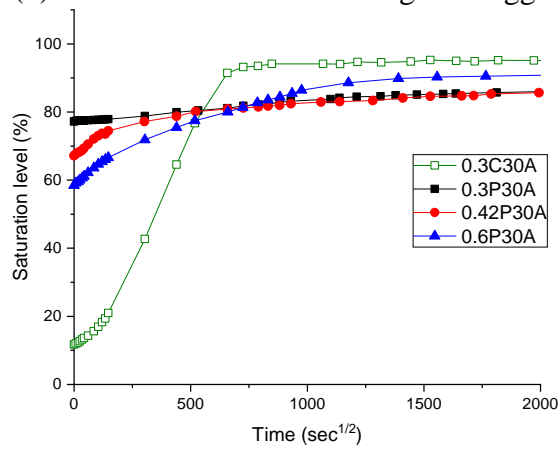
(b) Non-AE mortars containing 30% agg.



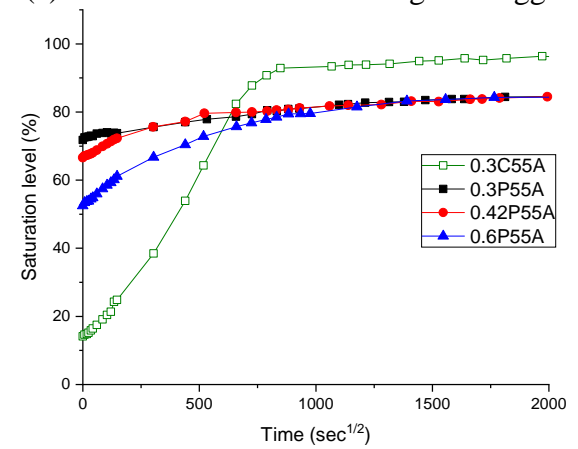
(c) Non-AE mortars containing 55% agg.



(d) AE pastes



(e) AE mortars containing 30% agg.

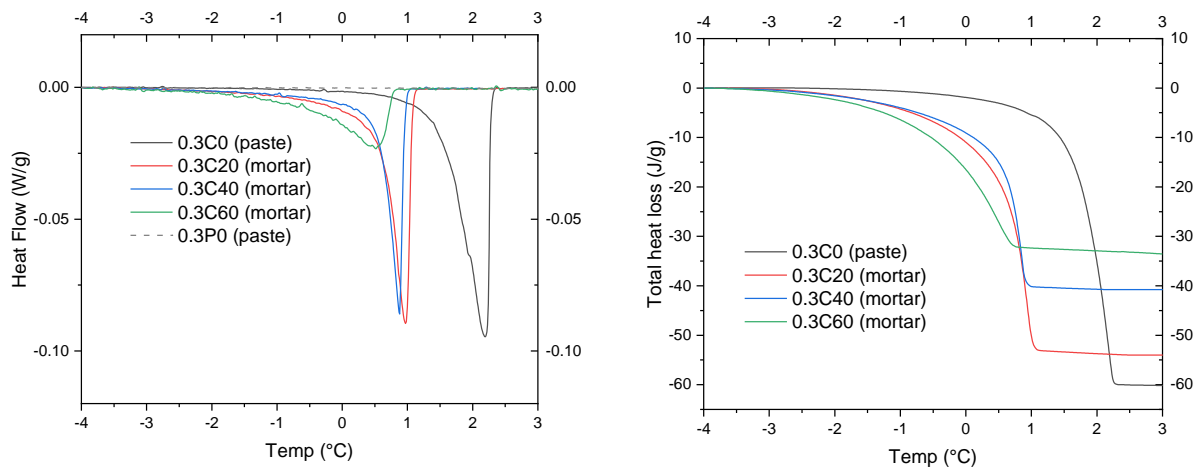


(f) AE mortars containing 55% agg.

Figure 4.9 Degree of saturation of the paste and mortar specimens

4.4 The amount of freezable water in the carbonated CSC system

For this experiment, CSC specimens were tested with 20% increments of aggregates in a volume up to 60%. Total heat loss was calculated based on the area of the heat flow over time. The total amount of freezable water was calculated based on the total heat loss divided by 334 J/g (heat of fusion of water). The amount of freezable water in the CSC system decreased as the volume of aggregates (ASTM C778 sand) increased, with a linear relationship as shown in Figure 4.11. The melting point of water in the CSC specimens was slightly depressed as the volume of the aggregates increased.



(a) heat flow of CSC system

(b) total heat loss of CSC system

Figure 4.10 DSC results of melting ice in the CSC system

Table 4.3 Total amount of freezable water in the CSC system

	Paste content	Total heat loss (J/g of sample)	amount of freezable water (g of water/g of sample)
0.3C0	100%	60.1	0.1799
0.3C20	80%	53.2	0.1593
0.3C40	60%	40.4	0.1210
0.3C60	40%	32.8	0.0982

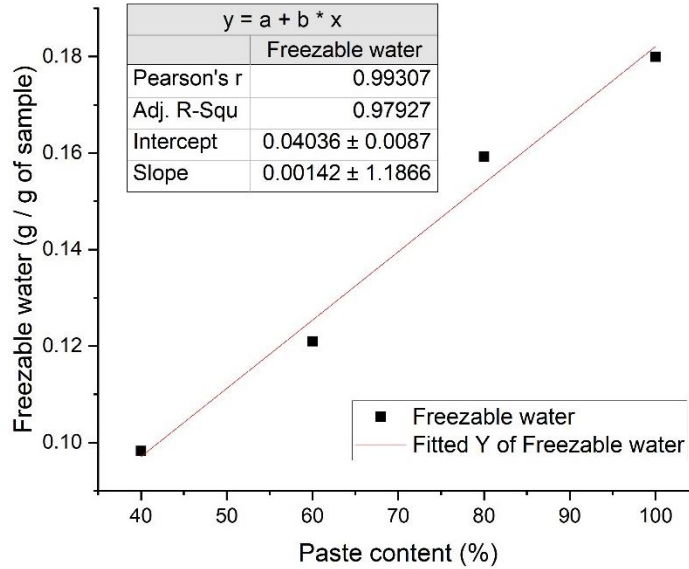


Figure 4.11 Relationship between the amount of freezable water and the CSC paste content

4.5 Freeze-thaw resistance of air entrained CSC system

Prior to discussing freeze-thaw resistance of the CSC system, it should be noted that the exposure conditions of this experiment were somewhat harsh on the specimens because of the small size (2" × 1" × 6") of paste and mortar specimens; ASTM C666 is designed for 3" × 4" × 16" concrete specimens. Also, the dynamic modulus of elasticity is more sensitive to changes in resonant frequency and the mass of the smaller sized specimens. As a result, the degree of degradation of the dynamic modulus of elasticity of the small specimens may be higher than if 3" × 4" × 16" concrete specimens had been tested. Also, 60% of the relative dynamic modulus of elasticity, which is the failure point determined by ASTM C666, may not be applicable to the small paste and mortar specimens in this study.

First, without entrained air, all of the CSC specimens failed suddenly at the early stage of the experiment. CSC paste was completely broken at only 4 F/T cycles, as shown in Figure 4.15. The other specimens failed at 36 F/T cycles, although the surfaces of the specimens were not damaged as much based on the relative dynamic modulus. Cracks and erosion started at the edge of the specimens. Therefore, the impact of freezing-thawing on CSC paste and mortars without entrained air was detrimental.

AEA was used in the CSC system and is commonly used in OPC concrete for improving freeze-thaw resistance. A significant improvement was observed in the CSC specimens as shown in Figure 4.12 (b) and Figure 4.15. In CSC paste, the specimen survived after 4 F/T cycles,

which did not occur without entrained air and there were no severe cracks. However, with a larger number of F/T cycles, CSC paste started losing its mass from the edges and surfaces and, eventually, resonant frequency measurements were unreliable after 156 F/T cycles. During the test, several cracks developed, which were in horizontal direction to the side of the paste specimen. In the CSC mortar specimens, mass loss was not as significant as compared to the CSC paste. The CSC mortars rather lost smaller amount slowly from the edges and surface. After a few F/T cycles, the surfaces of aggregates were exposed due to surface scaling. Continual mass loss occurred as F/T cycles progressed until the end of the test. In the CSC mortar containing 55% aggregate, the degradation process that occurred under F/T conditions was faster than what occurred for the CSC mortar containing 30% aggregate and there was more mass loss. At the end of the test, the thickness of the specimen containing 55% aggregate was thinner than the original due to F/T damage. In general, the RDME was moderately decreased when the air was entrained in the CSC specimens instead of the sudden drop of RDME that was seen for the non-air entrained CSC specimens. Thus, adding AEA into the CSC system appears to be mandatory in order to improve performance under F/T conditions.

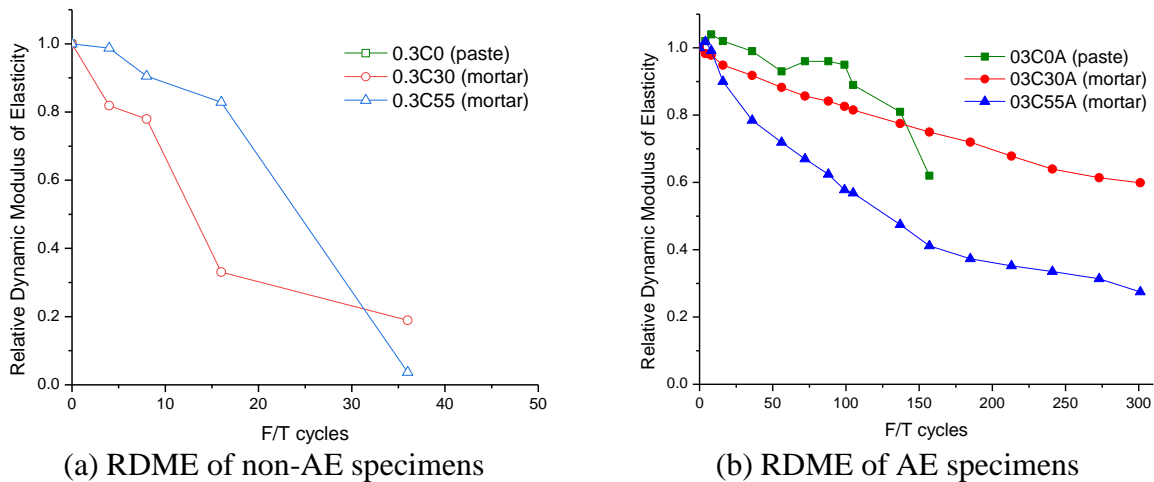
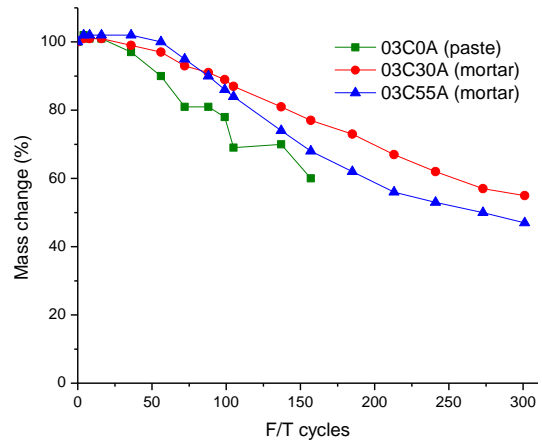
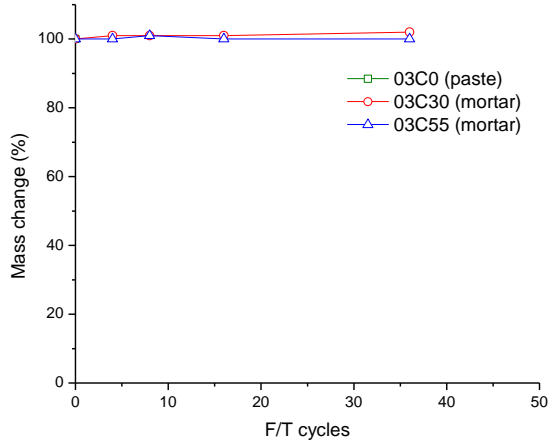


Figure 4.12 Relative dynamic modulus of elasticity (RDME) of CSC specimens under F/T cycles



(a) mass change of non-AE specimens

(b) mass change of AE specimens

Figure 4.13 Mass change of CSC specimens under F/T cycles



(a) non-AE CSC paste at 4 F/T cycles



(b) AE CSC paste at 160 F/T cycles



(c) non-AE CSC mortar-55% agg. at 36cycles



(d) AE CSC mortar-55% agg. at 300 F/T cycles

Figure 4.14 Close view of CSC specimens at the failures

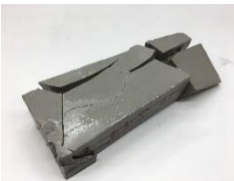
# of cycles	Non-AE specimens			AE specimens		
	pastes	mortars (30% agg.)	Mortars (55% agg.)	pastes	mortars (30% agg.)	mortars (55% agg.)
0						
4						
36	N/A					
156	N/A	N/A	N/A			
300	N/A	N/A	N/A	N/A		

Figure 4.15 Overview: the appearances of the CSC specimens exposed to F/T cycles

4.6 Conclusion

The initial rates of water absorption (sorptivity) of the CSC system were the highest among all OPC specimens. This was mainly because the pore system of the CSC specimens had a higher volume of air-filled capillary pores as compared to OPC specimens, prior to the water absorption test. This tendency was also found in the OPC series; the initial sorptivity increased as the water-to-cement ratio increased due to the higher ratio of the volume of capillary pores to the volume of gel pores. Another reason was the high pore connectivity of CSC system as compared to the OPC system, as shown in the MIP results in Chapter 3. Also, as the aggregate content increased, the initial sorptivity of the specimen decreased as well as peak water absorption because the aggregates played a significant role in reducing pore connectivity and the total porosity of the CSC system.

The results of the water absorption test were used to determine the degree of saturation of the CSC specimens. In the non-AE CSC paste, the time to reach peak saturation was 2 days and the peak level was almost 100%, which is critical for freeze-thaw performance. This tendency was diminished when the CSC system was combined with the aggregates, which lowered peak saturation to below 95%. However, this saturation level was still detrimental to the CSC specimens that were exposed to freeze-thaw conditions. As a consequence of these pore characteristics of the CSC system, the non-AE CSC specimens failed suddenly with a few F/T cycles; especially, the paste specimens were completely broken after 4 F/T cycles. Therefore, using an air entraining agent is recommended for the CSC system in order to lower the peak level of saturation and the initial sorptivity.

In this study, entrained air helped to slow down the initial sorptivity of the CSC system and delayed the time required to reach the peak level of saturation. However, the peak level of saturation was still greater than the critical saturation level and as a result the air entrained CSC system may still be susceptible to the actions of freezing-thawing. Entrained air significantly improved the freeze-thaw resistance of the CSC system. There was no sudden failure and the degradation progressed gently. The AE paste specimen failed earlier than the AE mortar specimens. The mortar containing 55% aggregates was expected to perform the best among the tested CSC specimens because of its lowest initial sorptivity and peak level of saturation but the mortar containing 30% aggregate performed the best under freeze-thaw conditions. This may be

because of the wall and percolation effects (increased area of porous ITZ) in the mortar containing 55% aggregates, as described in Chapter 3.

Therefore, to improve the freeze-thaw resistance of the CSC system, the pore characteristics of the CSC system need to be modified by the following strategies: reducing total water absorption, the connectivity of the pore network, increment in the tortuosity of pore network, and delay in the time to reach critical saturation. These desired properties of the pore characteristics of the CSC system can be enhanced by increasing the volume and size of the aggregates and using AEA. Additionally, increased the tortuosity of the pore network by using large (less surface area) or angular shaped aggregates will help to diminish the porous ITZ that was present in the CSC containing 55% aggregates (round shape of sand particles) or will help to increase the bonding between aggregates and CSC paste.

Since the unique pore characteristic of CSC after carbonation contains a higher volume of capillary pores than gel pores (approximately 4 to 1), the pore network needs to be alternated by using an air entraining agent. AEA plays a significant role in delaying the time to reach the critical saturation level and reducing total water absorption. Moreover, due to its spherical shape of large air bubbles, the entrained air reduces the internal tensile stress caused by ice formation.

Based on an understanding these design parameters, the CSC concrete containing angular shaped aggregates and entrained air needs to be studied in terms of whether its freeze-thaw resistance is improved or not, which is done in the next chapter.

5. FREEZING-THAWING AND SCALING RESISTANCES OF CARBONATED CSC CONCRETE

5.1 Motivations and objectives

In this chapter, the freeze-thaw resistance of CSC concretes (CSCC) is discussed. Based on the findings from the previous chapter (i.e., AEA and angular shape of aggregates), various CSCC were designed and their resistance to freeze-thaw was compared. The CSCC included non-AE and AE CSC concretes containing crushed granite and AE CSC concrete containing pea gravel. Since CSCC is the concrete based on new cementitious material, it was beneficial to compare freeze-thaw performance with conventional concrete (reference concrete). OPC replaced with 20% fly ash concrete was selected as a reference, since it is well-known for its excellent freeze-thaw performance. For these tests, ASTM C457 [114], ASTM C642 [115], ASTM C666 [104], and ASTM C672 [116] were performed because use of these standards demonstrate the criteria necessary for evaluating freeze-thaw performance of concretes.

5.2 Materials and methods

Three different cementitious materials were used: ASTM C150 Type I OPC, ASTM C618 Type C fly ash, and CSC. The chemical composition of each cementitious material is listed in Table 5.2. Natural sand was used as a fine aggregate and three different types of aggregates were used as coarse aggregates: crushed limestone, crushed granite, and pea gravel. Crushed granite and pea gravel were used only in CSC concretes and the crushed limestone was used in the reference concrete. The reason for using two different crushed coarse aggregates in two different types of concrete was that the crushed granite was more easily accessible in NJ, as the CSC concrete was manufactured and shipped from Solidia Technologies located in Piscataway, NJ. The properties of the aggregates are listed in Table 5.1.

Table 5.1 Properties of aggregates

	Specific Gravity	Absorption	Max. size
Crushed limestone	2.72	1.2%	1"
Crushed granite	3.03	0.4%	1/2"
Rounded pea gravel	2.62	1.7%	3/8"
Natural sand	2.56	2.1%	1/5"

Table 5.2 Chemical components of cementitious materials

	Content (%)		
	Type I OPC	Fly ash Class C	CSC
SiO ₂	19.6	36.9	44.02
Al ₂ O ₃	5.2	20.14	5.13
Fe ₂ O ₃	2.9	7.01	1.79
CaO	64.0	24.6	43.64
MgO	2.6	5.47	1.15
SO ₃	3.3	1.58	0.16
Total alkali (Na ₂ O+0.658 K ₂ O)	0.72	1.21	1.61
L.O.I.	1.2	-	0.71
Total	99.52	96.91	98.21

5.2.1 Mixture proportions

Proportions of mixtures were carefully designed so that a reasonable comparison of freeze-thaw resistance between both types of concretes could be made. In general, the OPC concrete specimens used for the comparison of freeze-thaw resistance would have the same water-to-cement ratio (w/c) because w/c plays a critical role in the porosity of the concrete; as w/c increases, the specimen is more susceptible to freeze-thaw conditions. However, as discussed in

Chapter 3, the 0.3 OPC system showed excellent freeze-thaw resistance regardless of whether AEA was used because the primary volume of the pores in 0.3 OPC consists of gel pores; the gel water is hardly frozen above -40°C (due to pore size) and the high ionic strength of the pore solution depresses the freezing temperature of water in gel pores even further. On the other hand, the 0.3 CSC system contains a higher volume of capillary pores that are vulnerable to freezing and thawing. Thus, instead of having the same w/c for the comparison of freeze-thaw resistance, concretes with a similar compressive strength were selected for this study. All mixtures in Table 5.3 has repeatedly gained 7,000 ~ 8,000 psi level of compressive strength.

For both types of concretes, air entraining agent was used to improve freeze-thaw resistance, and 20% OPC (Type I cement) was replaced by Class C fly ash to reduce permeability in the presence of de-icing solution [5], [117]. However, the carbon content in fly ash may have obstructed the surfactant action of AEA and this may have resulted in an insufficient entrained air volume [118], [119]. Furthermore, to make additional comparisons, non-air entrained (NAE) CSCC containing crushed granite and air entrained (AE) CSCC containing pea gravel were prepared for the reasons mentioned in Section 5.1.

Table 5.3 Concrete Mixture Proportions

	AE CSCC (crushed granite)	AE CSCC (pea gravel)	AE Reference concrete	NAE CSCC
Cement, lb/yd ³	-	-	547	-
Solidia cement, lb/yd ³	674	674	-	674
Fly ash, lb/yd ³	-	-	137	-
Water, lb/yd ³	196	196	287	196
Sand, lb/yd ³	1,161	1,161	1,290	1,161
Coarse aggregate, lb/yd ³	1,911	1,652	1,740	1,911
AEA, fl.oz/cwt	1.0	1.0	1.02	-
Water reducer, fl.oz/cwt	2.4	2.4	-	2.4
w/cm	0.30	0.30	0.42	0.30

Table 5.4 Test matrix and the number of specimens

Type of specimen	Scaling resistance ASTM C672	Freeze-thaw resistance ASTM C666	Air void spacing ASTM C457	Permeable voids ASTM C642
AE CSCC (crushed agg.)	2	3	3	3
AE CSCC (pea gravel)	-	3	-	-
AE reference (crushed agg.)	2	3	3	3
NAE CSCC (crushed agg.)	-	3	-	-

5.2.2 Resistance to surface scaling

According to the ASTM C 672 standard, the specimens $72 \text{ in}^2 \times 3 \text{ in}$ (h) were placed in a moist curing room for 28 days after demolding and were stored in a 50% relative humidity chamber at $(23 \pm 2) \text{ }^\circ\text{C}$. After building a dike to retain the 4% CaCl_2 solution on the top surface of the specimens, they were placed in an environmental chamber. The temperature of the chamber was set to $(-18 \pm 3) \text{ }^\circ\text{C}$ for 11 hours and to $(23 \pm 2) \text{ }^\circ\text{C}$ for 11 hours. The 4% CaCl_2 solution was prepared by diluting 100 g of 40.8% CaCl_2 solution with 920 g of water and the solution was repeatedly replenished after the completion of every 5 freezing-thawing cycles. The measurement of the mass loss was monitored until 100 F/T cycles.

5.2.3 Freezing-thawing (F/T) test of concrete specimens - ASTM C666

The concrete specimens were cast in molds ($3'' \times 4'' \times 16''$) and were demolded one day after. Prior to the freezing-thawing test, reference concretes were stored in a saturated lime water bath (23°C) for 14 days and CSC concretes were cured in a carbonation chamber (65°C , 60~65% RH, and high purity CO_2 at a pressure of 1 atm) for another 6 days at Solidia Technologies. As soon as the CSC specimens arrived at Purdue, they were placed in a lime saturated water bath for 14 days. Before the test, the specimens were placed in a water container at 4°C for 1~2 hours and then the masses and resonant frequencies of the specimens were measured.

Immediately after these measurements, the specimens were exposed to repeated freezing-thawing cycles, as shown in Figure 4.1. At least every 28 F/T cycles, mass and resonant frequency of the specimen were recorded. During the measurements, the specimen container was cleaned and replenished with cold tap water.

5.2.4 SEM analysis

At the completion of the freezing-thawing test, SEM samples were collected from the degraded specimens, as shown in Figure 5.1. This analysis was designed to investigate microstructures at the corner and inside of the damaged specimens by freezing-thawing action and to examine the formation of the micro-cracks in its system. A dry-cut saw was used to obtain SEM samples ($\leq 1 \times 1 \times 1 \text{ in}^3$) from the specimens, and the samples were placed in a convection

oven at 60°C for three days. Once dried, the SEM samples were thoroughly vacuum impregnated with a low-viscosity epoxy. The impregnated specimens were lapped and polished with progressively smaller grit (45 μm, 30 μm, 15 μm, 9 μm, 6 μm, 3 μm, 1 μm, and 1/4 μm). After polishing, palladium sputter-coated was applied on the top surface of the sample to reduce thermal damage and to prohibit the accumulation of electrostatic charges.

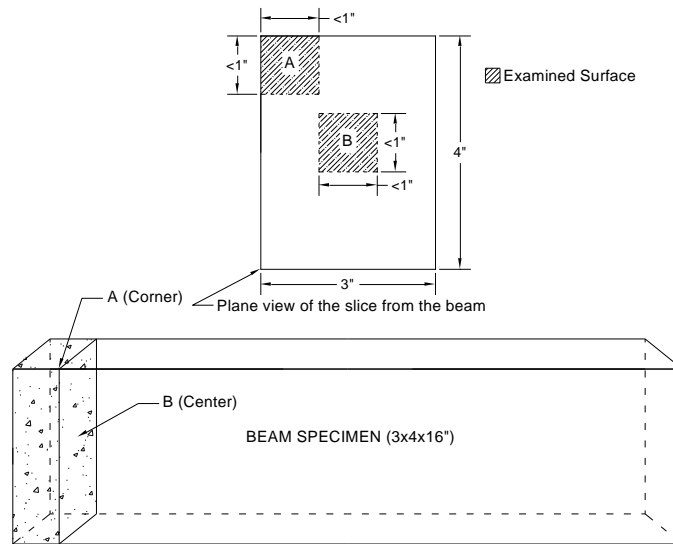


Figure 5.1 Locations of SEM samples

5.2.5 Air void spacing factor in hardened concrete

It is essential to understand the air void system in hardened concrete in order to explain and evaluate the resistance to freezing-thawing of the specimens. Based on ASTM C457, with the use of 1 in maximum size of aggregate, the minimum area of the polished surface for microscopical measurement should be 12 in². Thus, the surface area (13 in²) of the concrete specimens was examined in order to calculate an air void spacing factor in hardened concrete and the linear traverse method (procedure A) was applied. For magnification of the optical microscope, 60X was used.

5.2.6 The volume of voids in hardened concrete

Based on ASTM C642, three disks (4”(d)×2”(t)) were prepared in order to calculate the average value of permeable voids in hardened concrete. This test was performed before exposure to freezing-thawing.

5.3 Results and discussion

5.3.1 Resistance to surface scaling

As shown in Figure 5.3, no visible signs of scaling were found on either specimen (AE reference concrete and AE CSCC). Also, both specimens increased in mass during the scaling test, as shown in Figure 5.2. AE CSCC absorbed a higher amount of 4% CaCl_2 solution as compared to the AE reference because of the high volume of capillary pores in the CSC system. The discoloration of the specimens was due to the color of the CaCl_2 solution. In general, scaling damage increased as the w/cm increased, because there are more of the larger capillary pores that can accommodate a large amount of water near the finishing surface. Also, in the OPC system, calcium oxychloride can be formed due to the reaction between calcium hydroxide and CaCl_2 ; which is detrimental to the OPC system. On the other hand, in the CSC system, there is no calcium hydroxide, so calcium oxychloride cannot be formed in the presence of CaCl_2 [120]. For these reasons, it is expected that scaling damage from the AE reference concrete (0.42 w/cm) would be higher than the AE CSCC (0.3 w/c). However, the reference concrete in this experiment performed well because Class C fly ash refines the pore structure of the OPC system and reduces the amount of calcium hydroxides, which helps to resist damage from scaling [121], [122]. According to ACI 318, an unreinforced concrete structure should have a maximum of 0.45 w/cm and 4,500 psi compressive strength in the presence of deicing chemicals in order to increase the resistance to scaling [123]. Thus, both types of air-entrained specimens resulted in outstanding resistance to scaling until 100 freezing-thawing cycles in the presence of 4% CaCl_2 .

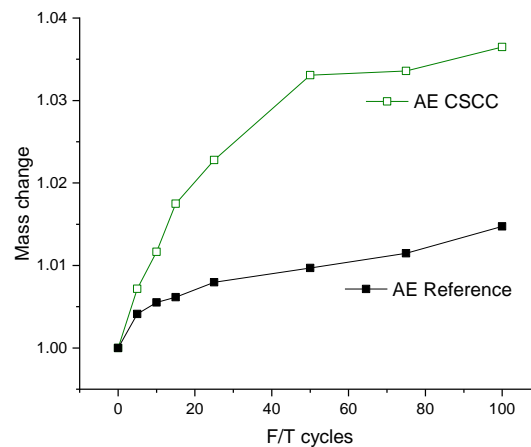


Figure 5.2 Mass changes of AE CSCC and AE Reference concrete (scaling test)

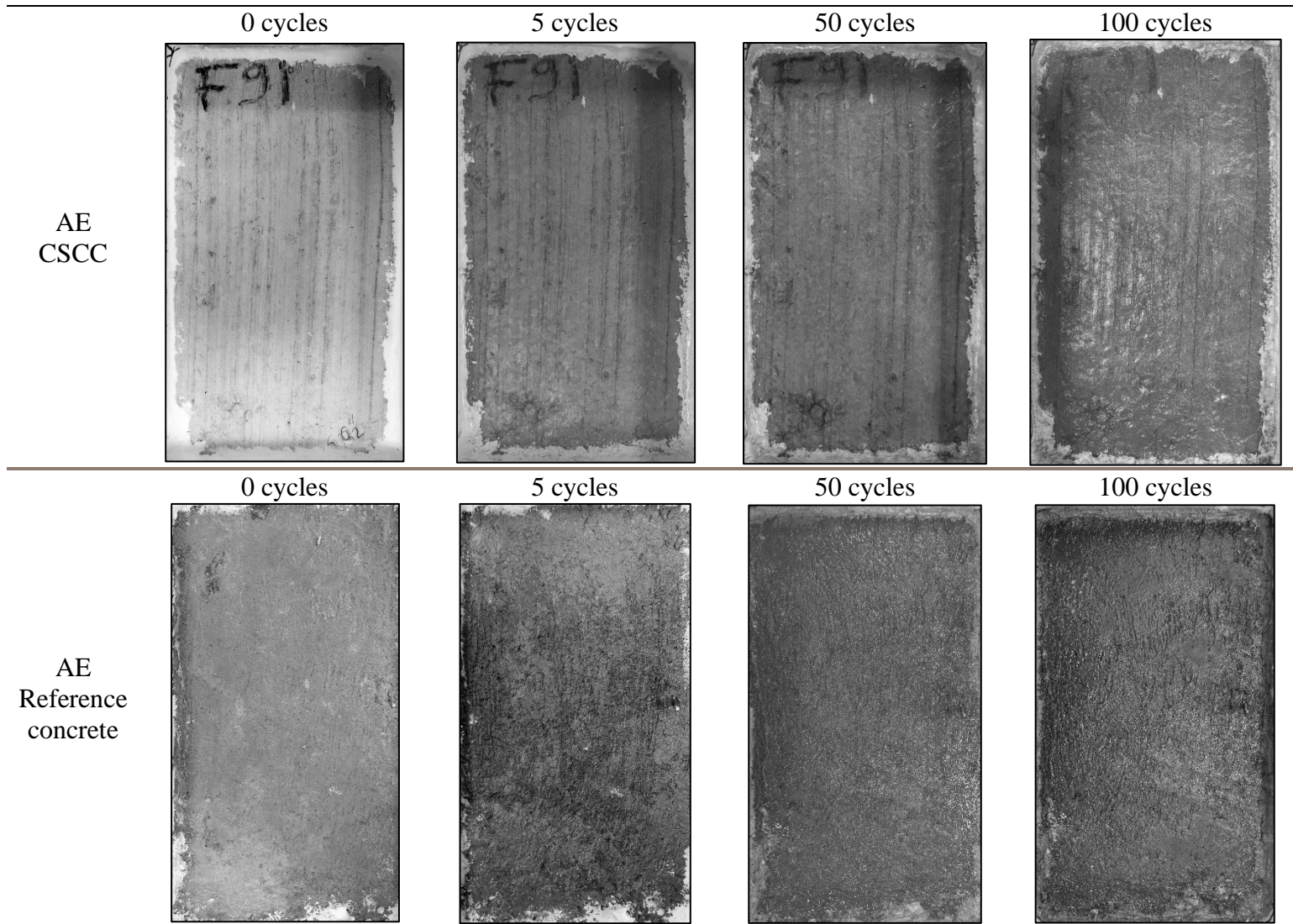


Figure 5.3 Appearances during scaling test (AE concretes)

5.3.2 Resistance to freezing-thawing

All of the CSC concrete specimens in this experiment contained 70~72% of aggregates that consisted of 42% coarse aggregate and 30% fine aggregate; a small volume of CSC paste would decrease the total water absorption and the connectivity of the pore network. The dimensions of the specimens met the requirement of ASTM C666; therefore, the freezing-thawing cycles (ASTM C666 procedure A) for the concrete specimens would not be as aggressive as for the CSC paste and mortar specimens in the previous chapter. Thus, it is more reasonable to use the freeze-thaw resistance test results of the CSC concrete in this chapter for making decisions regarding failure (below 60% RDME) as compared to the RDME results from Chapter 4.

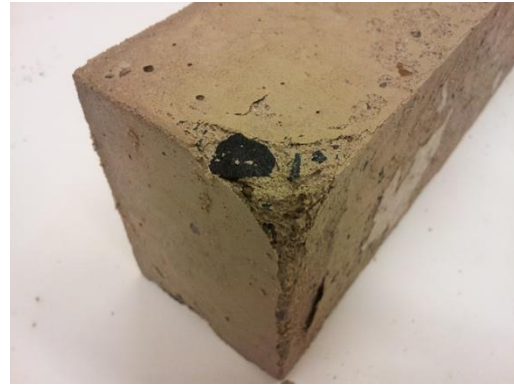
5.3.2.1 Air entrained vs. non-air entrained CSCCs

As shown in Figure 5.5 (a), non-air entrained (NAE) CSC concrete did not lose any mass loss during the experiment until 388 F/T cycles, although the layer of the finishing surface started scaling off and the erosion around the edge of the specimen was higher than that of the air entrained CSC concrete as the F/T cycles increased. This was because the NAE CSCC specimen consistently absorbed additional water during the experiment. Thus, the mass loss due to erosion may be compensated for by the mass of the water being absorbed. On the other hand, the mass of the air entrained (AE) CSC concrete increased because there was less surface scaling and the entrained air delayed the rate of water absorption; both specimens were soaked in water before the test.

The degree of RDME degradation associated with NAE CSCC was higher than that of AE CSCC and it sustained RDME above 60% until 300 F/T cycles. However, later, the RDME kept decreasing to 30% at approximately 800 F/T cycles, as shown in Figure 5.9.



(a) NAE CSCC after 33 F/T cycles



(b) NAE CSCC after 388 F/T cycles

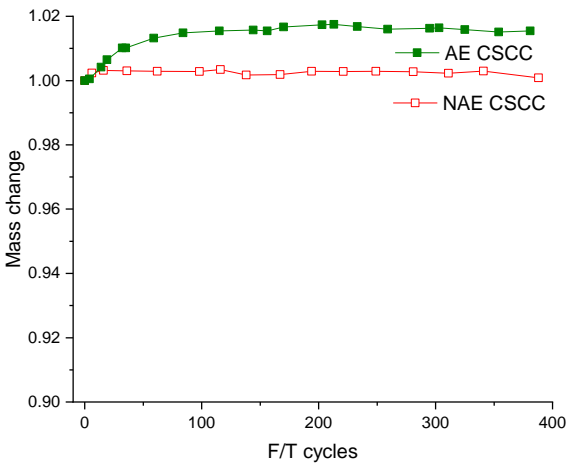


(c) NAE CSCC after 300 F/T cycles

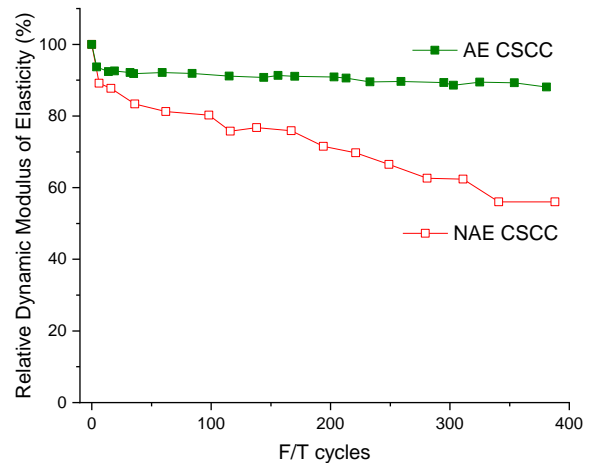


(d) AE CSCC after 300 F/T cycles

Figure 5.4 Appearance of the CSCC specimens



(a) mass change



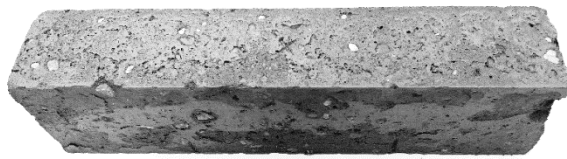
(b) RDME

Figure 5.5 Comparison of air entrained and non-air entrained CSCCs

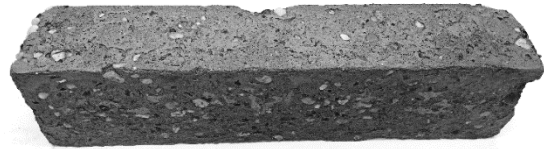
5.3.2.2 Crushed granite vs rounded pea gravel (AE CSCCs)

As discussed in Chapter 4, the rounded shape of the aggregate increases the connectivity of the pore network (i.e., decreases the tortuosity of the pore network), which may be detrimental to freezing and thawing resistance. In air entrained CSC concrete, the use of pea gravel had a

negative impact on freezing-thawing resistance because, unlike the other CSCC specimens, mass loss of the AE CSCC containing pea gravel decreased as the number of F/T cycles increased. Also, the RDME of the specimen containing pea gravel decreased more rapidly than the other CSCC specimens and the reading (RDME) was stopped at 230 F/T cycles. In this particular case, it is assumed that the disintegration between the CSC paste and the pea gravel was the main cause of failure, whilst the CSC paste was protected from the entrained air bubbles. The thin layer of cement paste (usually finishing surface) does not have sufficient space to mitigate the pressure due to ice formation while freezing; thus, the thin cement paste is likely to be detached [124]. This tendency would also occur in conventional concrete containing pea gravel [124]. This experiment confirmed that rounded shapes of aggregates decrease the tortuosity of the pore network as well as the bonding strength due to the small surface area of the aggregates (as compared to a crushed/angular shape of aggregates).



(a) AE CSCC-pea gravel at 30 F/T cycles



(b) AE CSCC-pea gravel at 88 F/T cycles



(c) AE CSCC-pea gravel at 150 F/T cycles



(d) AE CSCC-crushed aggregate at 575 F/T cycles

Figure 5.6 Appearances of the AE CSCC specimens

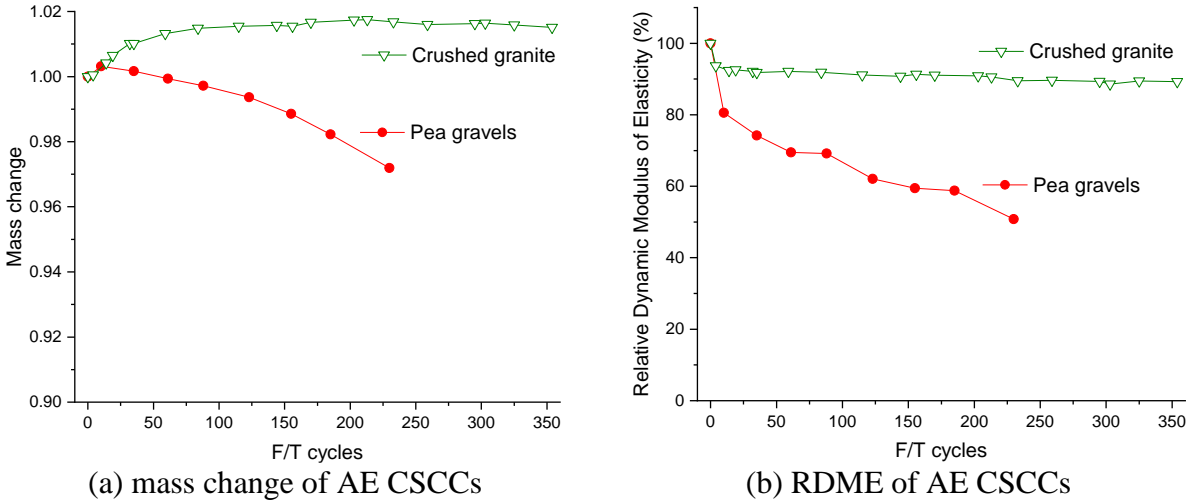


Figure 5.7 Comparisons of crushed granite and pea gravel

5.3.2.3 AE CSCC vs. AE reference concrete

Based on the previous experiments, AEA and crushed aggregates are the two design factors that allow the CSC system to perform better during F/T exposure. In this experiment, the CSC specimens were monitored for up to 1,000 F/T cycles and were compared with the freeze-thaw resistance of the AE reference concrete; the number of F/T cycles for testing described in ASTM C666 is up to 300 F/T cycles.

As mentioned earlier, ASTM E 1876 was used to calculate the relative dynamic modulus of elasticity (RDME), since it accounts for the mass variation of dynamic modulus of elasticity. The value of RDME determined by ASTM C666 was also provided because ASTM C666 is a protocol for testing the freeze-thaw resistance of concretes. These two different RDMEs are shown in Figure 5.9 (c) and (d). In this study, the F/T performance of the concrete specimens based on the results generated using ASTM E 1876 was discussed because the AE reference concrete experienced severe mass loss due to scaling along with freezing-thawing, as shown in Figure 5.8 (a) and (b).

AE CSCC did not reach failure and maintained its RDME over 80% even after 1,000 freezing-thawing cycles. However, NAE CSCC failed at approximately 330 F/T cycles, although there was almost no mass loss until failure, as shown in Figure 5.9 (a). The RDME of both air-entrained types of concrete dropped to below 95% prior to 30 F/T cycles, and then it degraded slowly as the number of freezing-thawing cycles increased. As shown in Figure 5.9 (b) and (c), the RDME of AE reference concrete increased between 60 and 90 F/T cycles. It is assumed that

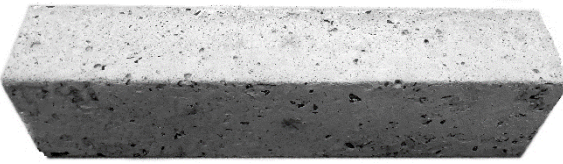
the increased RDME of AE reference concrete is the reason for the slow development of strength with the use of fly ash [117], [121]; the specimens were 50 days in age at this time. This assumption can also be explained by the observation that the RDME of CSCC did not increase during the experiment, since it reached full strength right after carbonation curing. It is interesting that the value of the dynamic modulus of elasticity of AE CSCC was higher during the entire experiment, although the RDME of AE CSCC was 1~2% lower than the reference concrete until 900 freezing-thawing cycles. Moreover, AE CSCC nearly maintained its original mass throughout the freezing-thawing test due to the slight damage from scaling and the additional water absorption. On the other hand, AE reference concrete started to present with scaling damage on the exposed surface within a few F/T cycles and, eventually, it could no longer measure RDME after 992 F/T cycles as a result of the severe degradation from scaling on the surface, as shown in Figure 5.8 (b). To understand this phenomenon, it was necessary to investigate the damaged microstructure of both specimens.



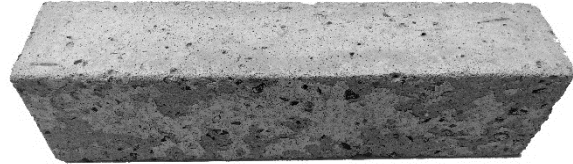
(a) AE reference concrete after 300 cycles



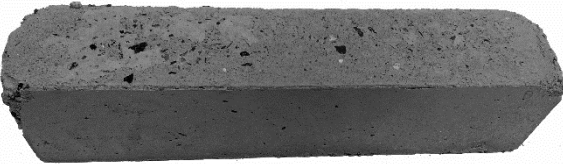
(b) AE reference concrete after 992 cycles



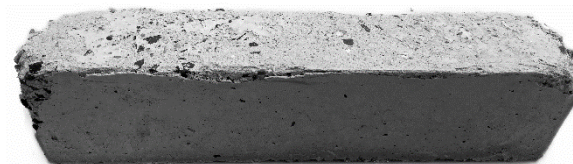
(c) AE CSCC after 300 cycles



(d) AE CSCC after 1,000 cycles

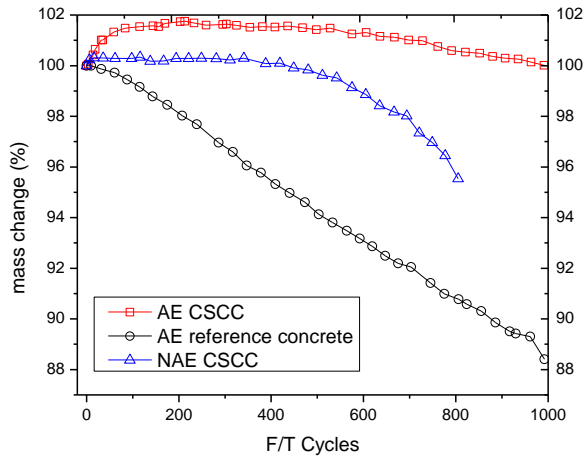


(e) NAE CSCC after 300 cycles

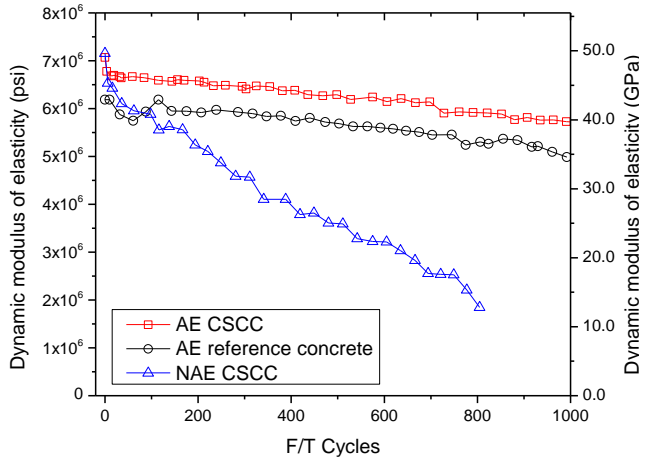


(f) NAE CSCC after 480 cycles

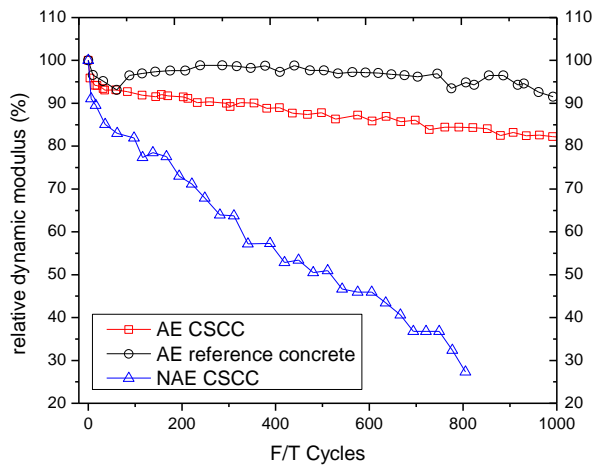
Figure 5.8 Appearances of the specimens after freezing-thawing test



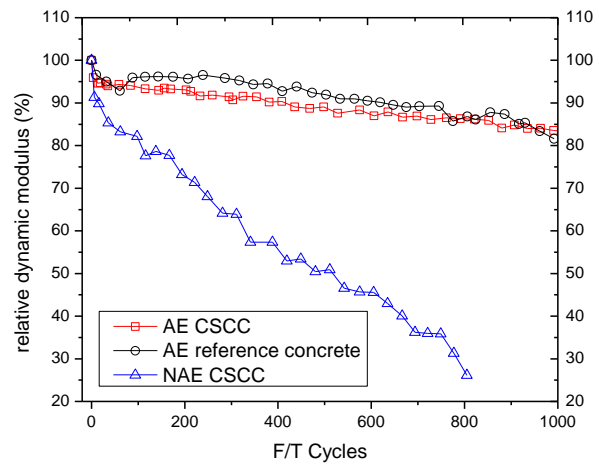
(a) mass change



(b) dynamic modulus of elasticity



(c) RDME by ASTM C666



(d) RDME by ASTM E 1876

Figure 5.9 Results from freezing-thawing experiment

5.3.3 SEM analysis

As shown in Figure 5.1, in order to compare the degree of damage based on location, two samples were taken from the concrete specimen; one was from the edge that was the most deteriorated and the other was taken from the inside of the concrete beam.

5.3.3.1 Edge of the concrete

If the samples had not been exposed to F/T cycles, the SEM image would display a solid matrix without the space filled within the diagonal lines, as shown in Figure 5.10 (a), (c) and (e). As a result of repeated F/T cycles, the space filled with diagonal lines was extensive in all types of specimens, as shown in Figure 5.10. The area of the space in the AE reference concrete was

larger than that of the AE CSCC. This was obvious because the result from the mass loss during the experiment showed that AE reference concrete suffered from the scaling damage; highly exposed the surface area of coarse aggregates was found as shown in Figure 5.8 (b). In both types of AE specimens, mass loss occurred because of the loss of paste and mortar content rather than the loss of coarse aggregates.

In terms of crack formation due to freezing-thawing cycles, CSCC presented discrete crack formation. Unlike the AE reference concrete, the cracks tended to be propagated through the ITZ in between the aggregate and CSC paste. This likely happened because the air was not entrained in the CSC system, as shown in Figure 5.10 (e) and (f). Thus, excessive cracks were found in the NAE CSCC specimen; also, there was a lack of air voids for minimizing the hydraulic pressure resulting from the formation of ice. Based on the findings discussed in Chapter 3, this formation of cracks was predictable; the CSC system contained more porous ITZ as compared to the OPC system. In other words, the space between aggregate and cement paste in CSCC provided easier access for the retention of external water than the path through the air voids in the CSC paste. Additionally, the air voids in AE CSCC were relatively insufficient as compared to the AE reference concrete. The air voids were surrounded by calcium carbonates and unreacted CSC, as shown in Figure 5.10 (h).

As a comparison, the crack formation in the AE reference concrete was propagated through the entrained air voids (Figure 5.10 (g)), which resulted from the hydraulic pressure that was delivered to vicinity of the voids by the action of freezing-thawing [60]. Also, the air voids in the AE reference concrete were more frequently found and were well-distributed.

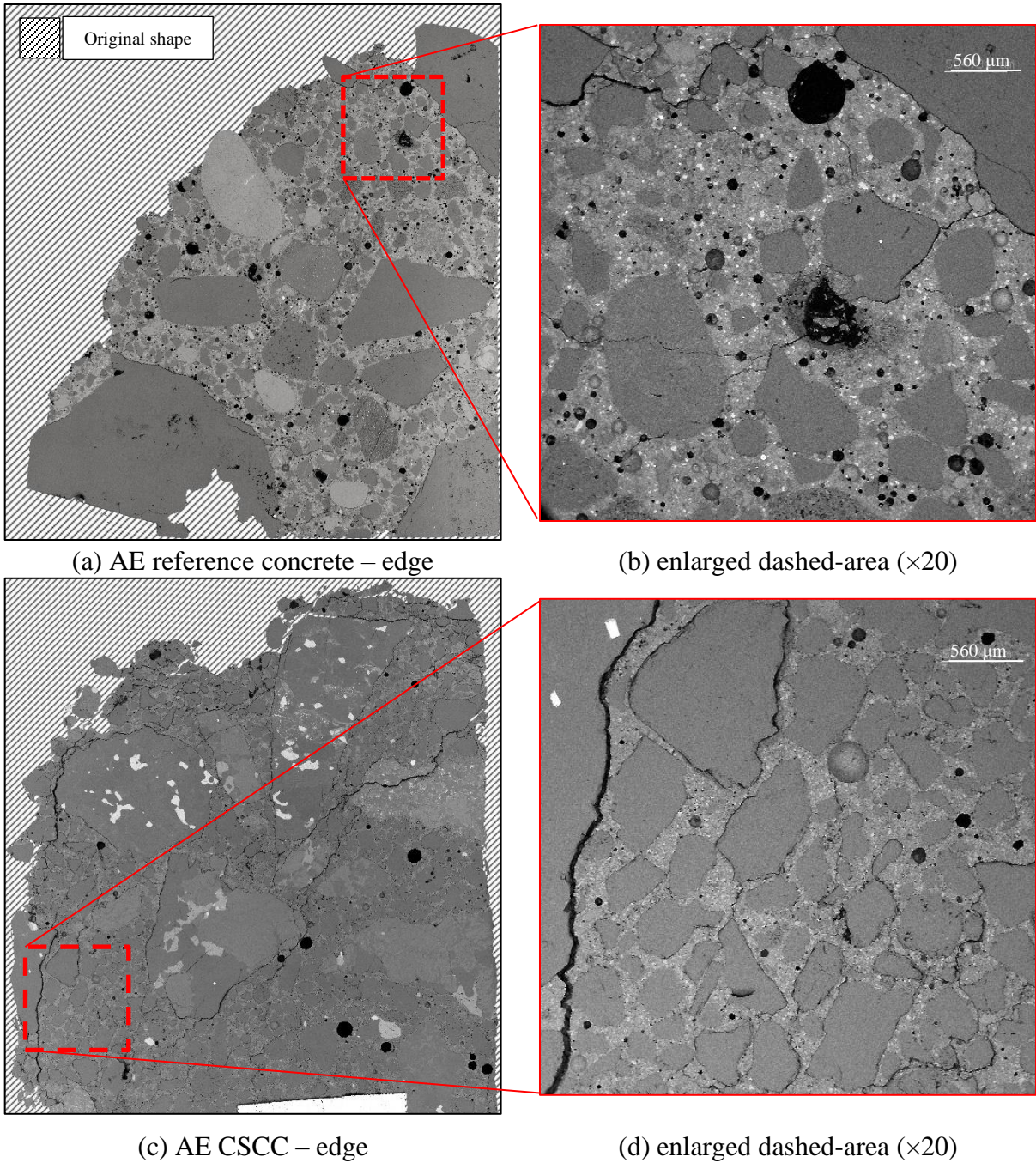
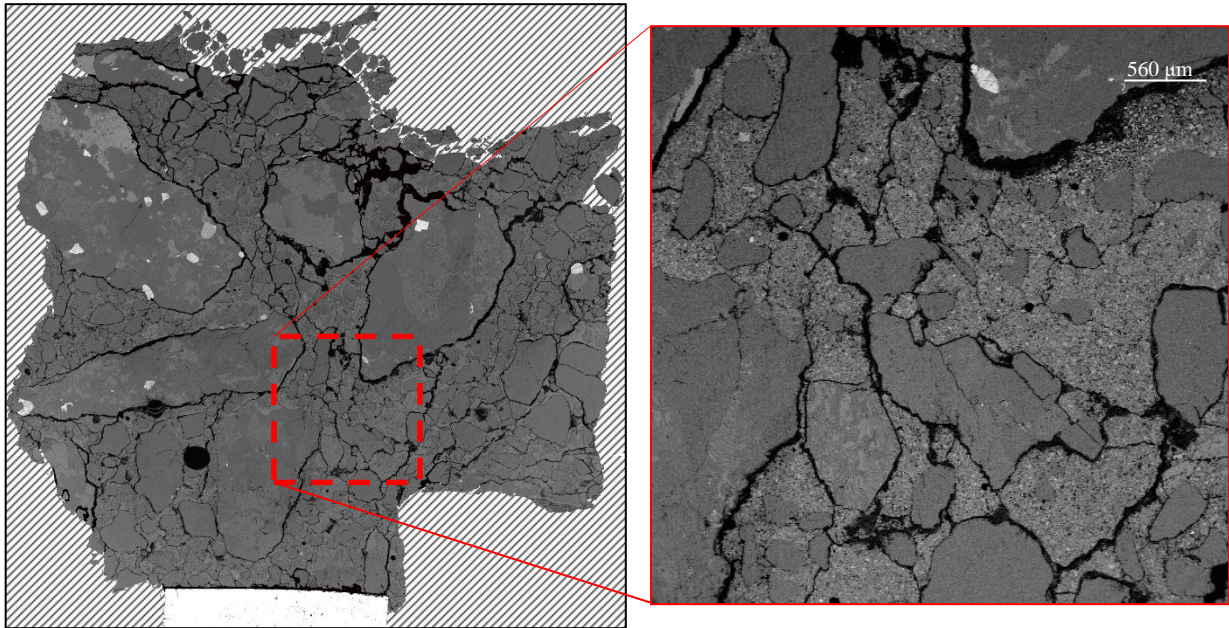


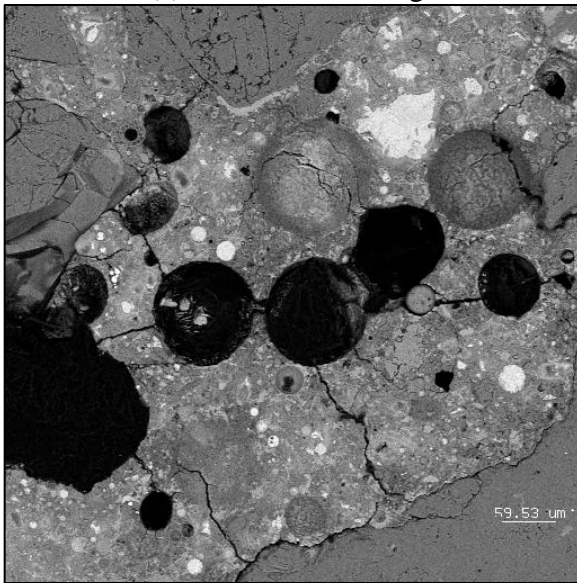
Figure 5.10 BSE images of the edge of each specimen

Figure 5.10 continued

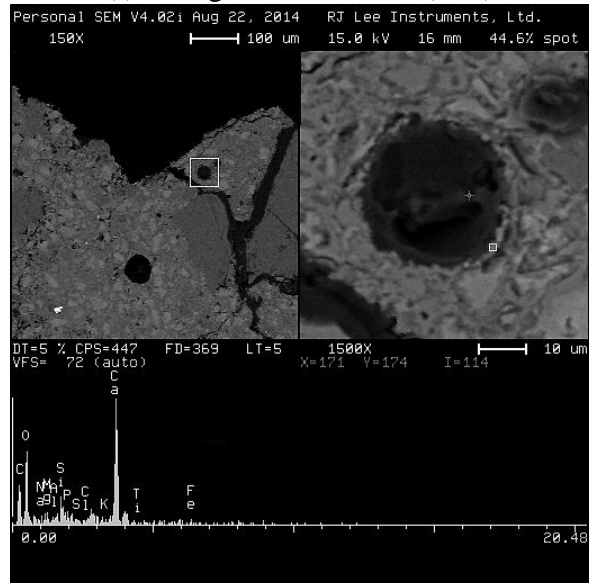


(e) NAE CSCC – edge

(f) enlarged dashed-area (×20)



(g) AE reference concrete – air voids

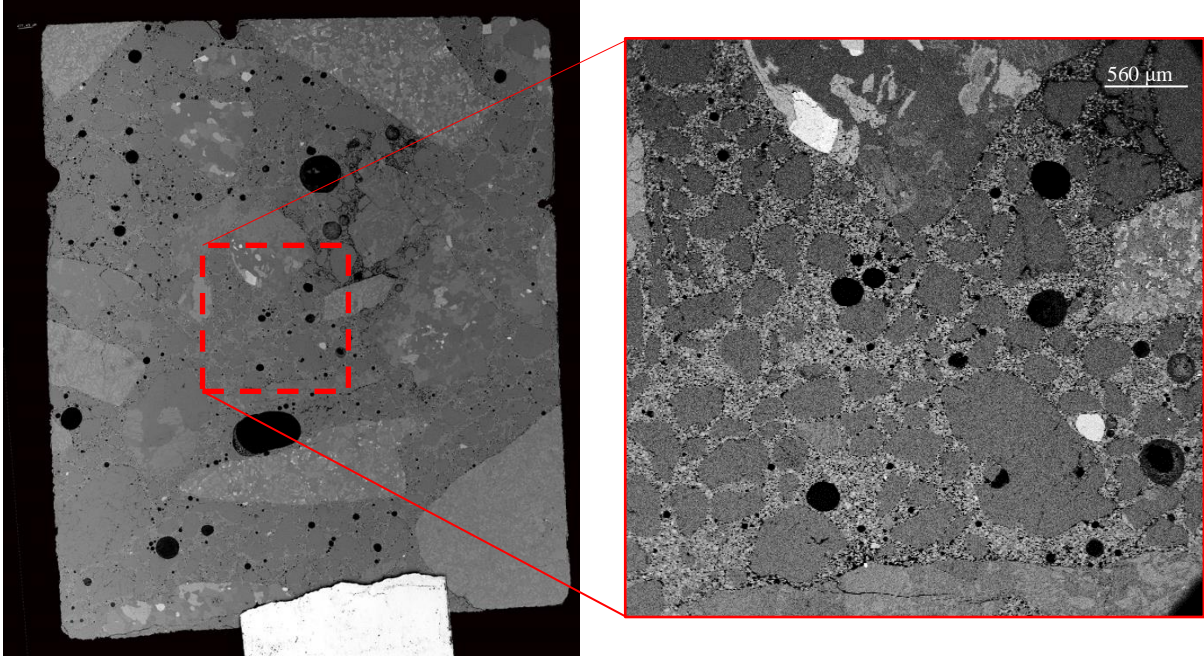


(h) AE CSCC – air voids

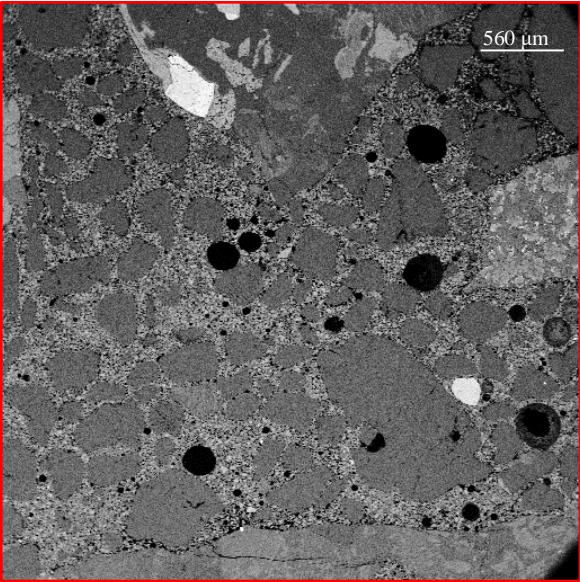
5.3.3.2 Inside of the concrete

The inside part of the specimens was assumed to be less damaged from F/T attacks because most of the damage was initiated at the surface and edge of the specimens. The formation of cracks was not found in this area, as the cracks present around the edge of the specimens. AE CSCC showed entrained air bubbles throughout the CSC system whilst NAE CSCC showed

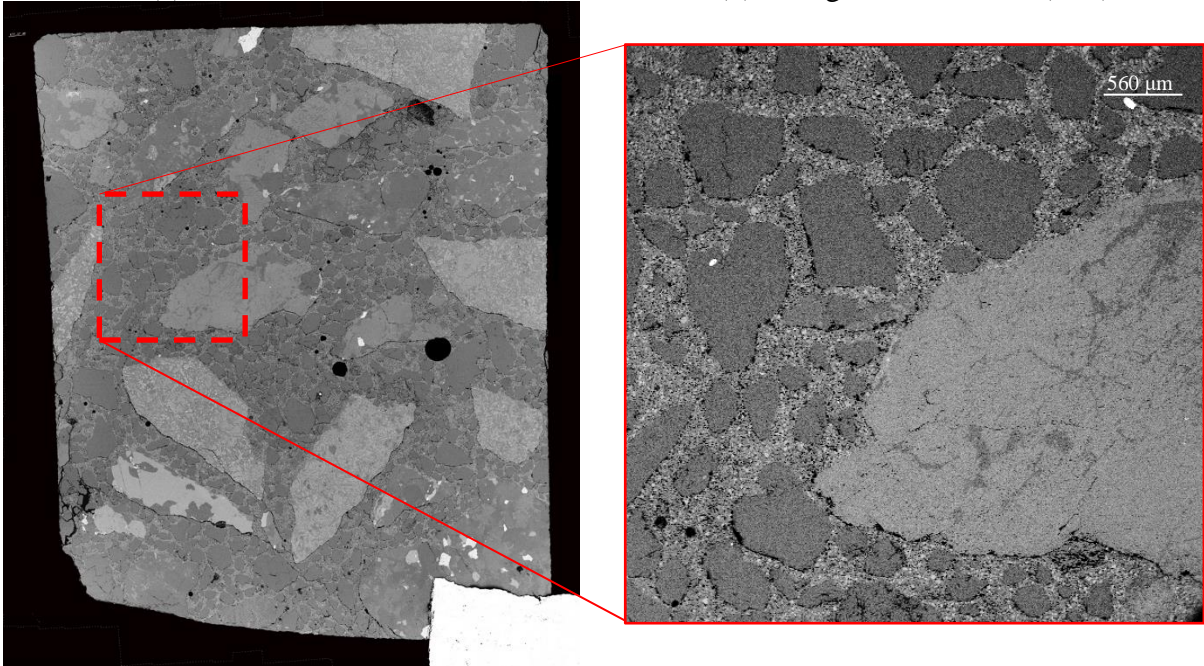
almost no air bubbles but porous ITZ was observed. The air void system in the AE reference was relatively well-distributed as compared to the air void system in the AE CSCC specimen.



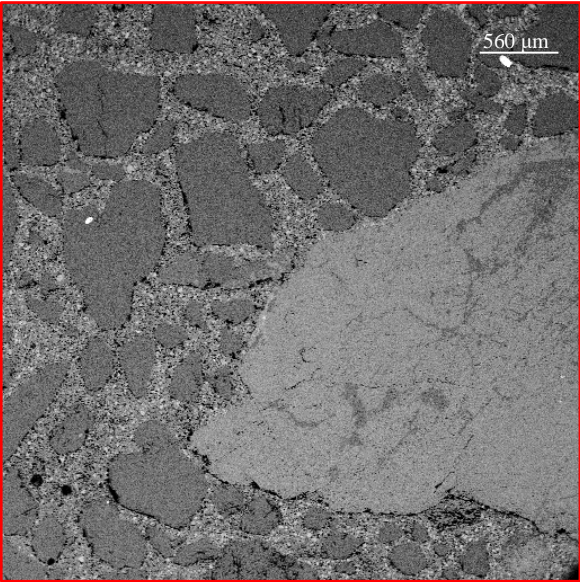
(a) AE CSCC – inside



(b) enlarged dashed-area (×20)



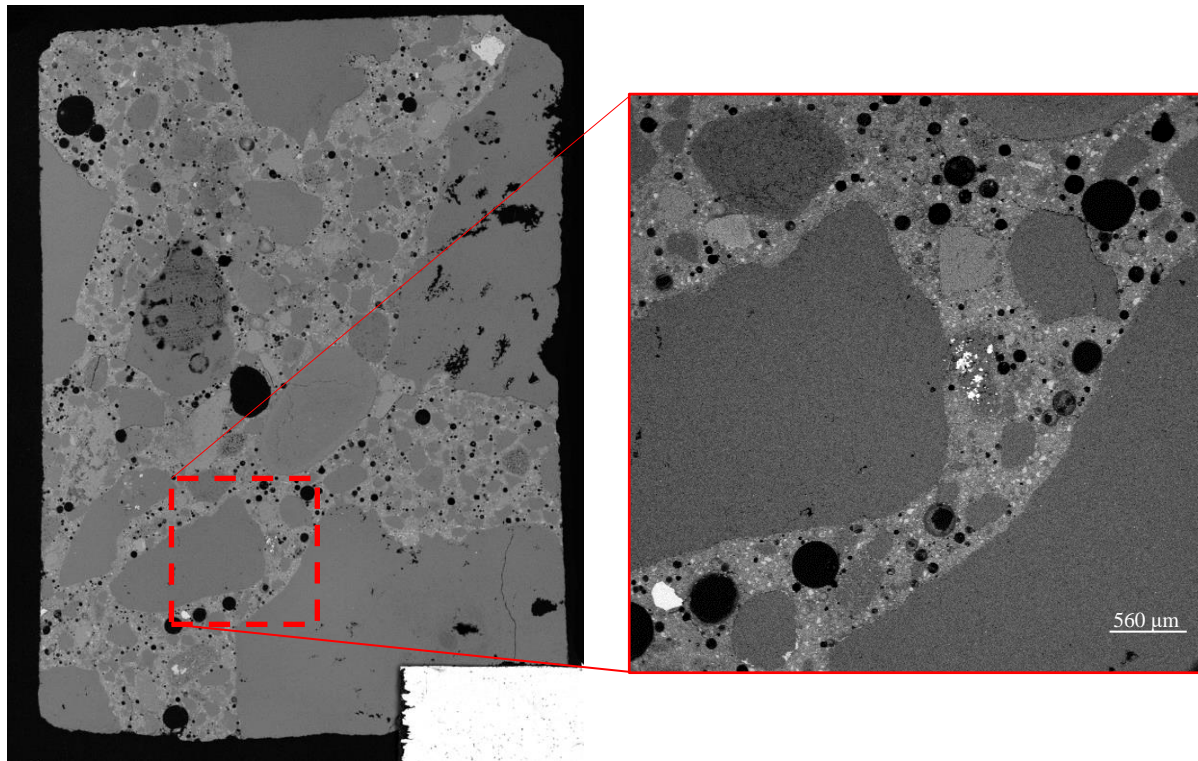
(e) NAE CSCC – inside



(f) enlarged dashed-area (×20)

Figure 5.11 BSE images of the inside of the specimens

Figure 5.11 continued



(e) AE reference concrete – inside

(f) enlarged dashed-area (×20)

5.3.4 Air void spacing factor

As mentioned earlier, a similar specimen compressive strength was selected in order to compare the freezing-thawing resistance of each type of concrete. To understand why both AE concretes performed well under the actions of freezing-thawing, it would be beneficial to measure the air-void content and spacing factor in the concretes since the air-voids system plays a significant role in resistance to freezing-thawing [60], [71]. For instance, if the air voids provide sufficient space in the concrete for releasing internal stress through the near voids, there would be less damage due to the expansion resulting from ice formation. Thus, it is also important to understand how air voids are well-spaced from each other [71]. According to the Portland Cement Association, the desired length of the spacing factor for freeze-thaw durability should be less than 0.008 inch [71]. As shown in Table 5.5, both air-entrained specimens satisfied the spacing factor requirement and provided acceptable air content for freeze-thaw durability. Thus, in terms of RDME, both air-entrained specimens performed well until 1,000 freezing and thawing cycles.

One interesting result was that the air content and void frequency of AE reference concrete were higher than those of AE CSCC, which reflects that the efficiency of AEA was lower in CSCC, as described in Section 4.3.3. Consequently, the RDME of AE CSCC had a lower value than AE reference concrete. Additionally, to confirm the efficiency of AEA, the volume of permeable pore space was determined by ASTM C 642. The result also demonstrated that AE reference concrete provided a better air void system, since it had a higher volume of permeable pore space that was a combination of higher w/c and greater effectiveness of AEA. This part of the study regarding the air voids system in CSC should be further investigated in the future.

Table 5.5 Parameters related to air void system of air-entrained specimens

	AE reference concrete	AE CSCC
Air content (%)	8.41	7.13
Void frequency (/in)	10.18	4.67
Specific surface (in ² /in ³)	484.17	261.93
Spacing factor (in)	0.0015	0.0024
Absorption (%)	4.97	2.66
Volume of permeable pore space (%)	11.09	5.92

5.4 Conclusions

The scaling performance of AE CSCC was outstanding in the presence of 4% CaCl₂ because the CSC system does not have calcium hydroxide nor detrimental chemical compositions (i.e., calcium oxychlorides and gypsum).

In this chapter, for freeze-thaw performance, three different mixtures of CSCC were evaluated and compared to the AE reference concrete. It was inevitable that the CSCC required two essential factors that enhanced its serviceability under F/T conditions: the angular shape of aggregates and air entrainment. The AE CSCC containing rounded pea gravel performed worse than the NAE CSCC containing crushed granite in terms of freeze-thaw resistance. The lower surface area of aggregates, reduction in bonding and tortuosity of the pore network, resulted in excessive mass loss and degradation of the dynamic modulus of elasticity. However, in the case of the CSCCs containing crushed granite, mass loss was negligible, although the damage started at the edge of the CSCCs. Additionally, the finishing surfaces were scaled off as soon as the F/T

cycle was initiated. When a combination of AEA and crushed granite was used in CSCC specimens, freeze-thaw damage was minimized; the AE CSCC sustained its structural integrity until the 1,000 F/T cycle. As compared to the AE CSCC, the AE reference specimen showed 1~2% higher RDME throughout most of the experiment; however, the mass loss of the AE reference concrete was more severe as compared to the CSCC specimens containing crushed granite. The dynamic modulus of elasticity of the AE CSCC that was calculated by ASTM E1876 was higher than the AE reference concrete throughout the entire experiment. With a similar compressive strength, AE CSCC provided less void frequency, air content, and permeable pore space, which may have been caused by the inefficiency of the AEA as compared to the AE reference concrete. This may result in the concrete having a lower relative dynamic modulus of elasticity during exposure to freezing-thawing cycles than that of AE reference concrete; but it still performed well during the freezing-thawing cycles.

6. CONCLUSIONS AND FUTURE STUDIES

6.1 Conclusions

The new cement, CSC, used in this investigation consists mostly of wollastonite, rankinite, and some belite and is non-hydraulic. As such it hardens by carbonation, not by hydration (as is the case for OPC). Due to this unique hardening process, the properties of the CSC concrete are different from conventional concretes, which may limit or broaden the prospective uses of concrete based on this binder. Thus, although the mechanical performance of this new CSCC is comparable to that of the OPC-based concrete, the information on the durability of this new CSCC is still lacking. This study focused on the characterization of the pore system of the CSC system and its effect on the sorptivity and freeze-thaw resistance of CSCC. The major findings are summarized below.

6.1.1 Pore system characterization of carbonated CSC paste and mortars

Initially, uncarbonated CSC paste contained approximately 56% porosity (at w/c=0.3). During the carbonation curing pores became filled with carbonation products and at the completion of the carbonation process the porosity was reduced to about 20%. At this time, the CSC paste contained ~30% calcium carbonates by weight. In addition, the total porosity of carbonated CSC paste increased as the water-to-cement ratio increased.

In 0.3 w/c of CSC paste, two distinctive pore ranges were detected by MIP: small (gel) capillary pores (5 nm~100 nm) and large capillary pores (30 μm ~100 μm). The small capillary pores were found in between crystals of calcium carbonate and the large capillary pores were found in bulk matrix.

This unique pore size distribution observed in the carbonated CSC paste was affected by the presence of aggregates in the matrix. The total porosity of the CSC system decreased as the volume of the aggregate content increased (due to reduction in the volume of the paste). However, the differences in total porosity between 0.3C30 and 0.3C55 mortars were practically negligible. This was due to the increased volume of the porous ITZ in the CSC system resulting from higher volume of the aggregates. However, introduction of higher volume of aggregate resulted in creation of pores with different size range (from 0.1 to 4 μm) compared to 0.3C30

mortar. The observed thickness of the ITZ was approximately 10 μm with porosity decreasing with the increase in the distance from the surface of the aggregate. This tendency for decrease in porosity with the increase in the distance from the surface of the aggregate was also found in the OPC system, but in that case the total porosity was almost two times lower than that of the CSC system. Also, while micro-cracks were present in OPC mortars at the boundary between aggregates and pastes, CSC mortars contained porous areas without micro-cracks. The porous ITZ present in the CSC system is expected to increase the connectivity of the pores.

6.1.2 The rate of water absorption (sorptivity) of carbonated CSC paste and mortars

The CSC paste absorbed the amount of water equal to approximately 80% of its total absorption capacity in 6 hours and reached nearly 97% saturation in 24 hours. This initial sorptivity and the total absorption were both reduced with the increase in the volume of the aggregate. The time to reach given level of saturation in the CSC mortar was significantly delayed compared to the CSC paste, with 80% saturation achieved in 3-4 days and 97% saturation achieved in ~ 5 days. Since the initial sorptivity is related to the rate of development of F/T damage, AEA was used to reduce the value of initial sorptivity as the presence of larger air bubbles reduces the rate of water absorption.

The initial sorptivity of air-entrained CSC paste was approximately three times lower than that of the non-air entrained CSC paste. However, the initial sorptivities of the CSC mortars were not significantly affected by introduction of the entrained air. Moreover, the peak saturation levels in both, paste and mortar AE CSC specimens, were not much different from those observed in the non-AE CSC specimens. One possible reason for this behavior was the fact that the boundaries of the air-entrained voids present in the CSC specimens were relatively porous and thus connected to the system of capillary pores. In contrast, the boundaries of the air-entrained voids in the AE OPC system were relatively denser (less porous) thus reducing the overall saturation level over time.

One significant difference between the CSC and OPC systems was the initial saturation level at the beginning of the sorptivity experiment. Due to preconditioning (50% RH for 15 days) prior to the test, the starting saturation levels for CSC paste and mortars (10~20%) were significantly lower than those of the OPC system (about 75%). This indicates that CSC systems

contained mostly capillary pores and that only small (gel-size) capillary pores were filled with moisture during conditioning at 50% RH.

6.1.3 Effect of AEA on freeze-thaw resistance of carbonated CSC paste and mortars

The non-AE CSC paste failed after only a few (around 4) F/T cycles and the non-AE CSC mortars failed after 36 F/T cycles. The early failure of the non-AE system was the direct consequence of the lack of air bubbles that can relieve the pressure generated by water expelled from the saturated capillaries during the freezing event.

The F/T resistances of the CSC specimens was significantly improved by introduction of the system of entrained air. Specifically, the AE CSC paste was able to sustain up 156 F/T cycles and the AE CSC mortars were able to maintain their structural integrity up to until the end of the experiment (300 F/T cycles). Also, the degradation process of the AE CSC specimens was much more gradual than a more sudden failure observed in the non-AE CSC specimens. One interesting point was that the end of the test (after 300 F/T cycles) the RDME values of 03C55A mortars lower than that of 03C30A mortars. This may have been caused by the larger volume of porous ITZ present in 03C55A specimens.

6.1.4 Freeze-thaw resistance of CSCC vs. reference concrete

To evaluate the extent to which the differences in pore structure of the CSC and OPC systems influence the F/T resistance of corresponding concretes, three different CSCC mixtures were produced and tested. These included non-AE and AE concretes with crushed granite coarse aggregate and AE concrete with pea gravel. The F/T performance of these mixtures was compared to F/T performance of AE reference concrete. The reference concrete, based on binary binder system (OPC + 20% of fly ash) and crushed limestone as a coarse aggregate was previously found to perform well under F/T conditions. The F/T performance of AE CSCC containing crushed granite was found to be comparable to that of the reference concrete whereas the other two CSCC mixtures suffered more severe damage.

The AE CSCC specimens containing the crushed granite maintained their structural integrity up to 1,000 F/T cycles and lost the least amount of mass compared to the other two CSCCs. On the other hand, it was impossible to consistently and accurately measure the resonant

frequencies of the AE reference concrete specimens past 992 F/T cycles due to extensive scaling which prevented the probe from making a good contact with the surface. The edges of all concrete beams were more susceptible to F/T damage than the other parts of the beams.

The cracks observed in the AE CSCC were located at the boundary between the aggregate and paste whilst cracks in the AE reference concrete were found propagating throughout the entrained air voids. In the case of non-AE CSCC, extensive cracking was observed near the outer surfaces and edges of the specimens. This cracking caused debonding of aggregates from the CSC paste. The number of cracks observed in the center of the specimens (i.e. away from external surfaces and edges) was much lower.

6.1.5 Methods for enhancement of freeze-thaw resistance of CSCC

The main aim of this study was to estimate and to enhance the freeze-thaw resistance of the CSCC system. For this purpose, the characteristics of the pore system of CSCC need to be altered in the following ways. First, AEA should be introduced as it was found to significantly improve the freeze-thaw performance of CSCC. The entrained air bubbles delayed the initial sorptivity and provided extra space that relieved the internal stress caused by ice formation.

Second, reducing the volume of porous ITZ is essential for improving freeze-thaw resistance. The porous ITZ increases pore connectivity and decreases tortuosity of the pore network; thus, it causes a higher degree of degradation due to freeze-thaw attacks as compared to the system with lower volume of porous ITZ. Also, larger sized aggregates help to reduce the area of the porous ITZ, by reducing the surface area of aggregate.

Third, strengthening the bond between aggregates and CSC paste increases the freeze-thaw resistance of the CSCC. The angular shape of the coarse aggregates increases the tortuosity of the pore network and increases the bond strength. The freeze-thaw performance of AE CSCC containing crushed granite was better (the RDME higher than 90% at the end of 350 F/T cycles) than that of the AE CSCC containing rounded pea which failed after 230 F/T cycles (RDME ~50%).

6.2 Future study

Based on the research presented in this dissertation, two distinct lines of future studies are proposed as briefly described below.

As demonstrated in this dissertation, the effectiveness of the AEA when used in the CSC system was reduced when compared to the effectiveness of the same admixture used in the OPC system. Specifically, the frequency of entrained air voids was lower in the AE CSC system than in the OPC system. This may have been caused by the low water-to-cement ratio of the CSC system, and the difficulties with stabilization of the entrained air bubbles under the conditions of high curing temperatures during the carbonation process. Thus, it would be useful to study the stabilization of the entrained air bubbles during the carbonation process using various dosages of AEA and varying the values of w/c.

Another potential future study can involve determination of whether such properties of aggregate as shape, absorption, surface area and gradation effect the freeze-thaw resistance of AE CSCC. Since densifying of ITZ is essential for improving scaling and freeze-thaw resistance of AE CSCC, optimization the gradation of coarse and fine aggregates potentially offer another way to enhance the CSCC performance, not only with respect to durability but also with respect to mechanical properties.

REFERENCES

- [1] M. Crippa *et al.*, “Fossil CO₂ and GHG emissions of all world countries - 2019 Report,” Luxembourg, 2019.
- [2] R. M. Andrew, “Global CO₂ emissions from cement production, 1928-2019,” *Earth System Science Data*, pp.1-67, 2019.
- [3] United States Environmental Protection Agency, *U.S. Greenhouse Gas Emissions and Sinks, 1990-2016 (EPA 430-R-18-003)*. EPA, Washington D.C., 2018.
- [4] WBCSD and IEA, “Cement Technology Roadmap 2009: Carbon emissions reductions up to 2050,” 2009.
- [5] S. Kosmatka, B. Kerkhoff, and W. C. Panarese, “Fly Ash , Slag , Silica Fume , and Natural Pozzolans,” in *Design and Control of Concrete Mixtures*, 14th ed., Skokie, Illinois: Portland Cement Association, 2002, pp. 57–72.
- [6] ACI Committee 232, *Report on the Use of Raw or Processed Natural Pozzolans in Concrete (ACI 232 IR-12)*. American Concrete Institute, Farmington Hills, MI, 2012.
- [7] J. Davidovits, “Geopolymers,” *J. Therm. Anal.*, vol. 37, no. 8, pp. 1633–1656, 1991.
- [8] D. Khale and R. Chaudhary, “Mechanism of geopolymerization and factors influencing its development: A review,” *J. Mater. Sci.*, vol. 42, no. 3, pp. 729–746, 2007.
- [9] J. S. J. Van Deventer, J. L. Provis, and P. Duxson, “Technical and commercial progress in the adoption of geopolymer cement,” *Miner. Eng.*, vol. 29, pp. 89–104, 2012.
- [10] B. V. Rangan, “Geopolymer concrete for environmental protection,” *Indian Concr. J.*, vol. 88, no. 4, pp. 41–59, 2014.
- [11] L. Barcelo, J. Kline, G. Walenta, and E. Gartner, “Cement and carbon emissions,” *Mater. Struct.*, vol. 47, no. 6, pp. 1055–1065, 2014.
- [12] W. Kurdowski, *Cement and Concrete Chemistry*. Springer, 2014.
- [13] Aether-cement.eu, “Aether ® lower carbon cements,” Lafarge, 2014. [Online]. Available: <http://www.aether-cement.eu/>.
- [14] S. P. Deolalkar, “Cement Substitutes,” in *Designing Green Cement Plants*, 2016, pp. 379–384.

- [15] E. Gartner and T. Sui, “Alternative cement clinkers,” in *Cement and Concrete Research*, Elsevier Ltd, 2016.
- [16] J. H. Sharp, C. D. Lawrencef, and R. Yang, “Calcium sulfoaluminate cements — low-energy cements , special cements or what?,” *Adv. Cem. Res.*, vol. 11, no. 1, pp. 3–13, 1999.
- [17] V. Atakan, S. Sahu, S. Quinn, X. Hu, and N. Decristofaro, “solidia why CO₂ matters,” *ZKG international*, vol. 67, no. 3, pp. 60–63, 2014.
- [18] S. Sahu and N. DeCristofaro, “Part One of a Two-Part Series Exploring the Chemical Properties and Performance Results of Sustainable Solidia Cement™ and Solidia Concrete™,” 2013. [Online]. Available: <http://solidiatech.com/wp-content/uploads/2014/02/Solidia-Cement-White-Paper-12-17-13-FINAL.pdf>.
- [19] S. Mindess, J. F. Young, and D. Darwin, *Concrete*, 2nd ed. Englewood Cliffs, NJ: Prentice Hall, 2003.
- [20] K. K. Aligizaki, *Pore structure of cement-based materials*. New York, NY: Taylor and Francis, 2006.
- [21] T. C. Powers, “Freezing Effects in Concrete,” in *Durability of Concrete*, American Concrete Institute SP 47-1, 1975, pp. 1–11.
- [22] R. A. Helmuth, “Capillary Size Restrictions on Ice Formation in Hardened Cement Pastes,” *4th Int. Symp. Chem. Cem.*, Washington D.C., vol. 2, pp. 855–869, 1960.
- [23] G. Fagerlund, “A Service Life Model for Internal Frost Damage in Concrete,” Report TVBM-3119, Division of Builing Materials, Lund Institute of Technology, Lund University, Sweden, 2004.
- [24] T. C. Powers, “Hydraulic Pressure in Concrete,” *PCA Bulletin 63*, Research and Development Laboratories of the Portland Cement Association, Chicago, IL, April, 1956.
- [25] W. Thomson, “The effect of pressure in lowering the freezing-point of water experimentally demonstrated,” *London, Edinburgh, Dublin Philos. Mag. J. Sci.*, vol. 37, no. 248, pp. 123–127, 1850.
- [26] V. Penttalla, “Freezing-induced strains and pressures in wet porous materials and especially in concrete mortars,” *Adv. Cem. Based Mater.*, vol. 7, no. 1, pp. 8–19, 1998.
- [27] The Aberdeen Group, “Air entrainment and concrete,” Publication# C760105, Aberdeen Group, 1976.

- [28] W. Li, M. Pour-Ghaz, J. Castro, and J. Weiss, “Water Absorption and Critical Degree of Saturation Relating to Freeze-Thaw Damage in Concrete Pavement Joints,” *J. Mater. Civ. Eng.*, vol. 24, pp. 299–307, 2012.
- [29] R. Gagné, E. Houehanou, M. Jolin, and P. Escaffit, “Study of the relationship between scaling resistance and sorptivity of concrete,” *Can. J. Civ. Eng.*, vol. 38, no. 11, pp. 1238–1248, 2011.
- [30] J. Zhang and P. C. Taylor, “Pore Size Distribution in Cement Paste in Relation to Freeze-Thaw Distress,” *J. Mater. Civ. Eng.*, vol. 27, no. 23, pp. 1–6, 2015.
- [31] D. P. Bentz, M. Ehlen, C. F. Ferraris, and E. J. Garboczi, “Sorptivity-based service life predictions for concrete pavements,” in *7th International Conference on Concrete Pavements*, International Society for Concrete Pavement, 2001, vol. 1, pp. 181–193.
- [32] Z. Li, *Advanced Concrete Technology*. John Wiley & Sons, 2011.
- [33] Ö. Cizer, C. Rodriguez-Navarro, E. Ruiz-Agudo, J. Elsen, D. Van Gemert, and K. Van Balen, “Phase and morphology evolution of calcium carbonate precipitated by carbonation of hydrated lime,” *J. Mater. Sci.*, vol. 47, no. 16, pp. 6151–6165, 2012.
- [34] D. R. Moorehead, “Cementation by the carbonation of hydrated lime,” *Cem. Concr. Res.*, vol. 16, pp. 700–708, 1986.
- [35] R. Camerini, G. Poggi, D. Chelazzi, F. Ridi, R. Giorgi, and P. Baglioni, “The carbonation kinetics of calcium hydroxide nanoparticles: A Boundary Nucleation and Growth description,” *J. Colloid Interface Sci.*, vol. 547, pp. 370–381, 2019.
- [36] T. Yates and A. Ferguson, *The use of lime-based mortars in new build*. NHBC Foundation, 2008.
- [37] J. Jain, O. Deo, S. Sahu, and N. Decristofaro, “Part Two of a Series Exploring the Chemical Properties and Performance Results of Sustainable Solidia Cement™ and Solidia Concrete™,” 2014. [Online]. Available: <http://solidiatech.com/wp-content/uploads/2014/02/Solidia-Concrete-White-Paper-FINAL-2-19-14.pdf>.
- [38] R. Tokpatayeva, J. Olek, D. Ravikumar, and V. Atakan, “Cement - A novel calcium silicate-based cement – Microstructure and Soak-solution chemistry,” *Poster session of Advancend in Cement-based Materials*, Advanced in Cement-based Materials, Cookville, TN, July, 2014.

- [39] N. Decristofaro and S. Sahu, “CO₂ Reducing Cement,” *World Cement*, pp. 2–5, 2014.
- [40] H. M. Jennings and P. D. Tennis, “Model for the developing microstructure in Portland cement pastes,” *J. Am. Ceram. Soc.*, vol. 77, no. 12, pp. 3161–3172, 1994.
- [41] H. M. Jennings, “Model for the microstructure of calcium silicate hydrate in cement paste,” *Cem. Concr. Res.*, vol. 30, no. 1, pp. 101–116, 2000.
- [42] R. F. Feldman and P. J. Sereda, “A New Model for Hydrated Portland Cement and its Practical Implications,” *Eng. J.*, vol. 53, no. 8/9, pp. 53–59, 1970.
- [43] T. Powers and T. Brownyard, “Studies of the physical properties of hardened Portland cement paste part 2,” *ACI J. Proc.*, vol. 18, no. 3, pp. 249–336, 1946.
- [44] T. C. Hansen, “Physical structure of hardened cement paste. A classical approach,” *Mater. Struct.*, vol. 19, no. 6, pp. 423–436, 1986.
- [45] T. C. Powers, “Structure and Physical Properties of Hardened Portland Cement Paste,” *Am. Ceram. Soc.*, vol. 41, pp. 1–6, 1958.
- [46] H. Jennings, “Water Sorption in Cement Paste: A Link Between Meso-Pore and Properties: Reversible and Irreversible Deformation,” in *Multiscale Materials Modeling Workshop Summary Report*, T. Morton Eds., The Federal Highway Administration, Washington D.C., 2013, pp. 4–5.
- [47] T. C. Powers and T. L. Brownyard, “Studies of the Physical Properties of Hardened Portland Cement Paste Part 3. Theoretical Interpretation of adsorption Data,” *ACI J. Proc.*, vol. 18, no. 4, pp. 469–504, 1946.
- [48] C. Villani, R. Spragg, R. Tokpatayeva, J. Olek, and J. Weiss, “Characterizing the Pore Structure of Carbonated Natural Wollastonite,” in *Proceedings of the 4th International Conference on the Durability of Concrete Structures*, J. Olek and J. Weiss, Eds. West Lafayette, IN: Purdue University, 2014, pp. 262–269.
- [49] W. Ashraf, “Reaction Kinetics, Microstructural Features and Mechanical Properties of CO₂ Activated Low-lime Calcium Silicate Binders,” *Ph.D. dissertation*, Civil Engineering and Material science, Purdue University, 2017.
- [50] S. Diamond, “Percolation due to overlapping ITZs in laboratory mortars? A microstructural evaluation,” *Cem. Concr. Res.*, vol. 33, no. 7, pp. 949–955, Jul. 2003.
- [51] J. P. Ollivier, J. C. Maso, and B. Bourdette, “Interfacial transition zone in concrete,” *Adv. Cem. Based Mater.*, vol. 2, no. 1, pp. 30–38, 1995.

- [52] W. Ashraf, J. Olek, and J. Jain, “Microscopic features of non-hydraulic calcium silicate cement paste and mortar,” *Cem. Concr. Res.*, vol. 100, pp. 361–372, 2017.
- [53] S. Brunauer, P. H. Emmett, and E. Teller, “Adsorption of Gases in Multimolecular Layers,” *J. Am. Chem. Soc.*, vol. 60, no. 2, pp. 309–319, 1938.
- [54] W. Thomson, “On the Equilibrium of Vapour at a Curved Surface of Liquid.,” *Proc. R. Soc. Edinburgh*, vol. 7, pp. 63–68, 1872.
- [55] S. Diamond, “A critical comparison of mercury porosimetry and capillary condensation pore size distributions of portland cement pastes,” *Cem. Concr. Res.*, vol. 1, no. 5, pp. 531–545, 1971.
- [56] Y. Abdel-Jawad and W. Hansen, “Pore Structure of Hydrated Cement determined by Mercury Porosimetry and Nitrogen Sorption Techniques.,” *MRS Proc.*, L.R. Roberts and J. P. Skalny, Eds., Material Research Society, Pittsburgh, PA, vol. 137, pp. 105–118, 1988.
- [57] C. Atkins, “Physical deterioration mechanisms,” in *Concrete durability - A Practical Guide to the Design of Durable Concrete Structures*, Soustos M., Ed. ICE Publishing, 2010, pp. 35–47.
- [58] ACI 201 Committee, *Guide to Durable Concrete (ACI 201.2R-16)*, American Concrete Institute, Farmington Hills, MI, 2016.
- [59] T. C. Powers, “Working Hypothesis for Further Studies of Frost Resistance of Concrete,” *ACI J. Proc.*, vol. 41, no. 4, pp. 245–272, 1945.
- [60] T. C. Powers, “The air requirement of frost resistant concrete,” *Proceedings, Highway Research Board*, vol. 29, 1949, pp. 184–202.
- [61] G. G. Litvan, “Adsorption systems at temperatures below the freezing point of the adsorptive,” *Adv. Colloid Interface Sci.*, vol. 9, no. 4, pp. 253–302, 1978.
- [62] G. G. Litvan, “Phase Transitions of Adsorbates:IV, Mechanism of Frost Action in Hardened Cement Pastes,” *J. Am. Ceram. Soc.*, vol. 55, no. 1, pp. 38–42, 1972.
- [63] J. Marchand, R. Pleau, and R. Gagné, “Deterioration of Concrete Due to Freezing and Thawing,” in *Materials Science of Concrete IV*, J. Skalny and S. Mindess, Eds., The American Ceramic Society, Westerville, OH, 1995, pp. 283–354.
- [64] G. W. Scherer and J. J. Valenza, “Mechanism of Frost Damage,” in *Materials Science of Concrete VII*, Young Francis and J. P. Skalny, Eds., American Ceramic Society, Westerville, OH, 2005, pp. 209–246.

- [65] O. Coussy and P. J. M. Monteiro, “Poroelastic model for concrete exposed to freezing temperatures,” *Cem. Concr. Res.*, vol. 38, no. 1, pp. 40–48, 2008.
- [66] M. J. Setzer, “Mechanical Stability Criterion, Triple-Phase Condition, and Pressure Differences of Matter Condensed in a Porous Matrix,” *J. Colloid Interface Sci.*, vol. 235, no. 1, pp. 170–182, 2001.
- [67] M. J. Setzer, “Frost-attack on concrete — modeling by the micro-ice-lens model — evaluating by RILEM CIF test,” in *Creep, Shrinkage and Durability Mechanics of Concrete and Concrete Structures*, T. Tanabe, K. Sakata, H. Mihashi, R. Sato, K. Maekawa and H. Nakamura, Eds., Taylor & Francis Group, London, 2008, pp. 971–977.
- [68] M. J. Setzer, “Action of frost and deicing chemicals - basic phenomena and testing,” in *Freeze-Thaw Durability of Concrete*, J. Marchand, M. Pigeon and M. Zetzer, Eds., E&FN Spon, London, 1997, pp. 3–22.
- [69] R. A. Helmuth, “Dimensional Changes of Hardened Cement Pastes Caused by Temperature Changes,” 1961, pp. 315–336.
- [70] G. Fagerlund, “Critical degrees of saturation at freezing porous and brittle materials,” *Doctoral thesis*, Division of Building Materials, Lund Institute of Technology, Lund, 1972.
- [71] Cement.org, “Control of Air Content in Concrete,” S. Kosmatka, Eds., Portland Cement Association, vol. 19, no. 1, pp. 1–8, 1998. [Online] Available: http://www.cement.org/docs/default-source/fc_concrete_technology/pl981.pdf?sfvrsn=2
- [72] G. G. Litvan, “Frost action in cement in the presence of De-Icers,” *Cem. Concr. Res.*, vol. 6, no. 3, pp. 351–356, 1976.
- [73] G. G. Litvan, “Phase Transitions of Adsorbates: VI, Effect of Deicing Agents on the Freezing of Cement Paste,” *J. Am. Ceram. Soc.*, vol. 58, no. 1–2, pp. 26–30, 1975.
- [74] G. G. Litvan, “Freeze-Thaw Durability of Porous Building Materials,” *Durability of Building Materials and Components ASTM STP 691*, P. J. Sereda and G. G. Litvan, Eds., American Society for Testing and Materials, Philadelphia, PA, 1980, pp. 455–463.
- [75] M. Pigeon and R. Pleau, *Durability of Concrete in Cold Climates*. London: E&FN SPON, 1995.
- [76] M. J. Setzer, “Development of the Micro-Ice-Lens Model,” *Proceedings of International RILEM Workshop on Frost Resistance of Concrete*, M. Setzer, R. Auberg and H. Keck, Eds., RILEM publication S.A.R.L., Essen, Germany, 2002, pp. 133–145.

- [77] G. G. Litvan, "Phase transitions of adsorbates. III. Heat effects and dimensional changes in nonequilibrium temperature cycles," *J. Colloid Interface Sci.*, vol. 38, no. 1, pp. 75–83, 1972.
- [78] J. J. Beaudoin and C. MacInnis, "The mechanism of frost damage in hardened cement paste," *Cem. Concr. Res.*, vol. 4, no. 2, pp. 139–147, 1974.
- [79] W. Ashraf, J. Olek, and V. Atakan, "Carbonation Reaction Kinetics of Carbonation Curing and CO₂ Sequestration Capacity of Hydraulic and Non-Hydraulic Cementitious Binders," in *4th international conference on sustainable construction materials and technologies*, P. Claisse, E. Ganjian, and T. Naik, Eds., Las Vegas, 2016, vol. 2.
- [80] J. F. Young, "Capillary porosity in hydrated tricalcium silicate pastes," *Powder Technol.*, vol. 9, no. 4, pp. 173–179, 1974.
- [81] M. Daimon, S. A. Abo-el-Enein, G. Hosaka, S. Goto, and R. Kondo, "Pore Structure of Calcium Silicate Hydrate in Hydrated Tricalcium Silicate," *J. Am. Ceram. Soc.*, vol. 60, no. 3–4, pp. 110–114, 1977.
- [82] D. N. Winslow and S. Diamond, "A Mercury Porosimetry Study of the Evolution of Porosity in Portland Cement," *J. Mater.*, vol. 5, no. 3, pp. 564–585, 1970.
- [83] G. Verbeck, "Pore Structure," in *STO49877S Significance of Tests and Properties of Concrete and Concrete-Making Materials*, R. Mielenz, D. Bloem, L. Gregg, L. Gregg, C. Kesler, and W. Price, Eds. ASTM International, West Conshohocken, PA, 1966, pp. 211–219.
- [84] L. I. Edel'sman, D. S. Sominskii, and N. V. Kopchikova, "Pore size distribution in cement rocks," *Colloid J.*, vol. 23, no. 2, pp. 192–196, 1961.
- [85] E. Washburn, "Note on a Method of Determining the Distribution of Pore Sizes in a Porous Material," in *Natl Acad Sci U S A*, 1921, vol. 7, no. 4, pp. 115–116.
- [86] Cement.org., "Ettringite Formation and the Performance of Concrete," G. S. Barger *et al.*, Portland Cement Association, 2001. [Online]. Available: https://www.cement.org/docs/default-source/fc_concrete_technology/is417-ettringite-formation-and-the-performance-of-concrete.pdf?sfvrsn=412%26sfvrsn=412
- [87] F. Locher and W. Richartz, "Setting of cement: I, Reaction and development of structure," *Zem.-Kalk-Gips*, vol. 29, no. 10, pp. 435–442, 1976.

- [88] R. A. Cook and K. C. Hover, "Mercury porosimetry of cement-based materials and associated correction factors," *Constr. Build. Mater.*, vol. 7, no. 4, pp. 231–240, 1993.
- [89] K. L. Scrivener and P. L. Pratt, "Characterisation of Portland Cement Hydration by Electron Optical Techniques," in *MRS Proceedings*, vol. 31, 1984, p. 351-356.
- [90] K. L. Scrivener, "The Use Of Backscattered Electron Microscopy And Image Analysis To Study The Porosity Of Cement Paste," in *MRS Proceedings*, vol. 137, 1988, p. 129.
- [91] A. R. Spurr, "A low-viscosity epoxy resin embedding medium for electron microscopy," *J. Ultrastructure Res.*, vol. 26, no. 1–2, pp. 31–43, 1969.
- [92] K. L. Scrivener, "Characterisation of the ITZ and its quantification by test methods," in *Engineering and Transport Properties of the Interfacial Transition Zone in Cementitious Composites - State-of-the-Art Report of RILEM TC 159-ETC and 163-TPZ*, M. G. Alexander, G. Arliguie, G. Ballivy, A. Bentur, and J. Marchand, Eds., RILEM, 1998, pp. 3–18.
- [93] J. J. Zheng, C. Q. Li, and X. Z. Zhou, "Thickness of interfacial transition zone and cement content profiles around aggregates," *Mag. Concr. Res.*, vol. 57, no. 7, pp. 397–406, 2005.
- [94] M. Jebli, F. Jamin, E. Malachanne, E. Garcia-Diaz, and M. S. El Youssoufi, "Experimental characterization of mechanical properties of the cement-aggregate interface in concrete," *Constr. Build. Mater.*, vol. 161, pp. 16–25, 2018.
- [95] D. N. Winslow, M. D. Cohen, D. P. Bentz, K. A. Snyder, and E. J. Garboczi, "Percolation and pore structure in mortars and concrete," *Cem. Concr. Res.*, vol. 24, no. 1, pp. 25–37, 1994.
- [96] Z. Yu, C. Ni, M. Tang, and X. Shen, "Relationship between water permeability and pore structure of Portland cement paste blended with fly ash," *Constr. Build. Mater.*, vol. 175, pp. 458–466, 2018.
- [97] S. Diamond and J. Huang, "The interfacial transition zone: reality or myth?," in *The Interfacial Transition Zone in Cementitious Composites*, 1998, pp. 3–39.
- [98] H. Ramézani, P. Mounanga, J. Jeong, and M. Bouasker, "Role of cement paste composition on the self induced stress in early-age mortars: Application of the Cosserrat size number," *Cem. Concr. Compos.*, vol. 39, pp. 43–59, 2013.
- [99] ASTM C1585, Standard Test Method for Measurement of Rate of Absorption of Water by Hydraulic Cement Concrete, ASTM international, West Conshohocken, PA, 2004.

- [100] C. Di Bella, I. De la Varga, J. Castro, D. P. Bentz, R. P. Spragg, and J. Weiss, “Fluid transport in high volume fly ash mixtures with and without internal curing,” *Cem. Concr. Compos.*, vol. 45, pp. 102–110, 2013.
- [101] C. Hall and C. Hall, “Water sorptivity of mortars and concretes: A review,” *Mag. Concr. Res.*, vol. 41, no. 147, pp. 51–61, 1989.
- [102] G. De Schutter and K. Audenaert, “Evaluation of water absorption of concrete as a measure for resistance against carbonation and chloride migration,” *Mater. Struct. Constr.*, vol. 37, no. 273, pp. 591–596, 2004.
- [103] S. P. Zhang and L. Zong, “Evaluation of relationship between water absorption and durability of concrete materials,” *Adv. Mater. Sci. Eng.*, vol. 2014, pp. 1-8, 2014.
- [104] ASTM C666/C666M-03, Standard Test Method for Resistance of Concrete to Rapid Freezing and Thawing, ASTM international, West Conshohocken, PA, 2003.
- [105] ASTM C215-14, Standard Test Method for Fundamental Transverse, Longitudinal, and Torsional Resonant Frequencies of Concrete Specimens, ASTM international, West Conshohocken, PA, 2014.
- [106] ASTM E1876-09, Standard Test Method for Dynamic Young’s Modulus, Shear Modulus, and Poisson’s Ratio by Impulse Excitation of Vibration, ASTM international, West Conshohocken, PA, 2015.
- [107] S. Caré, “Influence of aggregates on chloride diffusion coefficient into mortar,” *Cem. Concr. Res.*, vol. 33, no. 7, pp. 1021–1028, 2003.
- [108] Z. Ranachowski, D. Józwiak-Niedźwiedzka, P. Ranachowski, M. Dąbrowski, S. Kudela, and T. Dvorak, “The determination of diffusive tortuosity in concrete specimens using X-ray microtomography,” *Arch. Metall. Mater.*, vol. 60, no. 2A, pp. 1115–1119, 2015.
- [109] P. H. Torrans and D. L. Ivey, “Review of Literature on Air-Entrained Concrete,” Texas Transportation Insistutue Texas A&M University, College Station, Texas, Report. 103-1, February 1968.
- [110] T. C. Powers, “Topics in Concrete Technology, 3. Mixtures Containing Intentionally Entrained Air,” *J. PCA Res. Dev. Lab.*, vol. 6, no. 3, pp. 19–41, 1964.
- [111] B. J. E. Backstrom, R. W. Burrows, C. Richard, and V. E. Wolkodoff, “Origin, Evolution, and Effects of the Air Void System in Concrete, Part 3-The Air Void System in Job Concrete,” *ACI J. Proc.*, vol. 55, no. 10, 1958.

- [112] M. T. Hasholt, *Air void structure and frost resistance: A challenge to Powers' spacing factor*, vol. 47, no. 5. 2014.
- [113] D. J. Corr, P. J. M. Monteiro, and J. Bastacky, "Microscopic characterization of ice morphology in entrained air voids," *ACI Mater. J.*, vol. 99, no. 2, pp. 190–195, 2002.
- [114] ASTM C457/C457M-12, Standard Test Method for Microscopical Determination of Parameters of the Air-Void System in Hardened Concrete, ASTM international, West Conshohocken, PA, 2013.
- [115] ASTM C642-13, Standard Test Method for Density, Absorption, and Voids in Hardened Concrete, ASTM international, West Conshohocken, PA, 2013.
- [116] ASTM C672/C672M-12, Standard Test Method for Scaling Resistance of Concrete Surfaces Exposed to Deicing Chemicals, ASTM international, West Conshohocken, PA, 2011.
- [117] F. Massazza, "Pozzolana and Pozzolanic Cements," *Cem. Concr. Compos.*, vol. 15, pp. 471–635, 1993.
- [118] Y. Gao, H. Shim, R. H. Hurt, E. M. Suuberg, and N. Y. C. Yang, "Effects of carbon on air entrainment in fly ash concrete; The role of soot and carbon black," *Fuel Energy Abstr.*, vol. 38, no. 4, p. 231, 1997.
- [119] K. J. Folliard, K. Hover, N. Harris, and M. T. Ley, "Effects of Texas Fly Ash on Air-Entrainment in Concrete: Comprehensive Report," CTR the University of Texas at Austin, Austin, TX, Tech. Report. FHWA/TX-08/0-5207-1, Feb. 2008.
- [120] Y. Farnam, C. Villani, T. Washington, M. Spence, J. Jain, and J. Weiss, "Performance of carbonated calcium silicate based cement pastes and mortars exposed to NaCl and MgCl₂ deicing salt," *Constr. Build. Mater.*, vol. 111, pp. 63–71, 2016.
- [121] M. Thomas, "Optimizing the Use of Fly Ash in Concrete," Portland Cement Association, Publication IS 548, p. 24, 2007.
- [122] H. Jeong, J. Olek, D. K. Pannell, and R. Geiger, "Investigation of the effects of chloride-based deicers on plain and fly ash concretes containing dolomite as coarse aggregate," in *Proceedings of the 12th International symposium on Brittle Matrix Composites*, 2019, pp. 231–244.
- [123] A. 318-14, Building Code Requirements for Structural Concrete and Commentary (ACI 318-14). American Concrete Institute, 2014.

- [124] J. T. Kevern, K. Wang, and V. R. Schaefer, "Effect of coarse aggregate on the freeze-thaw durability of pervious concrete," *J. Mater. Civ. Eng.*, vol. 22, no. 5, pp. 469–475, 2010.